THE INTERACTION OF SUBDUCTING SLABS AND THE 670 KILOMETER DISCONTINUITY

Thesis by

Scott David King

In Partial Fulfillment of the Requirements

for the Degree of

Doctor of Philosophy

California Institute of Technology

Pasadena, California

1991

(Submitted August 20, 1990)

Acknowledgements

There are many people who helped to make my time spent at Caltech more enjoyable. First of all, I want to thank Brad Hager, who unselfishly shared many good ideas, and listened to many of my crazy ideas; I especially want to thank Brad for allowing me to work on a variety of different projects, some of which, like ConMan, actually turned into something useful. Also, thanks to Brad, Patty, Emmy, and Axel for their hospitality and friendship, especially for sharing their home with me on several occasions when I visited in Boston.

I was very lucky to have the opportunity to work not only with Brad, but with Arthur Raefsky, who shared his knowledge of finite element analysis and vector programming with me. Without his help and guidance ConMan would probably not exist. I also want to thank Don Anderson, who always challenged me to think about alternative hypotheses, for his advice and ideas. As an undergraduate, I was inspired and encouraged by Frank Richter.

I also want to thank Doug Neuhauser, the Seismo lab computer system manager. Doug not only kept the computers working—many times working all weekend, but helped debug software, diagnosed network problems, and installed many new and useful programs. Without Doug, it would have taken me much longer to finish my

degree.

My computer expenses were supported by several sources: Cray Research Inc. provided time on the JPL Cray X-MP, and NSF provided time on the NCSA Cray 2 and the SDSC Cray X-MP. I was also supported by grants from NASA and NSF.

I am grateful for the opportunity I had to participate in the annual mantle convection workshops, sponsored by IGPP, at Los Alamos National Laboratory, New Mexico. Some of the ideas in this work are the result of discussions and projects begun at mantle convection workshops.

While I was at the Seismo lab, I was fortunate enough to have several wonderful officemates: Lucianna Astiz, who helped me get past my orals and gave me her lucky pointer, Leslie Sonder, who *puni*shed me with her humor and shared her insight as well, and Andrea Donnellan, who was always willing to listen to both scientific and personal problems and was (and is) a good friend. I also enjoyed getting to know and work with the other students and post-docs who worked for Brad: I really enjoyed collaborating with Louise Kellogg; Walter Kiefer provided ideas and was a great resource for references; Mike Gurnis shared his subduction work; and Mark Richards helped me get started.

I also had several great roommates while at Caltech: John Brewer, the first person I met at Caltech and doubtless the last person I will see before I leave, has been a great friend; our ability to read each others' minds at times has been truly frightening. Todd Przybycien, aside from having an unspellable last name, has also been a great friend, card partner, carpenter, and bartender. Holden "Opie" Thorp was also a great friend as well as comedian and music/entertainment center, and

David Hwang always made me laugh about something.

I also want to thank my friends at the Lake Avenue Church Wednesday Night Study, especially Frank, Jim, Bob, and Janet P., whose friendship, support and prayers helped me make it through. But most of all, I thank my parents, who supported me financially, emotionally and spiritually. With out their support and prayers, I never would have made it.

To my parents.

THE INTERACTION OF SUBDUCTING SLABS AND THE 670 KILOMETER DISCONTINUITY

Scott David King, Ph.D.

California Institute of Technology 1991

The subduction of oceanic lithosphere plays a major role in the dynamics of the Earth. The dynamics of subduction are influenced both by variations in density (due to phase changes or compositional changes), and variations in viscosity encountered by the slab; the rheology of the slab and the coupling of the slab with the oceanic lithosphere also play important roles. Geoid and topography place fundamental constraints on subduction, and observations can be used to test various mantle models.

The effects of the rheology of slabs are considered using finite element convection calculations with Newtonian (linear) and non-Newtonian (power-law) temperature-dependent rheology. Newtonian temperature-dependent fluids do not exhibit slab-like features without weakening the thermal boundary layer. Weak zones are imposed at the trench and ridge, and the effects of varying the size, location, and strength of the weak zones are studied. Non-Newtonian rheology provides a self-consistent mechanism for weakening the thermal boundary layer without imposing a weak zone

at the trench. This self-consistency is not proof or confirmation of the importance of power-law deformation in the Earth. Even with non-Newtonian rheology, a weak zone at the ridge is necessary for plate-like behavior.

The geoid and topography for slabs with a density discontinuity and a viscosity discontinuity are compared. Weak slabs deform rapidly by spreading out along the density discontinuity with little deformation of the boundary, while strong slabs deform slowly and locally depress the density boundary. However, the long wavelength components of the geoid and topography are independent of the lateral variations in viscosity from the slab. Finite deformations of a compositional boundary are compared with an undeformable boundary approximation; the long wavelength components of the geoid and topography are indistinguishable for boundary deformations up to several hundred kilometers.

Subduction calculations are computationally intensive and high resolution is required to resolve deformation at the trench. The solutions are time-dependent, and a temperature-dependent rheology is required. Faster and more powerful numerical techniques are needed. A fast implementation of the finite element method is presented. Applied to creeping flow, this formulation allows large viscosity variations, but is still efficient on a vector supercomputer.

Table of Contents

List of Tables

List of Figures

It's a bawdy planet. —Shakespeare, *The Winter's Tale*, I, ii

Chapter 1

Background

Over the past two decades numerical models of mantle convection have changed dramatically from calculations of flow in a two-dimensional Cartesian box with uniform material properties (e.g., Richter, 1973; McKenzie, Roberts and Weiss, 1974) to two-dimensional temperature and pressure dependent calculations including plates and slabs (Christensen and Yuen, 1984; Gurnis and Hager, 1988), chemical and phase boundaries (e.g., Chirstensen and Yuen, 1984), and recently constant property three-dimensional Cartesian (e.g., Gable, O'Connell and Travis, 1988, 1990; Houseman, 1988) and spherical calculations (e.g., Bercovici *et al.*, 1989a, 1989b). Part of this advance has come from a better understanding of the important processes governing creeping flow in the Earth, but most of the advance has come from advances in the speed of computers and computational techniques. Convection calculations have been and still are limited by the speed and memory of the fastest computers available.

The elastic and compositional structure of the mantle was studied long before the

idea of a convecting and dynamic mantle was accepted (e.g., Jeffreys, 1939; Birch, 1952). It was not until the emergence of plate tectonic theory in the late 1960's that the notion of mantle-wide flow was generally accepted. Over the last 20 years two models of mantle flow have dominated the literature: one, where convection involves the whole mantle, from the surface to the core mantle boundary; and the other, where the upper mantle and the lower mantle convect separately with little or no transfer of material between them. The structure of the one-dimensional seismic velocity model puts this boundary at approximately 670 kilometers. These models have profound implications not only for the dynamics of the Earth, but also on its formation, bulk composition and evolution. There has been a great deal of often heated debate over the validity of these models.

In the classic layered mantle model, the upper mantle is a reservoir associated with chemical composition change from sea floor spreading, while the lower mantle is a more primitive (undifferentiated) and rarely sampled reservoir (e.g., Wasserburg and DePaolo, 1979; Allégre, 1982). The strongest evidence for whole mantle convection is the seismic observation of travel time anomalies from deep focus earthquakes which are interpreted as cold slabs penetrating deep into the mantle (Jordan, 1977; Creager and Jordan, 1984, 1986). This implies a considerable flux of material into the lower mantle and conflicts with the classical view of a chemically stratified mantle.

The conflicting evidence has lead to new hybrid models of convection such as penetrative convection (e.g., Silver, Carlson and Olson, 1988) and whole mantle convection with a large viscosity increase (e.g., Davies, 1984; Gurnis and Hager, 1988; Hager and Richards, 1989). These models are gaining in popularity over the

traditional whole or layered models.

Subducted slabs are a key to understanding the convective style of the mantle. As Hager and O'Connell (1981) point out, the temperature dependence of mantle rheology has two important effects. First, the temperature contrast across the upper thermal boundary layer (the plates and slabs) will be larger than that across the lower thermal boundary layer because the upper thermal boundary layer is stabilized by the temperature-dependent rheology. This means the negative buoyancy of the slab will be the largest source of thermal buoyancy in the convecting system. Second, the bottom thermal boundary layer will be destabilized by the temperature-dependent rheology and should lead to convective instabilities which are small in comparison to the plates. Internal heating will also increase the dynamic importance of the upper thermal boundary layer in relation to the lower one. Thus, density contrasts associated with plates and slabs are the predominate thermal density contrasts within the earth's interior.

The work in this thesis consists of two parts: modeling and studying the subduction of oceanic lithosphere using numerical convection calculations; and developing and implementing faster finite element algorithms for convection calculations. Numerical studies of subduction are important because while the geologic and seismic observations provide constraints on the depth of subduction and the deformation of the slabs, these observations alone cannot distinguish among different mantle models. Geologic and seismic observations can be compared to numerical subduction calculations to test different mantle models. Many simple static models have been used to study subduction (Schubert and Turcotte, 1971; Schubert, Yuen and Turcotte,

1975; Davies, 1980; Anderson, 1987), but these models are potentially misleading because subduction is time-dependent and the rheological properties of the mantle are too complicated for simple analytic models. While the implementation of the finite element algorithm is not directly related to the geophysical problem studied, it is the backbone of this work since none of it would have been possible without the improvements in computational power that resulted.

1.1 Numerical Background

At the time this work began, the NSF (National Science Foundation) supercomputer centers were beginning to make time available to academic researchers. It became clear from the first tests on the Cray X-MP at the San Diego Supercomputer Center that our code (Daly and Raefsky, 1985) was not achieving vector performance, especially when compared with other benchmarks of the Cray X-MP (e.g., Dongarra, 1987). The Daly and Raefsky code was written before vector or parallel computers became available to most academic researchers. After studying the Cray's architecture and learning how to "vectorize" or modify a code for a vector computer, a new code, which would take advantage of a vector computer like the Cray, was written.

In computer architecture terms, a vector is a one-dimensional data structure characterized by a starting address in memory, a length and an offset between elements (called the stride). A vector computer can perform operations on a vector of data much faster than if it were to process each element of the vector separately (called scalar processing). The computer code must be able to deliver vectors of data to the functional units (i.e., the adder or multiplier) to take advantage of vector arithmetic

and achieve vector speeds. The simplest way a program can do this is with a FORTRAN do loop. (This simple view of a vector computer is only intended to acquaint the reader with a few basic concepts; a complete discussion can be found elsewhere (e.g., Levesque and Williamson, 1989)).

For many codes this is straightforward; however, not every algorithm is vectorizable. Consider the following example of FORTRAN code to calculate the first 100 Fibonacci numbers:

```
NUMBER(1) = 1
NUMBER(2) = 1
DO I = 3, 100
    NUMBER(I) = NUMBER(I-1) + NUMBER(I-2)
END DO
```

Each Fibonacci number is dependent on the previous two numbers in the sequence. For a classical Von Neumann computer this is fine, but on a vector machine do loop, structures are handled differently. In a do loop which vectorizes, all the results on the right hand side of the equal sign must be known before the do loop begins. The Fibonacci number calculation is an example of a do loop with a vector dependence, and the Fibonacci numbers cannot be computed with vector arithmetic.

Another classic problem is a do loop which will not vectorize because of the program structures or data structures. Consider the following example taken from a FORTRAN code which multiplies two N by N matrices, A and B, and stores the result in the N by N matrix C:

```
DO I = 1, N
DO J = 1, N
    C(I,J) = 0
    DO K = 1, N
        C(I,J) = C(I,J) + A(I,K) + B(K,J)
    END DO
END DO
END DO
```

The inner 'K' do loop in this example is a vector reduction (dot product) which cannot run at peak rates on a vector machine. (Note that the left hand side C(I,J) is a constant for all 'K' in the inner loop). In this example, switching the 'I' and the 'K' do loops will reduce the execution time by a factor of 6 on a Cray X-MP for N greater than 30. In the case of the Daly and Raefsky code, the do loops are like the second example; the basic algorithm is vectorizable but the data structures and program structures are not suitable for a vector computer.

Over a period of four to six months a finite element code for convection in a two-dimensional Cartesian geometry, based on the Daly and Raefsky code, was written and tested. This code was named ConMan after CONvection in the MANtle. Another two to three months were spent testing ConMan against both analytic solutions and a set of benchmarks from the Los Alamos Mantle Convection Workshop (Travis *et al.*, 1990). The short time spent in developing ConMan shows that relatively little effort went into writing it when compared to the enormous improvement in CPU time for the problems that are studied.

A simple example illustrates the improvement in CPU time of ConMan compared to the original code. The standard problem before writing ConMan was isoviscous convection in a 32 element by 32 element unit aspect ratio box. A typical run takes

eight hours of CPU time on a VAX 780 and 40 minutes of CPU time on a Cray X-MP with the original code. With ConMan the same problem runs in less than two minutes of CPU time on a Cray X-MP, more than 250 times faster than the original code on a VAX 780. Using the theoretical speeds of the VAX 780 of 0.5 MFLOPS (Millions of FLOating Point instructions per Second) and 210 MFLOPS for the Cray X-MP, it is clear that ConMan is able to achieve close to the theoretical speed of the Cray. Because of the increase in speed brought about by ConMan, bigger and more complex problems could be considered. The work in this thesis would not have been possible without ConMan.

Because the development of this code was such an important part of this work, Chapter 2 outlines some of the details of writing a finite element code for a vector computer. Several of the key subroutines from ConMan are included in Appendix D to illustrate the strategy for vectorizing a finite element code.

1.2 Geophysical Background

Subduction of the oceanic lithosphere clearly plays a major role in convection in the Earth's mantle. Plate motions are the most direct evidence of mantle motion. It accounts for about eighty percent of the oceanic heat transport (Davies, 1988a, 1988b), plays a dominant role in the mass transport and is important in the chemical processing of the mantle (Allègre and Turcotte, 1985, 1986).

I begin with a brief review of some of the important work that has been done on subduction. A basic observation about subduction is that there are no earthquakes below 700 kilometers. This depth corresponds to a jump in seismic velocity of about

6–11% in the one-dimensional velocity profile of the mantle at 670 kilometers (Anderson, 1967; Anderson, 1970). While Birch (1952) considered the increase in seismic velocity to be smooth he did discuss the transition of upper mantle minerals to a mixed oxide assemblage in the lower mantle. It is known that from 12-26 GPa (400 to 750 kilometers) assemblages of olivine, pyroxene and garnet, thought to represent the composition of the mantle at this depth, undergo a series of solid-solid phase changes (e.g., Anderson, 1970, 1986; Ringwood and Irifume, 1988). The jump in seismic velocity is often assumed to be a density increase as a result of one of these phase changes, spinel to "post-spinel" being regarded as the most likely candidate (e.g., Anderson, 1970; Anderson, 1990). It has also been suggested that a phase change is insufficient to match the jump in seismic velocity, thus a change in composition is also needed (e.g., Anderson, 1970; Anderson, 1977; Lees, Bukowinski and Jeanloz, 1982; Anderson, 1990). Jeanloz and Thompson (1983) have shown that an increase in iron content by 5-10% would be consistent with the seismic data and could not be resolved by seismic models. Knittle, Jeanloz and Smith (1986) argue that a 2:1 mixture of olivine and pyroxene, at the appropriate pressure range, can account for the lower mantle elasticity and density. The relationship between the spinel post-spinel phase change, composition of the upper and lower mantle, and seismic discontinuity at about 670 kilometers is still not completely resolved.

The lack of earthquakes below 700 kilometers has been interpreted as evidence that subducted slabs do not extend below this depth. It is also observed that seismicity reaches a minimum at around 250 km and that there is a peak in seismicity around 600 km (e.g., Gutenburg and Richter, 1954; Sykes, 1966; Isacks, Oliver and Sykes,

1968). Isacks and Molnar (1971), Richter (1979) and Vassiliou *et al.* (1984) have shown that the stress pattern in subducted slabs changes from dominantly downdip extension at about 200–400 kilometers to dominantly downdip compression at about 500–600 kilometers. Giardini and Woodhouse (1984) used the seismicity pattern and focal mechanisms to show that the deep Tonga slab is thickening under compression as it approaches the "670." This information is consistent with the hypothesis that the subducting slab is meeting a barrier at about 700 kilometers. Studies have shown that a polymorphic phase change at 670 km would probably not be sufficient to stop a subducting slab from penetrating into the lower mantle unless the transformation is strongly endothermic (e.g., Schubert and Turcotte, 1971; Davies, 1980; Hager and Raefsky, 1981; Olson and Yuen, 1982; Christensen and Yuen, 1984). Although it has usually been assumed that this barrier is an increase in density, Vassiliou, Hager and Raefsky (1984) demonstrated that a viscosity jump of a factor of 10 is consistent with the seismic observations.

Davies and McKenzie (1969) first demonstrated the effects of the slab on travel-time residuals from subduction zone earthquakes. Since that time a number of studies have attempted to use the travel-time residuals to study the depth of the slab. Jordan (1977), Creager and Jordan (1984, 1986) and Fischer, Creager and Jordan (1990) analyzed long-wavelength variations in projections of travel time residuals of P waves onto the focal spheres of deep earthquakes in subducted slabs. In a number of subduction regions they found an anomalously fast travel-time residual in a band pattern with a strike and dip matching the slab. They interpret this as subducted slabs extending to depths greater than 900 kilometers. Their results,

however, cannot uniquely distinguish between a slab extending into the lower mantle and a cold downwelling in the lower mantle triggered by the impinging of a subducted slab on the "670."

More recent work (Zhou and Anderson, 1989; Zhou, Anderson and Clayton, 1990) also studied the residual spheres from a number of deep slab events. They used several lower mantle models, included near-receiver effects, and studied the effect of takeoff angle on the residual pattern. They found slab-like patterns which were sensitive to the model chosen and subhorizontal patterns, not the near vertical patterns indicative of deep slabs, beneath Japan.

Barkley (1977) identified a phase in the P wave coda from deep earthquakes in which he attributed to an S-P conversion or scattering at about 670 kilometers. Bock and Ha (1984) observed a similar phase from beneath the Tonga arc and noted that the short period of this phase indicated it was from a sharp (> 5 km) boundary. Richards and Wicks (1990) used short period records from earthquakes in the Tonga slab recorded at the Warramunga Seismic Array in central Australia to study the depth of the "670" in the vicinity of the Tonga slab. Using the travel time data across the seismic array they were able to estimate the depth of the "670" from three different regions on the Tonga trench. Although the phase could not be identified everywhere, where it was identified the depth of the conversion was never deeper than 700 kilometers. They argue that this implies the "670" is a phase change because the density anomaly associated with the cold Tonga slab would deform a chemical boundary more than 50 kilometers.

Zhou and Clayton (1990; also see Zhou, 1990) used seismic tomography to obtain

images of P and S wave velocities under island arcs in the Northwest Pacific. They found strong fast velocity anomalies associated with Wadati-Benioff zones, although sometimes the dip of the fast anomalies did not line up with the earthquakes inferred to be in the slab. The structure near the "670" becomes quite complicated in the images. Mariana appears to have a fast anomaly beneath "670" which could be from the slab, while other arcs show anomalies which could be interpreted as the slab flattening along the "670."

Long wavelength variations in the geoid are another constraint on the Earth's interior structure. Hager *et al.* (1985) showed that most of the geoid at long wavelengths (i.e., > 10,000 km) could be explained by density anomalies inferred from seismic tomography along with resulting dynamic topography. Hager (1984) used a 2 layer model to parameterize the interior viscosity and obtained a good agreement with the observed geoid over subduction zones in the Pacific for a viscosity model with a factor of 30 increase at 670 km. Hager and Richards (1989) point out that a chemical boundary cannot be ruled out on the basis of the geoid. They note that numerical studies (e.g., Hager and Raefsky, 1981; Christensen and Yuen, 1984) predict large dynamic topography on the "670" for the density difference between the upper and lower mantle and the modeled density of the slab which they need to match the geoid.

While a first order observation of plate tectonics is that plates are rigid and deformation takes place at plate boundaries, it is not clear how slabs behave. Bevis used slab geometry and the seismic moment release (1986, 1988) to estimate the strain-rate in slabs. He finds that between 75 and 175 kilometers the global average

downdip strain-rate is about 10^{-15} per second. Using a typical plate velocity of 10 cm/yr this implies a strain accumulation of order 10^{-1} over 100 kilometers. Bevis concludes that slabs have little flexural rigidity and do not behave elastically.

Melosh and Raefsky (1981) computed the stresses is a subducting slab using a viscoelastic finite element formulation. They modeled a subducting slab as a thin elastic layer over a thicker viscous layer. They found that the first order topographic features in a subduction zone are controlled by viscous stresses and that the elastic plate has little effect. However, Zhang, Hager and Raefsky (1985) showed that this was fortuitous.

Fischer and Jordan (1990) used seismic moment tensor data to estimate the seismic strain-rate in the deep Tonga slab. They found that assuming the seismic and aseismic strain-rate have the same geometry and that the seismic strain-rate represents a steady state value that thickening of the slab by at least 50% is required in central Tonga. They point out that this thickening is consistent with numerical studies of subduction with a viscosity contrast (Gurnis and Hager, 1988). However, this thickening could also be consistent with a chemical boundary.

Slab dip and trench migration are also important observations. Subduction is clearly not symmetric and most slabs dip at angles less than 90 degrees. It has been noted (Gurnis and Hager, 1988) that there is a relationship between arc age and slab dip. Younger arcs generally have steeply dipping slabs ($>$ 70 degrees) and older arcs have shallow dipping slabs associated with them. Elsasser (1971) points out that there is a transverse component to subduction (i.e., perpendicular to slab dip) and that this component is directed toward the ridge and downward.

Garfunkel, Anderson and Schubert (1986) point out that this retrograde motion of the subduction zone has significant implications for mantle flow patterns.

Gurnis and Hager (1988) showed that slab dip and trench motion could be understood by a model with a viscosity jump at the "670." Young slabs which have not reached the "670" have steep dips. As the slab reaches the "670" it becomes anchored in the more viscous lower mantle. The migration of the trench with time causes the slab dip to become more shallow with age.

1.3 Convection Background

Richter and Johnson (1974) used a linear stability analysis of convection in a layered fluid to estimate the range of densities where convection in two separate layers of equal thickness is stable. They identify three regimes of flow: separate convection within each layer, convection over the entire depth of the fluid, and separate convection with waves or deformation of the interface. One major drawback of this work is that the ratio of the thickness of the two layers was never explored.

Richter and McKenzie (1981) performed tank experiments as well as numerical experiments with constant viscosity fluids. They found that layered convection persisted when the density difference between the two fluids was greater than the density difference due to thermal expansion, a broader range of densities for which the system remains in a layered convection configuration than the previous linear stability analysis (Richter and Johnson, 1974). They also found that shear coupling (i.e., downwelling in the upper layer over upwelling in the lower layer) was the preferred state for numerical experiments. In the tank experiments both shear and thermal

coupling (i.e., downwelling in the upper layer over downwelling in the lower layer) were observed (see also Nataf, Moreno and Cardin, 1988). Richter and McKenzie concluded that a density difference of about 1% is needed to stabilize layered convection in a constant viscosity fluid.

Convection in a fluid with strongly temperature-dependent viscosity leads to a convecting system with little or no motion at the surface (Nataf and Richter, 1982). There have been many methods proposed to simulate plates in numerical convection experiments. Early models of convection with plates used discrete jumps in material properties and integration of basal tractions to advect the plates (e.g., Richter and McKenzie, 1978; Hager and O'Connell, 1981). Christensen (1983, 1984) showed that convection with a non-Newtonian temperature-dependent fluid leads to plate-like surface velocities. Davies (1988a) used imposed plate velocities scaled to match the predicted free convection velocity in combination with temperature-dependent viscosity to simulate plates. Kopitzke (1979) showed convection with fixed low viscosity corners and a high viscosity top gives uniform surface velocities. Schmeling and Jacoby (1981) used a temperature-dependent rheology modified by weak zones in the upper boundary layer. Gurnis (1988) and Gurnis and Hager (1988) used imposed weak zones, advected dynamically with the flow, at the trench and ridge, along with temperature-dependent viscosity, to simulate plates and slabs.

Turcotte and Oxburgh (1967) first applied boundary layer theory to plate motions in two-dimensions. In this simple approach, the temperature difference is confined to a thin layer near the boundary layer which moves at a uniform velocity. Somewhat surprisingly, boundary layer theory explains the oceanic heat flow and bathymetry

remarkably well.

Appealing to the success of boundary layer theory, Hager and O'Connell (1981) calculated density contrasts due to the thickening of oceanic lithosphere with age. They modeled the resulting mantle flow in three-dimensional spherical geometry with the current plate configuration and found that the density contrasts within the plates themselves can reasonably account for plate motions. They also showed that since the driving force from the thickening of the lithosphere is spread over the plate area, it balances the force from viscous drag; this produces a model with plate velocities which are uncorrelated with plate size. This is an important observation of Earth's plates which many previous models could not explain.

Hager and O'Connell (1981) also showed that as long as the viscosity of the lithosphere is much greater than the asthenosphere, the plate motions are nearly independent of the viscosity of the lithosphere. This was important to numerical modeling of plates since numerical methods were not (and are still not) yet sophisticated to handle the large change in material properties between the lithosphere and the mantle.

Richter and McKenzie (1978) presented calculations where the subduction dip angle was imposed as part of the initial conditions and was fixed throughout the calculation. The geometry and initial conditions were set up such that the downwelling was symmetric and the dip was 90 degrees. The material properties of the plate and the slab were taken to be the same; hence, the slab had the same high viscosity throughout and was not allowed to deform much. They showed that buoyancy forces due to subduction and plate creation are enough to drive plate motions. They also

found that a low viscosity layer beneath the plate was needed to match gravity data.

Christensen and Yuen (1984) used a temperature- and pressure-dependent rheology, where the cold dense thermal boundary layer simulated a rigid plate and subducting slab. In their calculations, the downwelling occurred in the corner of the box. Because of the boundary conditions, this constrained the dip to be 90 degrees and downwelling to be symmetric. They modeled the "670" as both a chemical and phase boundary identifying three regimes when the "670" is a chemical boundary: no penetration, limited penetration, and total penetration, depending on the magnitude of the density contrast. They also found that because the slab is stronger (due to temperature-dependence) and more buoyancy is concentrated in the slab, a larger density difference of about 3% is necessary to stabilize layered convection, but with large topography on the boundary. For a phase change, they found that a moderately negative Clapeyron slope could act with a small chemical density difference to prevent slabs from penetrating deep into the lower mantle.

Kincaid and Olson (1987) used tank experiments with a cold, dense viscous slab in a fluid with a density contrast at depth to study subduction. Their results confirmed the numerical models of Christensen and Yuen (1984). The good agreement is somewhat surprising since two fluids used by Kincaid and Olson, representing the upper and lower mantle, also had a factor of 10 difference in viscosity, while Christensen and Yuen did have a viscosity difference. Kincaid and Olson (1987) also showed that when the slab is the only source of negative buoyancy, retrograde subduction prevails and that slab migration and penetration into the lower layer are related.

Gurnis and Hager (1988) used imposed weak zones at the trench and ridge and

temperature-dependence to simulate plates and slabs. In their calculations, periodic boundary conditions were used and one of the plates was fixed; this resulted in asymmetric downwellings. The dip was controlled by the flow and was not, in general, 90 degrees. They found that a viscosity increase at 670 kilometers is consistent with the seismic observations of slab thickening but does not keep the slab from penetrating into the lower mantle. They also showed that trench migration is a mechanism for explaining the relationship between slab dip and age of the arc, consistent with Kincaid and Olson (1987).

Davies (1988a,b,c) used imposed plate velocities and temperature-dependent rheology to study the effects of rigid plates on the geoid, topography and heat-flux of a convecting system. He showed that plates are responsible for at least 80% of the heat transfer (1988b). He also showed that accounting for plumes, the depth age relation of Parsons and Sclater (1977) showed no departure from the cooling half-space model, eliminating the need for small scale convection. Davies did not apply his methods to subducting regions, but concentrated at spreading centers. In a later work, Davies (1989) defended the imposed velocity calculations by comparing those calculations to calculations with imposed weak zones, showing good agreement between the two methods.

1.4 Summary

The previous work can be classified in two broad categories: convection with density discontinuities (e.g., Richter and Johnson, 1974; Richter and McKenzie, 1981) and convection with "slab-like" features or driving forces (e.g., Hager and O'Connell,

1981; Gurnis and Hager, 1988). Several studies have attempted to combine both slabs and density discontinuities (Christensen and Yuen, 1984; Kincaid and Olson, 1987). The fate of a subducted slab is controlled by the style of convection and the nature of the "670." Conversely, subduction zones are the most obvious place to see flux between the upper and lower mantle. Therefore, it is necessary to include slabs in any understanding of the possible deformation of a density discontinuity such as the 670 kilometer discontinuity, and a density discontinuity will likly play a major role on the deformation of a subducting slab. In this thesis we bring both slabs and discontinuities together in numerical calculations to further our understanding of both subduction and the nature of the 670 kilometer discontinuity.

Since the nature of convection appears to be more complicated than the classical models of whole or layered mantle convection (Silver, Carlson and Olson, 1988), and since convection is almost certainly time-dependent (Hoffman and McKenzie, 1985; Christensen, 1987) and possibly chaotic (Kellogg and Stewart, 1990), better and more powerful methods are needed to study convection. In Chapter 2, the details needed for writing a high performance finite element code for studying time-dependent convection with strongly varying material properties are outlined. In Appendix C, the implementation of non-linear material properties is outlined and the results of a number of test problems are shown to confirm the validity of the method.

The importance of the rheology of the slab on the slab penetration question has been pointed out by several authors but never investigated (Christensen and Yuen, 1984; Kincaid and Olson, 1987). In Chapter 3, several parameterizations of slab rhe-

ology, from constant viscosity models with imposed weak and strong zones, to simulate temperature-dependence and faulting and or stress weakening at the trench to non-linear, stress-weakening, temperature-dependent rheologies are compared. The resulting flows are sensitive to the choice of plate parameterization indicating that subduction calculations need to proceed with caution.

The most direct observations from subduction zones are the geoid and topography. In Chapter 4, several "subduction" calculations are presented for various mantle models, along with the resulting geoid and topography. Matching trench topography places an additional needed constraint on the weak zone parameterization. Chemically stratified models with a deformable boundary between the fluids and pressure-dependent, hence depth-dependent, viscous models are compared for several slab rheologies. With these results we can begin to assess the strengths and weaknesses of the new hybrid mantle models.

Chapter 2

ConMan: A Vectorized Finite Element Code for Mantle Convection

2.1 Introduction

Many large computational projects in geophysics are now being run on vector supercomputers such as the Cray X-MP. Yet after more than a decade since the introduction of the Cray-1, most geophysicists simply compile their original codes, making use of the fast clock, without taking full advantage of the vector hardware or achieving anywhere near supercomputer speed.

To illustrate, consider the Cray X-MP with a 9.5 nanosecond clock. It takes six clock cycles to compute a floating point addition (seven for a floating point multiplication). This leads to a theoretical peak scalar rate of 9.5 MFLOPS (million floating point operations per second). This is about 25 times faster than a Sun 3/260 workstation (Dongarra, 1987). The theoretical maximum for vector code on the Cray X-MP is 210 MFLOPS, over 20 times faster than the scalar code and 500 times faster

than the Sun. In reality, the theoretical speeds are never reached; however, speeds of 50 to 200 MFLOPS are attainable for many codes (Dongarra and Eisenstat, 1984).

It is often mistakenly believed that for a general code, special tricks are needed to get vector performance. However, while vectorizing compilers are becoming more sophisticated, a code that does not have data structures suitable for vector operations will not perform well on a vector computer. We show that ConMan (CONvection MANtle), a finite element code for two-dimensional, incompressible, thermal convection, runs at speeds up to 65 MFLOPS for the entire code on a Cray X-MP (including i/o and subroutine overhead). ConMan uses the simple concepts we present and no special tricks.

Understanding vectorization is becoming even more important because of the recent introduction of high performance pipelined workstations. The pipeline architecture is similar to a vector register, and many of the same concepts from vector programming apply to getting the maximum performance out of a pipelined computer.

In the next section we discuss the basic concepts of vectorization, including the concepts of chaining and unrolling. Although we illustrate vectorization with the finite element code ConMan, the concepts we present are general. Because we use a general formulation of the finite element method, it would be especially easy to generalize ConMan to solve other equations or other geometries. We then review the equations for incompressible thermal convection and briefly describe the techniques used to solve them using the finite element method. We present benchmarks and timings for several computers and we include an example subroutine from ConMan

in Appendix D for illustration.

2.2 Vectorization

Consider the simple addition

$$c_i = a_i + b_i \qquad for\ i = 1, 2, ..., N_{comp} \tag{2.1}$$

on a generic scalar architecture. A new result, c_i, is available after N_{add}, the total number of cycles needed for one addition (on the Cray X-MP this is six cycles). On a vector computer, after the first summands a_1 and b_1 move to the second step in the addition unit, the next summands, a_2 and b_2, can enter the addition unit. The first result, c_1, is available after N_{add} cycles. Then, unlike a scalar operation, after $(N_{add} + 1)$ cycles, c_2 is available, and so on. After the startup cost, a new result is available every cycle. On the scalar machine, the second result would not be available until after $2 \times N_{add}$ cycles. For long vectors (i.e., N_{comp} large), the vector time is asymptotically reduced by $1/N_{add}$ relative to scalar processing.

In addition to achieving speedup by vectorizing, a vector computer can chain operations. The classic example is the linear algebra operation SAXPY (**S**ingle precision **A** times **X** **P**lus **Y**)

$$c_i = a \cdot x_i + y_i \qquad for\ i = 1, 2, ..., N_{comp} \tag{2.2}$$

Chaining allows the first result, $a \cdot x_1$, to be added to y_1 while the next result, $a \cdot x_2$, is being computed, and so on. Since the Cray X-MP has eight vector registers, up to seven vectors could appear on the right hand side and be chained (one register is needed for the result vector c_i). In this way, an addition and a multiplication can be computed each clock cycle, leading to the 210 MFLOP theoretical rate.

In FORTRAN (or C), vectorization is implemented in the inner-most do loop. Within the inner-most do loop there must be no subroutine calls or i/o statements because these inhibit vectorization of the loop (as compilers become more sophisticated this statement will no longer be true). Because it is the inner-most loops which are vectorized, these loops should be in general the longest loops (the loop whose index runs over the largest range) and they should not have any dependent statements, where a newly computed result is used in the right hand side of the same assignment during a future pass of the loop. A simple example is:

```
      DO 10 I=1,N
        A(I) = A(I) + A(I-1)
10    CONTINUE
```

This causes a problem because the result A(I) is dependent on the previous value A(I-1). In real codes this problem is often hidden in a statement which uses indirect referencing, like the following finite element example. This loop assembles the element contribution for the IELth element into the global equations, LM(IEL,1-4), for the four local nodes.

```
      DO 10 IEL=1,NEL
        A( LM(IEL,1) ) = A( LM(IEL,1) )  + EL_LOCAL(IEL,1)
        A( LM(IEL,2) ) = A( LM(IEL,2) )  + EL_LOCAL(IEL,2)
        A( LM(IEL,3) ) = A( LM(IEL,3) )  + EL_LOCAL(IEL,3)
        A( LM(IEL,4) ) = A( LM(IEL,4) )  + EL_LOCAL(IEL,4)
10    CONTINUE
```

Where LM(IEL,1) is an integer array of indices, IEL is the element number, and

LM(IEL,1) is the global equation number of the first node of the IELth element. Here the compiler cannot assume that LM(IEL,1) is not equal to LM(IEL-J,1) for some arbitrary J.

Many of the operations in a finite element code (or finite difference code) have this kind of structure and the LM arrays usually have the unfortunate property that LM(IEL,I) is not a unique value (see Figure 2.1 for an example). This is not a fatal problem because we can rearrange the elements (by shuffling the LM array) such that there is a small number of groups of elements that do not share global nodes (Figure 2.2). We can then loop over the total number of groups and over the elements in each group, which are independent and will safely vectorize.

The final point illustrated here is that since we want our inner-most loop to be the loop over the elements, we don't want small loops over the local node numbers (i.e., I=1,4). We unroll the inner-most loop by writing out the expression four times, explicitly putting in the value of the local node in each line (see Appendix D for an example).

2.3 Equations and Implementation

We now turn to the specific example program, ConMan, and discuss in brief the equations and the method used to implement their solutions on a vector computer. We give only a brief description of the numerical method used in ConMan and refer to other work for convergence proofs, stability proofs, and detailed analyses.

The equations for incompressible convection (in dimensionless form) are the equations of

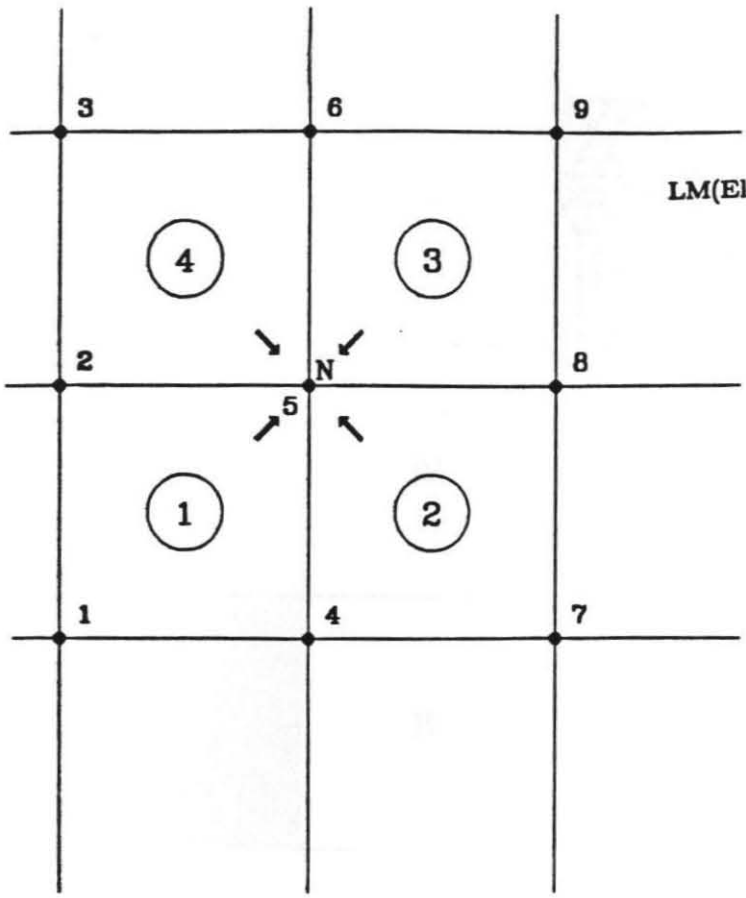

LM(Element number,local node number)

LM(4,1) = 2
LM(4,2) = 5
LM(4,3) = 6
LM(4,4) = 3

Figure 2.1: A schematic two-dimensional finite element grid. The four bilinear quadrilateral elements (circled 1-4) all contribute to the global nodal equation N, which they share in common. The element numbers are circled and the global node numbers are not. The LM array for element 4 is listed at the right.

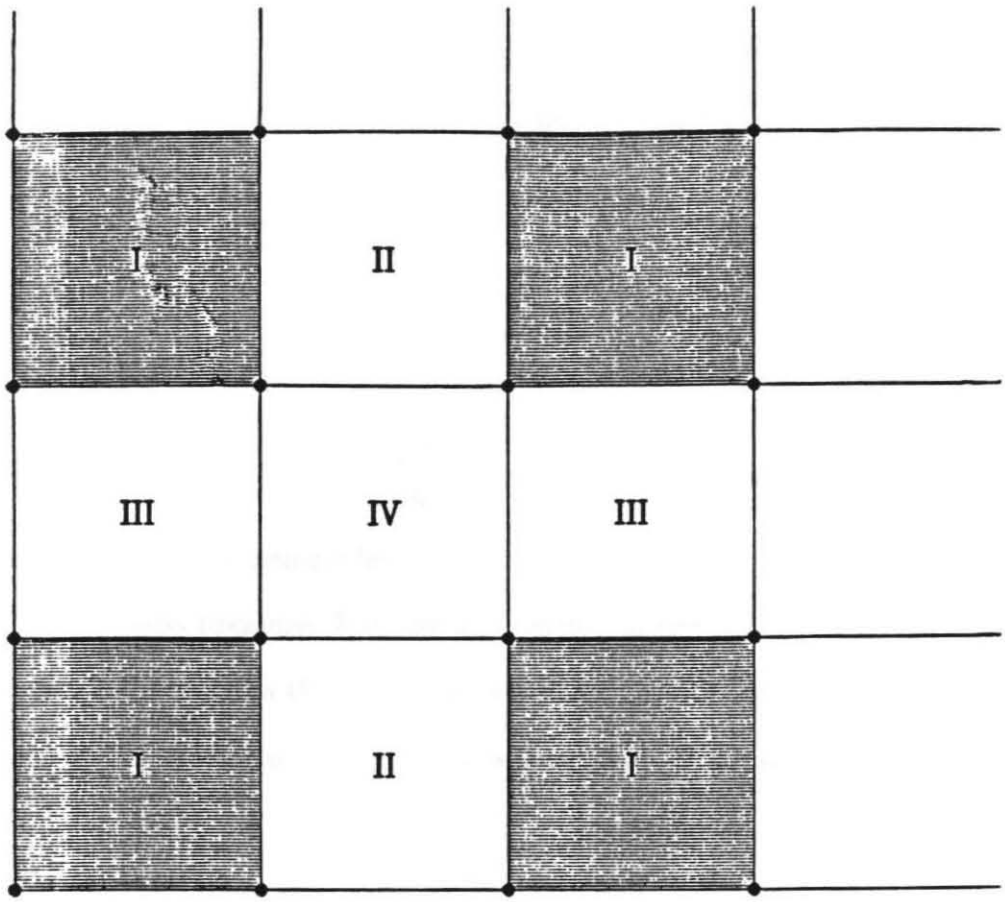

Figure 2.2: An example of the "four color" ordering scheme used in ConMan. Note that the shaded elements (group I) do not share nodes with any other group I element. This group can be operated on safely with a vector operation.

momentum:

$$\nabla^2 u + \nabla p = -\mathrm{Ra}\,\theta\hat{k} \tag{2.3}$$

continuity:

$$\nabla \cdot u = 0 \tag{2.4}$$

and energy:

$$\frac{\partial\theta}{\partial t} = u \cdot \nabla\theta + \nabla^2\theta + H \tag{2.5}$$

where u is the dimensionless velocity, θ is the dimensionless temperature, p is the dimensionless pressure, $\hat{k}$ is the unit vector in the vertical direction, H is the heat source term and t is the dimensionless time. In this form all the material properties are combined into one dimensionless parameter, the Rayleigh number, given by

$$Ra = \frac{\rho g \alpha \Delta T d^3}{\kappa\mu} \tag{2.6}$$

where ρ is the density, g is the acceleration due to gravity, α is the coefficient of thermal expansion, ΔT is the temperature drop across the box, d is the depth of the box, κ is the thermal diffusivity, and μ is the dynamic viscosity.

The momentum and energy equations form a simple coupled system of differential equations. We treat the incompressibility equation as a constraint on the momentum equation and enforce incompressibility in the solution of the momentum equation using a penalty formulation described below. Since the temperatures provide the buoyancy (body force) to drive the momentum equation and since there is no time-dependence in the momentum equation, the algorithm to solve the system is a simple one: given an initial temperature field, calculate the resulting velocity field; use the

velocities to advect the temperatures for the next time step; and solve for a new temperature field. If the time stepping for the temperature equation is stable, then this method is stable and converges as $\Delta t \rightarrow 0$.

The momentum equation is solved using the penalty method to enforce incompressibility. The formal statement of the problem is as follows:

Given:

$$
\begin{aligned}
f &: \Omega \rightarrow \Re^n \qquad \textit{body force vector} \\
g &: \Gamma_g \rightarrow \Re^n \qquad \textit{imposed velocity vector} \\
h &: \Gamma_h \rightarrow \Re^n \qquad \textit{imposed traction vector} \\
\Gamma_g \bar{\cup} \Gamma_h &= \Gamma \\
\Gamma_g \cap \Gamma_h &= \Phi
\end{aligned}
$$

where Γ is the boundary of the domain Ω and Γ_g and Γ_h are the parts of the boundary where velocities and tractions are specified.

Find $u : \Omega \rightarrow \Re^n$ and $p : \Omega \rightarrow \Re$

$$
\begin{aligned}
t_{ij,j} + f_i &= 0 \qquad \textit{on } \Omega \\
u_{i,i} &= 0 \qquad \textit{on } \Omega \\
u_i &= g_i \qquad \textit{on } \Gamma_g \\
t_{ij} n_j &= h_i \qquad \textit{on } \Gamma_h
\end{aligned}
$$

with the constitutive equation for a Newtonian fluid

$$t_{ij} = -p\delta_{ij} + 2\mu u_{(i,j)} \tag{2.7}$$

where t_{ij} denotes the Cauchy stress tensor, p is the pressure, δ_{ij} is the Kronecker delta and $u_{(i,j)} = (u_{i,j} + u_{j,i})/2$.

In the penalty formulation, the above is replaced by

$$t_{ij}^{(\lambda)} = -p^{(\lambda)}\delta_{ij} + 2\mu u_{(i,j)}^{(\lambda)} \tag{2.8}$$

where

$$p^{(\lambda)} = -\lambda u_{i,i}^{(\lambda)} \tag{2.9}$$

and λ is the penalty parameter (repeated subscripts means summation over all indices).

This formulation automatically enforces incompressibility since the solution converges to the incompressible stokes equation as λ approaches infinity (Temam, 1977). Also, the unknown pressure field is eliminated. This is quite useful not only because the amount of computational work is decreased because no pressure equation is solved, but also because it eliminates the need to create artificial boundary conditions for the pressure equation as in many of the early primitive-variable, finite difference formulations (see, e.g., Peyret and Taylor, 1983, pp. 144–156). There are no pressure boundary conditions in the formal specification of the problem.

The equation is cast in the weak form and the Galerkin formulation (i.e. the weighting functions are the same as the basis functions) is used to solve the weak form of the equation.

$$V = \{w \in H^1 \mid w = 0 \quad on\ \Gamma_g\} \tag{2.10}$$

V is the set of all weighting functions w which vanish on the boundary. Similarly V^h is a subset of V parameterized by h, the mesh parameter. Let g^h denote an approximation of g which converges to g as $h \rightarrow 0$.

Find $u^h = w^h + g^h$, $w^h \in V^h$, such that for all $\bar{w}^h \in V^h$

$$\int_\Omega (\lambda w_{j,j}\bar{w}_{i,i} + 2\mu w_{i,j}\bar{w}_{i,j})\, d\Omega = \int_\Omega f_i \bar{w}_i^h d\Omega + \int_{\Gamma_h} h_i \bar{w}_i^h d\Omega$$

$$- \int_\Omega \left(\lambda g^h_{j,j}\bar{w}_{i,i} + 2\mu g^h_{(i,j)}\bar{w}^h_{(i,j)}\right) d\Omega \tag{2.11}$$

$$w_i^h = \sum N_A u_{iA} \tag{2.12}$$

$$u_{iA} = u_i(x_A) \tag{2.13}$$

where N_A is the shape function for node A for the element.

The element stiffness matrix (Figure 2.3) is made up of the two terms from the left hand side of the integral equation. The integration is done using two by two Gauss quadrature, which is exact when the elements are rectangular and bilinear shape functions are used. The λ term is under-integrated (one point rule) to keep the large penalty value from effectively locking the element (Malkus and Hughes, 1978). The right hand side is made up of three known parts, the body force term (f_i), the applied tractions (h_i) and the applied velocities (g_i). The momentum equation is equivalent to an incompressible elastic problem, and the resulting stiffness matrix will always be positive definite (Hughes, 1986 p. 84-89). This allows us to consider only the upper triangular part of the stiffness matrix and save both storage and

$$
[K]^e = \begin{array}{c|cccccccc|c}
i = & 1 & 2 & 3 & 4 & & & & & j = \\
\hline
 & 1 & 2 & 4 & 7 & 11 & 16 & 22 & 29 & \\
 & & 3 & 5 & 8 & 12 & 17 & 23 & 30 & 1 \\
\hline
 & & & 6 & 9 & 13 & 18 & 24 & 31 & \\
 & & & & 10 & 14 & 19 & 25 & 32 & 2 \\
\hline
 & & & & & 15 & 20 & 26 & 33 & \\
 & & & & & & 21 & 27 & 34 & 3 \\
\hline
 & & & & & & & 28 & 35 & \\
 & & & & & & & & 36 & 4
\end{array}
$$

$$
[K]_\nu = \nu \begin{bmatrix} 2N_x(i)N_x(j) + N_y(i)N_y(j) & N_x(j)N_y(i) \\ N_x(i)N_y(j) & N_x(i)N_x(j) + 2N_y(i)N_y(j) \end{bmatrix}
$$

$$
[K]_\lambda = \lambda \begin{bmatrix} N_x(i)N_x(j) & N_x(i)N_y(j) \\ N_x(j)N_y(i) & N_y(i)N_y(j) \end{bmatrix}
$$

Figure 2.3: a) The location and numbering of the 8 by 8 element stiffness matrix for the velocity equation used in ConMan. Note that the matrix is made up of sixteen 2 by 2 matrices with i,j indices as shown. The i and j refer to the local node numbering of the element and can be thought of as the effect of node i as felt at node j. Each 2 by 2 matrix is made up of two terms: b) a viscosity contribution $[K]^e_\nu$, and c) a penalty contribution $[K]^e_\lambda$. $N_x(i)$ is the x derivative of the shape function evaluated at node i. (The ij's refer to the location of the 2 by 2 matrix in the 8 by 8 element stiffness matrix).

operations using Cholesky factorization. More details of the method and a formal error analysis can be found in Hughes, Liu and Brooks (1979).

The energy equation is an advection-diffusion equation. The formal statement is:

Find $T : \Omega \rightarrow R$ such that

$$\begin{aligned} \dot{T} + u_i T_{,i} &= \kappa T_{,ii} + H \quad on\ \Omega \\ T &= b \quad on\ \Gamma_b \\ T_{,j} n_j &= q \quad on\ \Gamma_q \end{aligned}$$

where T is the temperature, u_i is the velocity, κ is the thermal diffusivity and H is the internal heat source. The weak form of the energy equation is given by

$$\begin{aligned} \int_\Omega (w + p)\, \dot{T}\, d\Omega = &- \int_\Omega (w + p)\, (u_i T_{,i})\, d\Omega - \kappa \int_\Omega w_{,i} T_{,i}\, d\Omega \\ &+ \int_{\Gamma_q} w\, T_{,j} n_j\, d\Gamma_q \end{aligned} \tag{2.14}$$

where $\dot{T}$ is the time derivative of temperature, $T_{,i}$ is the gradient of temperature, w is the standard weighting function and $(w + p)$ is the Petrov-Galerkin weighting function with p, the discontinuous streamline upwind part of the Petrov-Galerkin weighting function, given by

$$p = \tau u \cdot \nabla T = \tilde{k} \frac{u_i w_{,i}}{||u||^2} \tag{2.15}$$

The energy equation is solved using Petrov-Galerkin weighting functions on the internal heat source and advective terms to correct for the under-diffusion and remove the oscillations which would result from the standard Galerkin method for an advection dominated problem (Hughes and Brooks, 1977). The Petrov-Galerkin function

can be thought of as a standard Galerkin method in which we counterbalance the numerical underdiffusion by adding an artificial diffusivity of the form:

$$\left(\xi u_\xi h_\xi + \eta u_\eta h_\eta\right)/2 \tag{2.16}$$

with

$$\xi = 1 - \frac{2\kappa}{u_\xi h_\xi} \tag{2.17}$$

$$\eta = 1 - \frac{2\kappa}{u_\eta h_\eta} \tag{2.18}$$

where h_ξ and h_η are the element lengths and u_ξ and u_η are the velocities in the local element coordinate system (ξ η system) evaluated at the element center. This form of discretization has no crosswind diffusion because the "artificial diffusion" acts only in the direction of the flow (i.e., it follows the streamline), hence the name Streamline Upwind Petrov-Galerkin (SUPG). This makes it a better approximation than straight upwinding and it has been demonstrated to be more accurate than Galerkin or straight upwinding in advection dominated problems (Hughes and Brooks, 1977). It has recently been shown that the SUPG method is one of a broader class of methods for advection-diffusion equations referred to as Galerkin/Least-Squares methods (Hughes *et al.*, 1988).

The resulting matrix equation is not symmetric, but since the energy equation only has one degree of freedom per node, while the momentum equation has two or three, the storage for the energy equation is small compared to the momentum equation. Since we use an explicit time stepping method, the energy equation is not implemented in matrix form. The added cost of calculating the Petrov-Galerkin weighting functions is much less than the cost of using a refined grid with the Galerkin

method. The Galerkin method requires a finer grid than the Petrov-Galerkin method to achieve stable solutions (Travis *et al.*, 1990).

Time stepping in the energy equation is done using an explicit predictor-corrector algorithm. The form of the predictor-corrector algorithm is:

Predict:

$$\dot{T}_{n+1}^{(0)} = 0 \tag{2.19}$$

Solve:

$$M^* \Delta \dot{T}_{n+1}^{(i)} = R_{n+1}^{(i)} \tag{2.20}$$

$$R_{n+1}^{(i)} = - \left[\dot{T}_{n+1}^{(i)} + u \cdot (T_{n+1}^{(i)})_{,x} \right] (w + p) -$$

$$\tilde{k}\, w_{,x} (T_{n+1}^{(i)})_{,x} + (\textit{boundary condition terms}) \tag{2.21}$$

Correct:

$$T_{n+1}^{(i+1)} = T_{n+1}^{(i)} + \Delta t \alpha \dot{T}_{n+1}^{(i)} \tag{2.22}$$

$$\dot{T}_{n+1}^{(i+1)} = \dot{T}_{n+1}^{(i)} + \Delta \dot{T}_{n+1}^{(i)} \tag{2.23}$$

where i is the iteration number (for the corrector), n is the time step number, T is the temperature, $\dot{T}$ is the derivative of temperature with time, $\Delta \dot{T}$ is the correction to the temperature derivative for the iteration, M^* is the lumped mass matrix, $R_{n+1}^{(i)}$ is the residual term, Δt is the time step and α is a convergence parameter. Note that in the explicit formulation M^* is diagonal.

The time step is dynamically chosen, and corresponds to the Courant time step (the largest step that can be taken explicitly and maintain stability). With the appropriate choice of variables, $\alpha = 0.5$ and two iterations, the method is second order accurate (Hughes, 1986, p.562-566).

2.4 Numerical Benchmarks

Two examples are given, based on benchmarks for two-dimensional Cartesian convection codes given in Travis et al., 1990. The parameters for these benchmarks are given in Table 1. There are two purposes for these benchmarks: first, to verify the code against standard existing codes; and second, to demonstrate the speed of the vector code on representative problems. Benchmark CVBM has a constant viscosity, and the velocity stiffness matrix is only factored once while TDBM (not from Travis *et al.*) has a temperature-dependent viscosity law and the velocity stiffness matrix is factored every time step. This allows us to observe the difference between the speedup in the finite element forms and assemblies and the matrix factorization and backsubstitution.

Vectorizing sparse matrix solvers is an area of active research (e.g., Ashcraft *et al.*, 1987, Lucas, 1988), and our implementation has used a standard and poorly vectorized solver. Therefore, we present the times in individual units of the program as well as the total times. Results are given for a Convex-C120 running Unix compiled with fc4.1, a Convex-C210 running Unix compiled with fc5.0, a Cray X-MP/48 running CTSS, compiled with CFT77, a Cray 2 (one processor) running Unicos and a Cray Y-MP (one processor), also running Unicos. (We list compilers and operating systems since we found a factor of up to 1.5 difference in speed between code compiled with different compilers on the same machine!) We present execution speed relative to the Cray X-MP scalar speed (Table 2), since that is comparable to the vector speed of the original code upon which ConMan was based. Notice that a well vectorized code runs better on mini-supercomputers like the Convex C120 and C210

Parameters	Benchmark	
	CVBM	TDBM
Rayleigh Number	77927	100000
Time Steps	5000	1000
Tempdep Viscosity	no	yes
Temp B.C. -top	T=0	T=0
Temp B.C. -bottom	T=1	T=1
Internal Heating	no	no

Table 2.1: Table of parameters for benchmark timing information. Tempdep viscosity requires a matrix factor every time step, otherwise the matrix can be factored only once and a backsolve is done every time step.

than scalar codes on the Crays. Hardware monitoring for CVBM gives an overall rate of 65 MFLOPS on the X-MP (95 MFLOPS on the faster Y-MP). TDBM, with an overall rate of 45 MFLOPS on the Y-MP, is slower because more time is spent factoring, a routine which is not well vectorized. A breakdown of the execution time spent in each of the major routines is given in Table 3.

We note that an old version of the SUPG (Streamline Upwind Petrov-Galerkin) code on which ConMan is based ran slower in vector mode than ConMan does in scalar. This indicates that even though the compiler indicated it was vectorizing many loops in the old code, either the time consuming calculations were not being vectorized or the loops were too short to see any appreciable speedup. We also note that ConMan runs faster on a Sun 4-330, which is a scalar machine, than the old SUPG code (a common finding of people who vectorize and optimize codes).

From the benchmark timings it is clear that the element assembly routines (f_vStf, f_vRes, f_tRes) have been improved significantly more than the factorization and backsubstitution routines. We note that faster fully vectorized matrix solvers are being developed especially for finite element programs (e.g., Lucus, 1988). We designed ConMan so that it can be easily adapted to a new matrix solver when one becomes available.

The routine times don't add up to the total times because there are unlisted routines (for grid generation and i/o) that take a small amount of time. The MFLOP rates and relative speeds, however, do include time spent in these routines. Note that the speedup, the ratio of scalar to vector speed, on the Convex is not as good as on the Crays. This is because in double precision the Convex memory access time,

Computer	Benchmark	
	CVBM	TDBM
Cray Y-MP V	31.18	26.07
Cray X-MP V	18.73	15.29
Cray 2 V	15.92	10.62
Convex C210 V	4.27	3.10
Convex C120 V	1.40	1.42
Ardent Titan V	1.23	1.54
Cray X-MP S	1.00	1.00
Sun 4-330	0.42	0.79
Sun SS1	0.37	0.61
Convex C120 S	0.31	0.42
Ardent Titan S	0.27	0.28

Table 2.2: Execution speeds normalized to the Cray X-MP scalar execution speed for the two benchmark problems (CVBM and TDBM) on various computers. Where available, both scalar (S) and vector (V) speeds are shown. The speedup (the ratio of scalar to vector times) is greater on the Crays because the slower memory access on the Convex limits vector performance.

Timings for Subroutines from BM1				
Subroutine	Convex		Cray X-MP	
	scalar	vector	scalar	vector
factor	10.4	3.6	4.8	0.3
backsolve	3132.2	830.2	1341.5	80.0
f_vStf	1.6	0.4	0.6	0.1
f_vRes	531.0	92.9	154.4	6.6
f_tRes	5272.3	948.7	1212.4	50.9
Timings for Subroutines from BM3				
Subroutine	Convex		Cray X-MP	
	scalar	vector	scalar	vector
factor	10883.4	3564.9	4870.0	297.1
backsolve	646.9	167.3	270.2	16.4
f_vStf	1690.0	417.1	649.5	71.3
f_vRes	112.9	19.5	30.6	1.4
f_tRes	1088.5	188.0	242.4	9.8

Table 2.3: Execution times (in seconds) for individual routines for benchmarks BM1 and BM3 in scalar and vector mode on various computers. Note that the assembling routines (f_vStf, f_vRes, f_tRes) show better vector performance than the factor and backsubstitution routines. The performance of the factor and backsolve improves as the bandwidth of the matrix approaches the vector register length.

especially in the indirect referencing, is slowing the vector calculations. The Convex is simply not able to deliver numbers fast enough to the vector registers. Since the Cray X-MP and Y-MP have three paths to memory, as well as a faster memory access time, they are not limited by memory access. Also, because of the Cray's larger word size we can use single precision on the Cray with the same accuracy as double precision on the Convex.

Plots of the final temperature field and the difference from a finite-difference calculation on a 129 by 129 grid from Travis *et al.* (1990) are shown in Figure 2.4. The solution for benchmark CVBM agrees quite well with the Travis et al. benchmark. Since error goes as $O((\Delta x)^2)$, where Δx is the grid spacing, the error associated with the high resolution grid is more than an order of magnitude less than the 33 by 33 grid used for CVBM. Taking the 129 by 129 result as the exact solution, the difference plot (Figure 2.4b) shows the error in the SUPG method. The SUPG method has localized the error in the corner regions where the flow is most advective, and compares exactly with the sequential SUPG method code used in the benchmark paper (see Travis *et al.* for more details of the error associated with the method).

2.5 Summary

In addition to the traditional modifications for vectorization (removing subroutine calls and i/o statements from the inner loops, etc.) we believe that data structure is an important consideration for codes used on vector computers. We have presented some simple ideas for improving code performance on vector computers, specifically

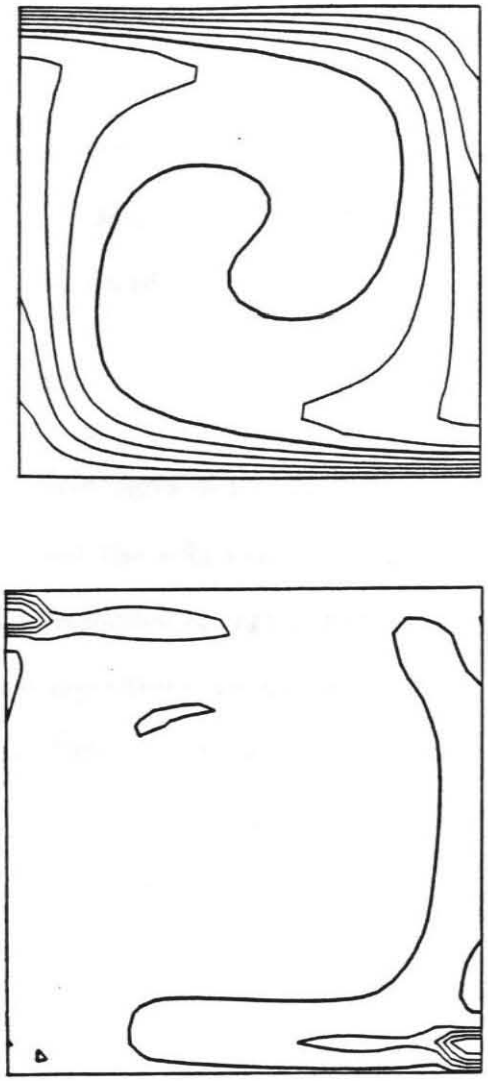

Figure 2.4: a) Final temperature field for CVBM. The contour interval is 0.1 dimensionless temperature units. The heavy contour is the 0.5 contour line. b) Difference of final temperature field above and the high resolution 129 by 129 grid from Travis *et al.* (1990). The contour interval is 0.002 dimensionless temperature units. The heavy contour is the 0.0 contour line.

in the improvement of data structures. These ideas work not only on small linear algebra routines but can also be extended to full scale scientific programs and still retain order of magnitude speedups. We have implemented these ideas in a new finite-element code, ConMan, designed for studying problems in mantle convection, which takes advantage of the speed available on today's vector supercomputers.

2.6 Additional Notes

The computationally intensive parts of the finite element method are typically the individual element forms and the solution of the global stiffness matrix. Both of these functions have been vectorized in high performance codes. To further increase computational speed, new algorithms are needed. A multifrontal sparse solver has been developed by Lucas (1988) and incorporated into ConMan (King, Lucas and Raefsky, 1990). The multifrontal solver uses the Multiple-Minimum Degree reordering heuristic to reduce the number of operations required to factor a sparse matrix. The reordered matrix has dense blocks and full matrix computational kernels (e.g., BLAS3) can be used to enhance vector performance.

For large problems, ConMan runs 9.5 times faster with the new sparse solver. The speedup perceived by the user is typically even greater because the multifrontal version of the code requires less storage and less CPU time, thus it can be run in higher priority scheduling queues.

The original version of ConMan, run on a VAX 11/780 took about 8 hours of CPU time for BM1. The total speed-up as perceived by the user, including improvements in both the algorithm and the hardware, is 450. It is important to remember that

this is for the smallest of the sample problems. Larger problems were simply not feasible.

Solutions for CVBM were provided by Brian Travis and were done as part of the IGPP Mantle Convection Workshop at Los Alamos National Laboratory. Helpful videotape lectures on vectorizing code and Cray architecture were obtained at the Los Alamos National Laboratory. Cray X-MP calculations were performed at the San Diego Supercomputer Center. Cray 2 and Cray Y-MP calculations were performed at NASA Ames with the help of Eugene Miya. Convex C210 calculations were performed by Ron Gray at Convex Computer Corporation. Sun 330 calculations were performed by Keith Bierman at Sun Microsystems, Inc. Appendix A contains a more extensive list of benchmark times.

Chapter 3

On Rheology: The Relationship Between Plate Velocity and Trench Viscosity in Newtonian and Power-Law Subduction Calculations

3.1 Introduction

The subduction of oceanic lithosphere plays a major role in the mass and heat transport in the Earth. Since so much of our knowledge of the mantle comes from observations in subduction regions, it is important to understand the dynamics of slabs. The rheology of slabs is very important to the dynamics of slabs. Slab rheology could play a major role in the deformation of the 670 kilometer discontinuity. For example, strong slabs could penetrate a chemical barrier more easily than weak slabs

(Christensen and Yuen, 1984).

The rheology of a material is controlled by the mechanisms of deformation. A constitutive law, which relates the stress and the strain-rate, is derived from these mechanisms and the viscosity (hence rheology) enters into these constitutive laws. The mechanisms by which minerals deform at the temperature and pressure ranges in subducted slabs are not well understood. The mantle may deform by diffusional flow (McKenzie, 1967; 1968), power-law creep (Weertman, 1970) or plastic failure (Ashby and Verrall, 1977). Geophysical and geochemical evidence indicates that olivine is the dominant mineral in the upper mantle (e.g., Birch, 1969; Ringwood, 1970). Laboratory measurements of flow properties of natural dunite, a mineral consisting of mostly olivine, at high temperature are best fit by a power-law constitutive law (e.g., Ashby and Verrall, 1977; Chopra and Patterson, 1981; Yuen, Sabadini and Boschi, 1983). Stresses in the mantle are likely to be largest in the cold lithosphere and slab, so if power-law deformation is important, it is likely to have the greatest effect in slabs and trenches. The fact that earthquakes occur in deep slabs may also indicate that some of the failure takes place by brittle fracture.

Convection in a Newtonian fluid (linear constitutive law) with a temperature-dependent viscosity leads to a convecting system with little or no motion at the surface (e.g., Nataf and Richter, 1982). Since plate tectonics is a major feature of the dynamics of the Earth, many convection studies have included moving plates using a variety of techniques. These range from integrating tractions along predefined plate boundaries (e.g., Richter and McKenzie, 1978; Hager and O'Connell, 1981) to using complicated viscosity laws to create strong plates and a relatively uniform mantle

with a weak region at the subduction zone (e.g., Christensen and Yuen, 1984).

In order to simulate "plate-like" behavior (i.e., uniform surface velocity and relatively low intraplate stress with asymmetric subduction) weak zones can be imposed at subducting regions and ridges (e.g., Schmeling and Jacoby, 1981; Davies, 1986; Gurnis and Hager, 1988). Because subducting regions are the highest stress regions, a stress-weakening rheology generates weak zones at subducting regions in a self-consistent fluid dynamical model, without requiring that they be specified *a priori*. However, the weak zones might simulate fracture or some other process not included in viscous flow models.

Surface velocities in non-Newtonian (non-linear constitutive law) systems can exhibit uniform plate-like behavior for a reasonable choice of parameters (Cserepes, 1982; Christensen, 1983; 1984). For steady-state flow, Parmentier, Torrance and Turcotte (1976, 1978) showed that Newtonian flows and non-Newtonian flows in a unit aspect ratio box are nearly the same when the viscosity used in the Rayleigh number scaling of the non-Newtonian flow is the average viscosity of the flow. Christensen (1983, 1984) showed strong similarities between non-Newtonian temperature-dependent calculations and Newtonian temperature-dependent calculations with the same scaling of the Rayleigh number and decreasing the Newtonian activation energy by $1/n$ where n is the exponent in the power-law relation. However, Christensen points out significant differences in time-dependent flows between Newtonian and non-Newtonian fluids. As we will show, this scaling may be somewhat fortuitous because the unit aspect ratio box severely restricts the flow.

Whether imposed *a priori* as a weak zone in a Newtonian model or resulting from

high stress in a power-law model, the effective viscosity of the weak zone is directly related to the plate velocity, and is therefore an important parameter in subduction models. We examine a range of weak zone viscosities using Newtonian rheologies to understand the effect of this parameterization of the weak zone on plate velocity. We then compare these calculations to non-Newtonian convection calculations with plates and slabs.

We examine the temperature-dependence of viscosity in a Newtonian rheology, including several viscosity laws used in recent subduction studies, and compare them to the temperature-dependence predicted by the deformation mechanisms. Hager and O'Connell (1981) point out that the plate velocities in their models are nearly independent of the lithosphere (plate) viscosity, as long as the viscosity of the lithosphere is much greater than the viscosity of the asthenosphere. This is because in the Hager and O'Connell calculations the plates were driven by the tractions at the base of the lithosphere, which are independent of the viscosity of the lithosphere, and the lithospheric deformation law included a yield stress. We examine the effect of increasing and decreasing the total variation of the viscosity for steady flows.

Next we examine Newtonian calculations with imposed weak zones. Since the weak zone doesn't have a direct physical interpretation, models where the solution depends on the weak zone parameterization could be misleading. We vary the size of the weak zone and its location relative to the initial downwelling in an attempt to assess the independence of the "slab-like" features on the weak zone parameterization. We also examine the effect of the viscosity of the weak zone with temperature-dependent rheology.

Finally, we discuss temperature-dependent power-law rheology. We show that plate-like surface velocities and slab-like downwellings are possible in convection calculations with reasonable choices for the Rayleigh number and activation energy. We also find that no weak zones are needed at the trench with non-Newtonian calculations, while a weak zone is still needed at the ridge. It is possible that some mechanism other than strain weakening, such as partial melting or fracture, plays a role in reducing the effective viscosity near the ridge. Without a ridge weak zone, the non-Newtonian plates have unrealistically high strain accumulations within the plate.

3.2 Newtonian versus Non-Newtonian Rheology

We first examine Newtonian flows using imposed strong and weak zones to better understand how the viscosity of the weak zones affects the flow. To do this, we use a series of calculations in a Cartesian box with six zones, each of which can have a different viscosity (Figure 3.1). The largest zone has a uniform background viscosity, representing most of the mantle. The two long, narrow zones are high-viscosity zones, simulating the effects of temperature-dependence, representing the plate and the slab. The three small zones are low-viscosity (weak) zones to allow deformation at the "ridge," the "trench" and the "tip" of the slab.

We carry out a series of calculations with different weak zone viscosities and plate/slab viscosities. The viscosities of the plate and slab are set equal to each other, although this may not be realistic for the Earth. A weak zone is needed at the ridge and is always fixed to be 1/100 times the mantle viscosity. This simulates the effects

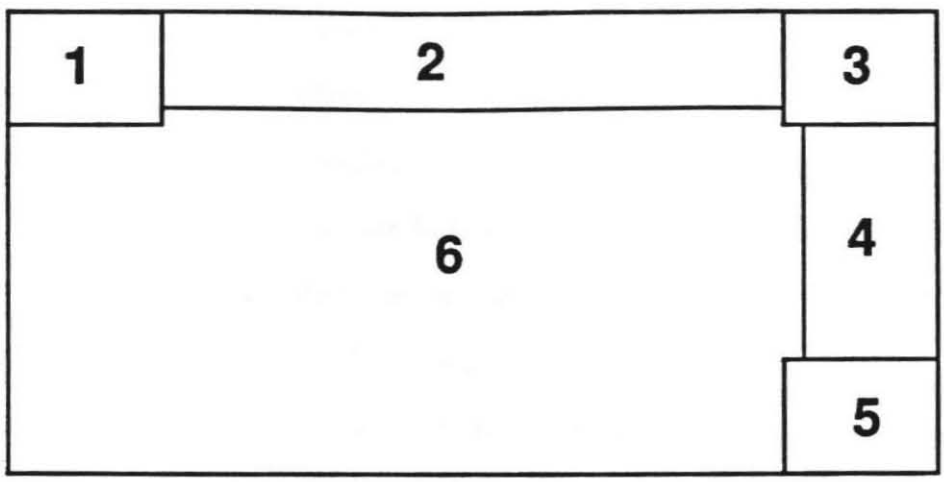

Figure 3.1: The material zones used for the Newtonian calculations. Zones 1,3, and 5 are "weak zones" to allow deformation at the ridge, trench, and tip of the slab. Zones 2 and 4 are strong zones to simulate the temperature-dependent rheology.

of temperature dependent rheology; the temperatures near the ridge are higher and boundary layer is thinner there. Partial melting may also play a role in decreasing the viscosity near the ridge. Plate/slab viscosities need to be at least 100 times the mantle viscosity for "plate-like" behavior (i.e., low intraplate strain or uniform velocity). Increasing the plate viscosity up to 10,000 times the mantle viscosity does not change the solution significantly. The effect of the plate/slab viscosity on the steady surface velocities is shown in Figure 3.2. Notice that increasing the plate/slab viscosities greater than 100 times the viscosity has almost no effect on the solution.

The viscosities of the weak zones at the trench and slab tip play important roles in the development of the flow. For the calculations shown, the viscosities of these two regions were equal. Figure 3.3 shows the plate and slab velocities as a function of the trench/tip viscosity, normalized to the mantle viscosity. The Rayleigh number is 2.0×10^5. Results for Rayleigh numbers up to 10^7 and plate/slab viscosities from 100 to 10,000 times the mantle viscosity agree qualitatively with Figure 3.3. The size of the weak zones is not a factor as long as the weak zone is at least as deep as the plate and as wide as the slab to keep the plate and slab from locking.

The graph can be simplified to three regions of characteristic behavior. If the weak zone viscosity is comparable to the plate viscosity (the far right portion of Figure 3.3), then the plate and slab are almost stationary and large shear tractions build up at the base of the plate. This agrees with experiments showing that temperature-dependent viscosity leads to flows with little or no surface motion (Nataf and Richter, 1982). For viscosities much less than the mantle viscosity (far left of Figure 3.3), the plate and slab velocities tend toward asymptotic values and large shear tractions do

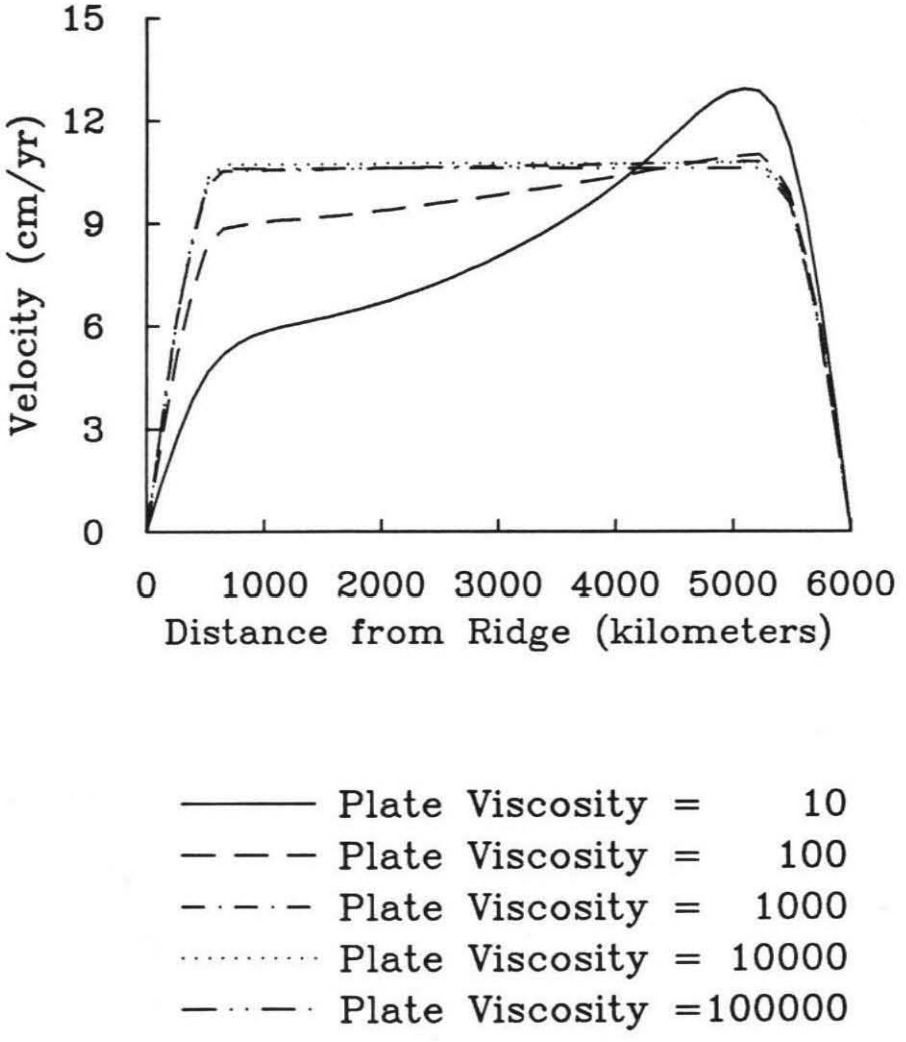

Figure 3.2: Surface velocities for various plate/slab viscosities. In all calculations the Rayleigh number is 10^6 and the weak zone viscosity is 10^{-3}.

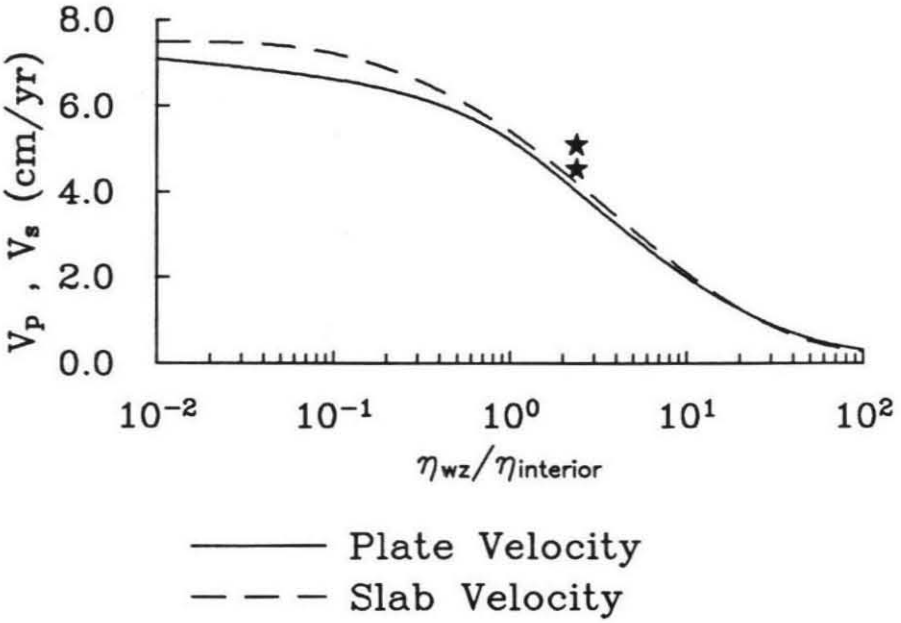

Figure 3.3: Steady plate and slab velocities as a function of weak zone viscosity (zone 3 and 5), η_{wz}. Temperature-dependence is simulated by imposing the plate and slab viscosity, η_{plate} to be 1000 times the interior viscosity. The Rayleigh number for all calculations is 2.0×10^5. The stars represent the plate and slab velocities for a non-Newtonian calculation with a plate, slab and weak zone preexponential viscosity 1000 times the interior viscosity. The effective Rayleigh number for the non-Newtonian model, the formal Rayleigh number divided by the strain-rate averaged viscosity (after Parmentier *et al.*, 1976), is also 2×10^5.

not build up at the base of the plate. For weak zone viscosities comparable to the mantle viscosity, there is an inverse relationship between weak zone viscosity and plate velocity, with lower viscosities giving higher plate velocities. The flow pattern in the mantle region for all the calculations in this intermediate range is similar; the main differences in these calculations are the plate and slab velocities and the velocities directly beneath the plate and adjacent to the slab. The mantle velocities for the calculations with weak zone viscosities much less than the mantle viscosity are significantly faster than the mantle velocities for the calculations with weak zone viscosities between the mantle and plate/slab viscosity.

The stars on Figure 3.3 represent plate and slab velocities for a non-Newtonian model with the same effective Rayleigh number, defined using the strain-rate average viscosity (Parmentier, Torrance and Turcotte, 1976; Parmentier, 1978). The viscosity ratio plotted in Figure 3.3 is determined by averaging the effective viscosities over the same regions as shown in Figure 3.1. Both plate and slab velocities are slightly higher and the ratio of slab to plate velocity is somewhat greater for the non-Newtonian calculation than for the Newtonian one. In both the Newtonian and non-Newtonian flows, the strain-rate in the slab from 75 to 150 km (to compare with Bevis, 1986) is 2×10^{-15}/sec.

For comparison, the temperature fields from the non-Newtonian calculation and the equivalent Newtonian calculation are shown in Figure 3.4, along with the effective viscosities for both calculations. The slab velocities differ by up to 10%. This differs from the results of Parmentier, Torrance and Turcotte (1976) and Christensen (1983, 1984) who found that for steady-state flows, Newtonian flows more closely resemble

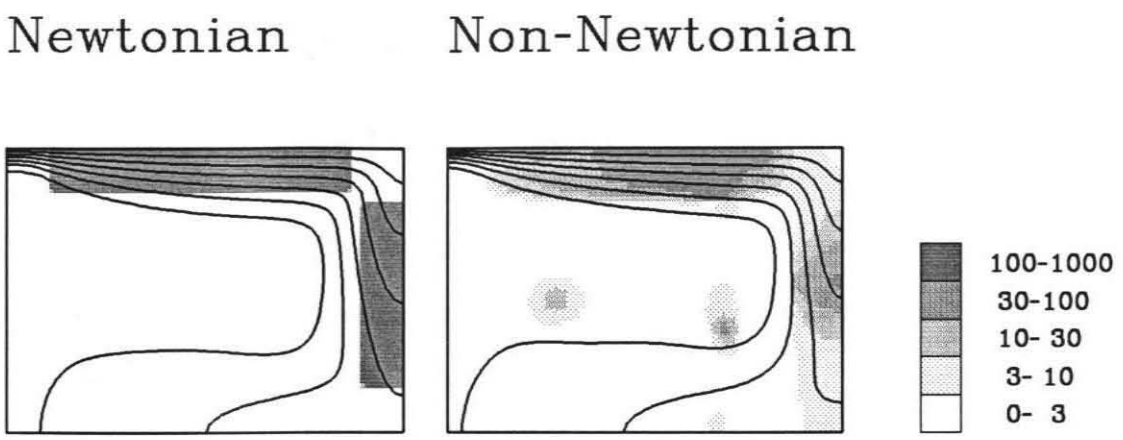

Figure 3.4: Steady-state Newtonian temperature (contours) and viscosity (shading) fields with a plate-slab viscosity equal to 1000 (zones 2, 4 and 5) and a weak ridge and trench (zones 1 and 3) and a steady-state non-Newtonian calculation with the same plate and slab viscosity but a strong trench ($\eta_{trench} = \eta_{plate}$). The effective Rayleigh numbers for the two calculations are equal. The weak trench simulates the non-Newtonian rheology at the trench. Contour intervals shown are for 0.02, 0.04, 0.06, 0.08, 0.1 and 0.12 dimensionless temperature units.

non-Newtonian flows with a simple scaling of the Rayleigh Number and the activation energy (for the temperature-dependence). Despite the relatively large differences in velocity, the temperature fields differ by less than 1% . Christensen and Yuen (1989) showed that the similarity between Newtonian and non-Newtonian flows breaks down when the flows become time-dependent, but the solutions in Figure 3.4 are steady.

3.3 Temperature-Dependence

We will return to the effect of stress on rheology in section 3.4. The effect of temperature on rheology is independent of mechanism because it enters through the vacancy diffusion coefficient, D, which has the form

$$D = D_o \exp(-E^*/RT)$$

where E^* is the activation energy, R is the gas constant and T is the temperature. This leads to a temperature-dependent viscosity of the form

$$\eta(T) = \eta_o \exp(E^*/RT)$$

which is shown graphically in Figure 3.5 for olivine, whose creep properties are best known of all mantle minerals. The experimental data is fit by $D_o = 0.1\ m^2/s$ and $E^* = 522$ kJ (Ashby and Verrall, 1977). As a rule of thumb, the viscosity decreases by at least one order of magnitude for every 100 °K increase in temperature. This is shown as a dashed line in Figure 3.5. The viscosity is scaled so that at 1473 °K it has a value of 1.

Rayleigh number scaling becomes less clear with temperature dependence. The

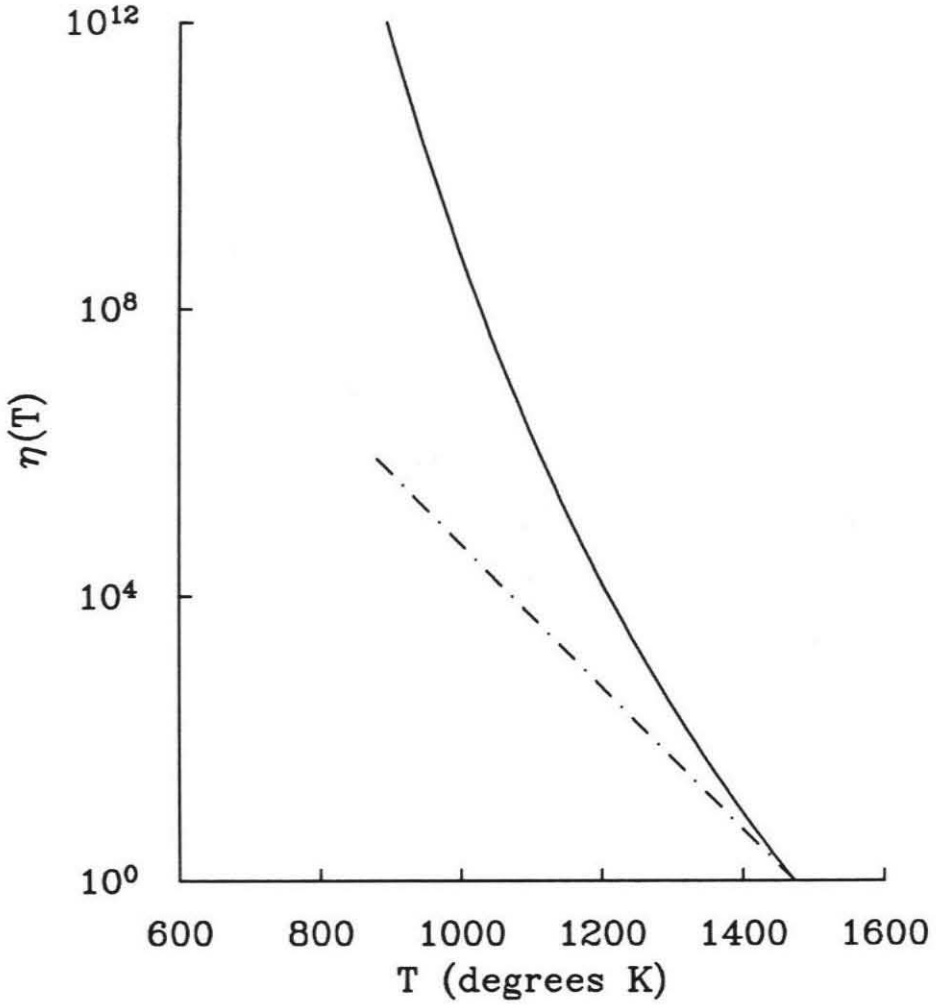

Figure 3.5: Temperature-dependence of viscosity for olivine (solid line) from Ashby and Verrall (1977), compared with a one order of magnitude increase in viscosity per 100 °K (dot-dash line). The viscosity is scaled such that at 1473 °K the viscosity is 1.

Rayleigh number is defined as

$$Ra = \frac{g\alpha\Delta T d^3}{\kappa\eta}$$

where g is the gravitational acceleration, α is the coefficient of thermal expansion, ΔT is the temperature difference across the top and the bottom of the box, d is the depth of the box, κ is the thermal diffusion and η is the kinematic viscosity. The formal definition of the Rayleigh number is for an isoviscous problem (Chandraesekhar, 1961) so η is a constant. Richter, Nataf, and Daly (1983) and Christensen (1984) showed that for many relations the appropriate viscosity is the average viscosity of the system. Unfortunately, since that depends on the final temperature distribution, the Rayleigh number is no longer known *a priori*, but becomes a part of the solution. We choose to define the temperature-dependence of viscosity as

$$\eta(T) = \eta_o \exp\left(\frac{E^*}{T + T_o} - \frac{E^*}{1.0 + T_o}\right)$$

η_o is the pre-exponential viscosity, $\eta(T)$ is the effective viscosity, T is the dimensionless temperature, E^* is the dimensional activation energy divided by $R\Delta T$, where R is the gas constant and ΔT is the temperature scaling (for reference $E^*/R\Delta T \approx 60$ for olivine). T_o is the temperature offset, since dimensionless $T = 0$ is actually 273° Kelvin. The second term in the exponential scales $\eta(T)$ such that $\eta(1) = \eta_o$. We then use η_o in the definition of the Rayleigh number. Since we use $T = 1$ in the interior of our subduction calculations this scaling is equivalent to defining a Rayleigh number based on the interior of the flow.

A simple constitutive law with such a large variation in viscosity probably does not accurately describe the deformation of the mantle because at low temperatures

other deformation mechanisms become the dominant mechanism of deformation (Ashby and Verrall, 1977). In numerical convection calculations, where the mantle is typically modeled as a viscous fluid with either a Newtonian or power-law viscosity, it is not clear what constitutive law is most appropriate. A number of temperature-dependent laws have been used based both on reasonable assumptions about the rheology and numerical limitations (e.g., Gurnis and Hager, 1988; Davies, 1988). These are plotted in Figure 3.6, along with our viscosity definition with several different values of E^*.

Numerically, because of the finite precision of computers, it is only possible to solve Stokes flow problems with a few orders of magnitude variation in viscosity. With a finite element method using a penalty formulation and a direct solver (ConMan), our experience shows that variations up to six orders of magnitude are numerically possible. For iterative and spectral methods two orders of magnitude are about the maximum viscosity variation possible (e.g., Davies, 1988).

The total variation in viscosity can be almost as important as the functional form of the viscosity variation with temperature. This is illustrated in Figure 3.7, where we present six steady solutions of a temperature-dependent calculation with a Rayleigh number of 10^6 in a unit aspect ratio box. For the calculations in Figure 3.7, $E^* = 6.0$ (one tenth the activation energy for olivine given in Ashby and Verrall) and $T_o = 0.2275$, corresponding to $\Delta T = 1200$ °C and a surface temperature of 0 °C. The only parameter allowed to vary in the calculations shown in Figure 3.7 is the maximum allowed viscosity. Specifically, the algorithm used is: if $\eta(T)$ is greater than $\eta_{cut-off}$, then $\eta(T) = \eta_{cut-off}$. Five different values of $\eta_{cut-off}$ are shown, along

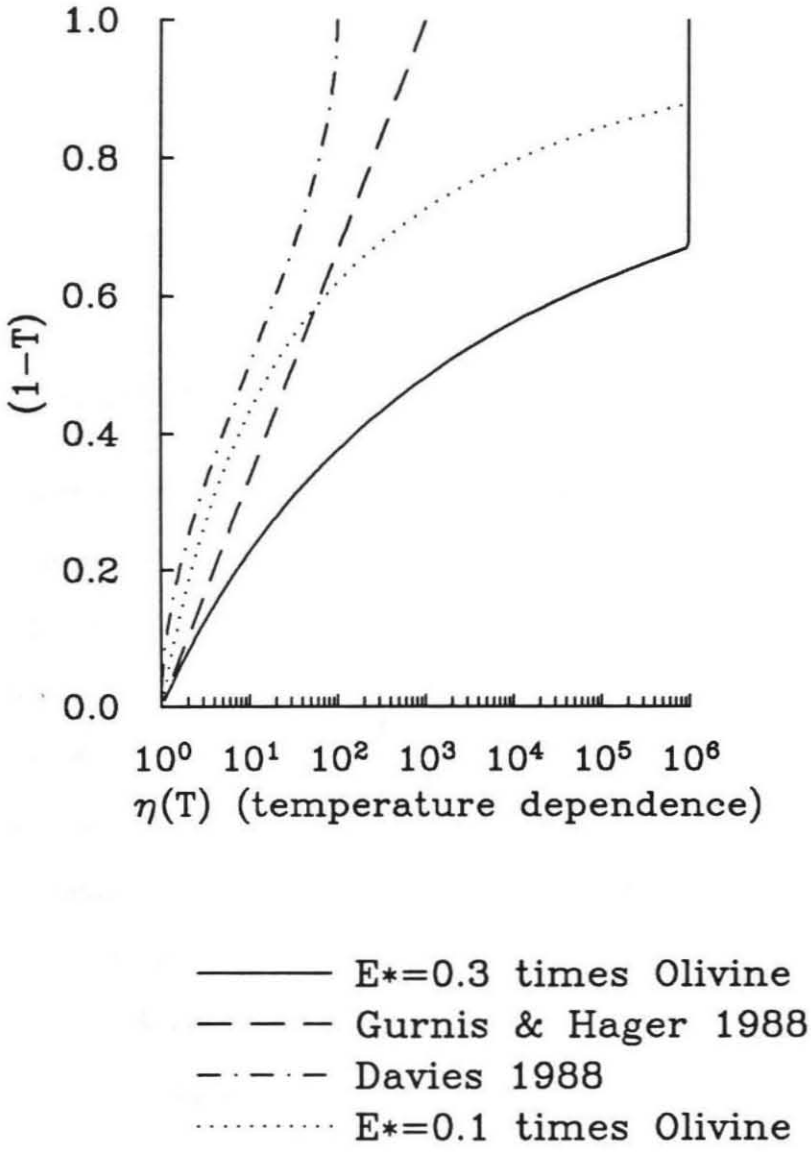

Figure 3.6: Various temperature-dependent viscosity laws. The vertical axis is plotted as 1-T (temperature) so that colder temperatures are at the top. The horizontal axis is the log of the viscosity, scaled so that at T=1 the viscosity is 1.0.

with a constant viscosity calculation for comparison. Notice that $\eta_{cut-off} = 10$ looks very similar to the constant viscosity case for this activation energy. Also, the calculations with $\eta_{cut-off} \geq 10^4$ are nearly the same. Figure 3.8 shows the Nusselt number versus $\eta_{cut-off}$, demonstrating quantitatively the difference between the flows.

3.4 Weak Zones

For numerical subduction calculations, weak zones are often added at the trench to soften the boundary layer and cause "subduction" (Kopitzke, 1979; Schmeling and Jacoby, 1981; Christensen, 1983; Gurnis and Hager, 1988; Davies, 1989). We investigate the effect of varying the size and viscosity of the weak zone for several temperature-dependent models.

First we consider several calculations with piecewise continuous constant surface velocity boundary conditions following Davies (1988) (i.e., the magnitude of the imposed velocities are scaled with the Peclet number of the flow so that the imposed velocities do not force or resist the flow). These results are shown in Figure 3.9. The sides of the box have reflecting boundary conditions, and the box is cooled from above and heated both from below and internally. The Rayleigh number is 10^6, based on heating from below. This provides an initial starting condition with uniform plate velocities for all subsequent calculations. In this calculation there are two plates, one from x=0 to x=1 moving to the right with a 5 cm/yr velocity and the other from x=1 to x=2 which is stationary.

We compare various temperature-dependent rheologies with this geometry and

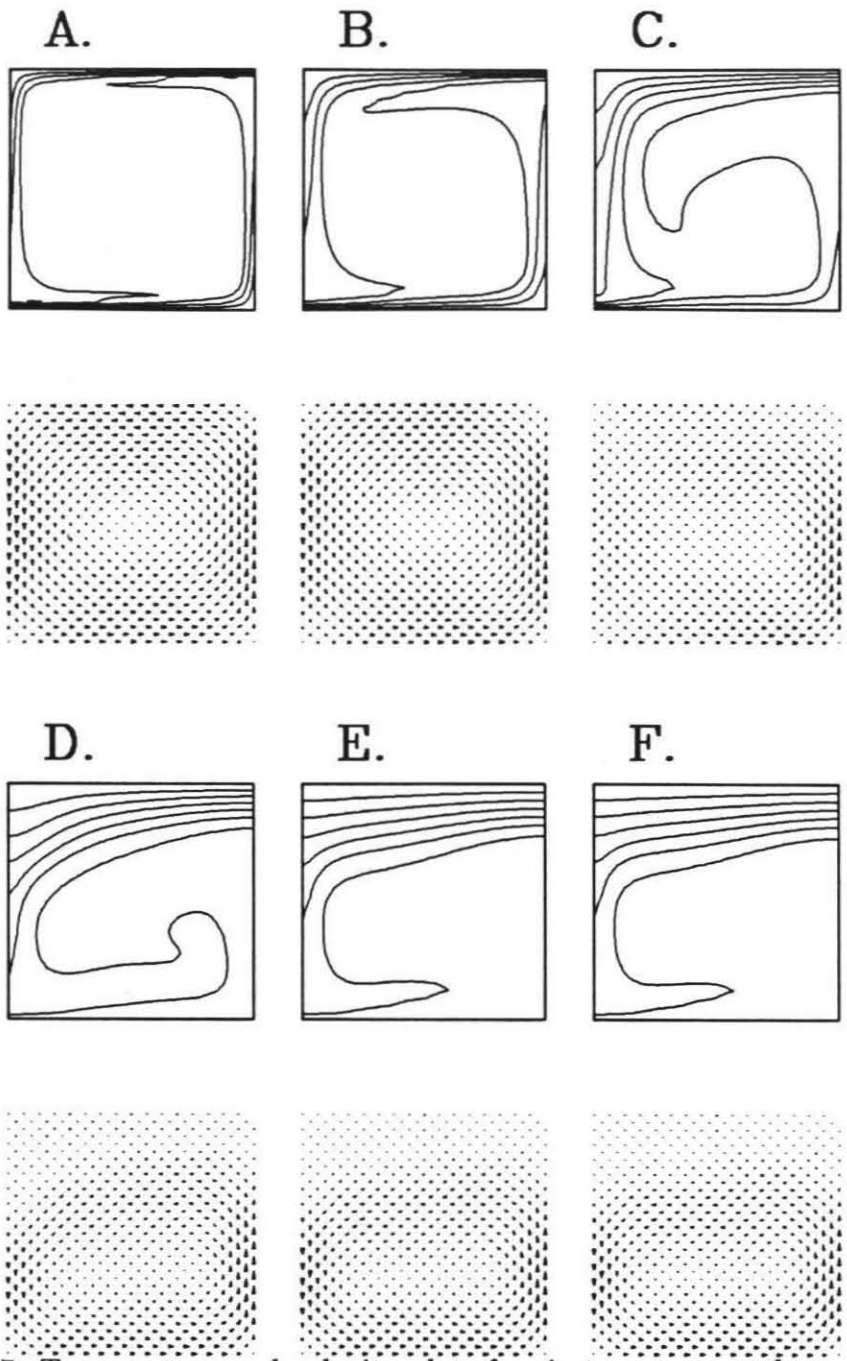

Figure 3.7: Temperature and velocity plots for six temperature-dependent viscosity calculations with a Rayleigh number of 10^6. The temperature dependence follows (2) with $E^* = 6.0$ and $\Delta T = 0.227$. The viscosity cut off is varied in each calculation: a) 10^1, b) 10^2, c) 10^3, d) 10^4, e) 10^5, f) 10^6.

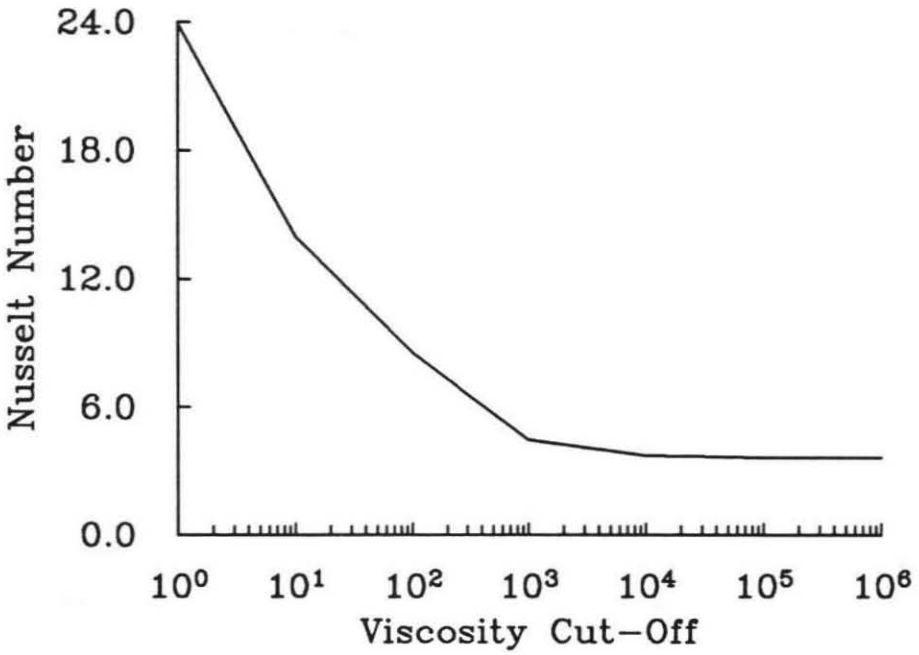

Figure 3.8: The Nusselt number as a function of viscosity cut off for the six steady solutions in Figure 3.7.

A.

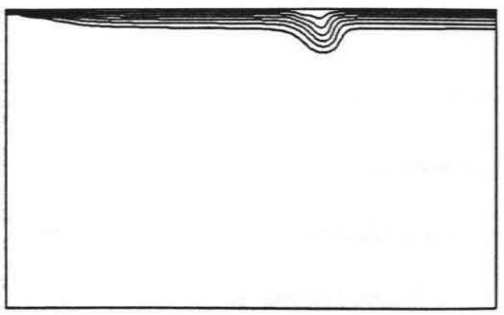

Time Step=40 Time=0.000643

B.

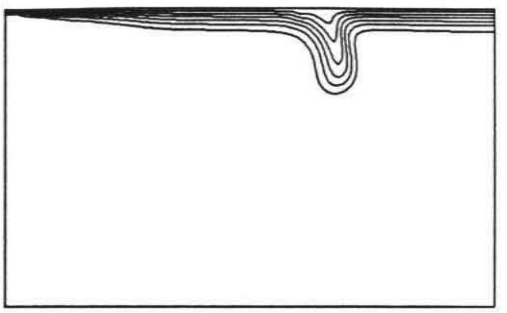

Time Step=80 Time=0.001270

C.

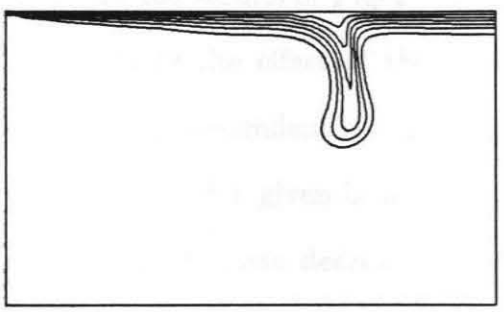

Time Step=120 Time=0.001792

D.

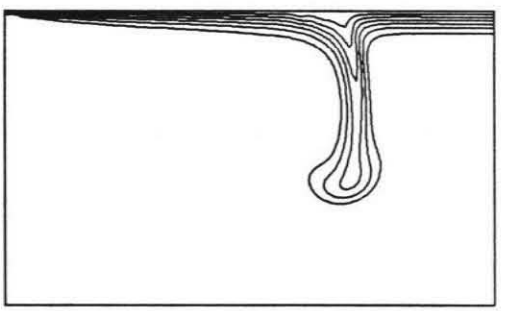

Time Step=160 Time=0.002218

Figure 3.9: Constant viscosity slab model with imposed plate velocities on the left plate (6 cm/yr). The Rayleigh number is 10^6. Time steps and diffusional times are indicated beneath each plot.

the imposed plate velocities and find that unless the total variation in viscosity is less than two orders of magnitude, the plates pile up at the trench and will not deform and subduct. In fact, the calculation in Figure 3.9 is a constant viscosity calculation. This demonstrates that some weakening is needed at the trench, either due to the high stresses or brittle failure, to overcome the strength of the cold lid.

Next we consider several Newtonian temperature-dependent calculations without imposed velocities. Instead of imposing plate velocities, we use the thermal field from Figure 3.9b as the initial condition. These calculations also have reflecting boundary conditions on the side walls and are heated both internally and from below as well as cooled from above with a Rayleigh number of 10^6. (Here the viscosity in the Rayleigh number definition is $\eta(1)$, the interior viscosity.) The viscosity law is cut-off at 10^4 based on the results of Figure 3.7 and 3.8.

To study the effect of the weak zone size on the plate-slab system, we use a temperature-dependent law and beginning with an activation energy of 522 kJ/mole (the olivine value given in Ashby and Verrall, 1977), using Figure 3.9b as an initial condition, we began decreasing the activation energy until a plate-like solution resulted. The attempt is not to model the initiation of subduction, which may be a very complicated function of pre-existing cracks or zones of weakness, but to see if a slab can continue to subduct without being driven by external forces, once it has begun to subduct. We choose the weak zone pre-exponential viscosity to be 10^{-3} (based on the work from Section 3.2) and the weak zone has the same exponential temperature-dependence as the rest of the fluid. The "slab" did not continue to subduct in these calculations, regardless of the weak zone size or viscosity, until the

activation energy was decreased to 104 kJ/mole (one fifth the dry olivine value from Ashby and Verrall). For activation energies higher than this the plate stops and the slab cools by diffusion. For lower activation energies, uniform plate velocities and slab-like downwellings are possible depending on the strength and size of the trench weak zone.

For the remaining calculations we chose an activation energy of 52.2 kJ/mole. Two weak zones are used in these calculations: one at the trench and one at the ridge. We hold the parameterization of the weak zone at the ridge fixed, since we find its effect was confined to the plate near the ridge. (The size of the weak zones is based on numbers of elements). We vary the size of the trench weak zone using depths corresponding to: half the thickness of the thermal boundary layer (TBL), equal thickness of the TBL, and twice the thickness of the TBL. We also vary the width of the trench weak zone, from long and skinny to square. Gurnis and Hager (1988) used a weak zone inclined at 45° but we do not consider any non-rectangular weak zones in our calculations.

Calculations with two end-member weak zones are shown in Figure 3.10. If the trench weak zone is too small (Figure 3.10a) the plate freezes up, like the calculations with no weak zone. If the trench weak zone is too big (Figure 3.10b), the strain-rate beneath the slab is unrealistically high and too much of the boundary layer subducts. The depth of the trench weak zone needs to be about the thickness of the thermal boundary layer and varying the width of the trench weak zone has only a minor effect. Variation of trench weak zone viscosity has a more important role, as was discussed in Section 3.2. Even for the largest trench weak zone, if the pre-exponential

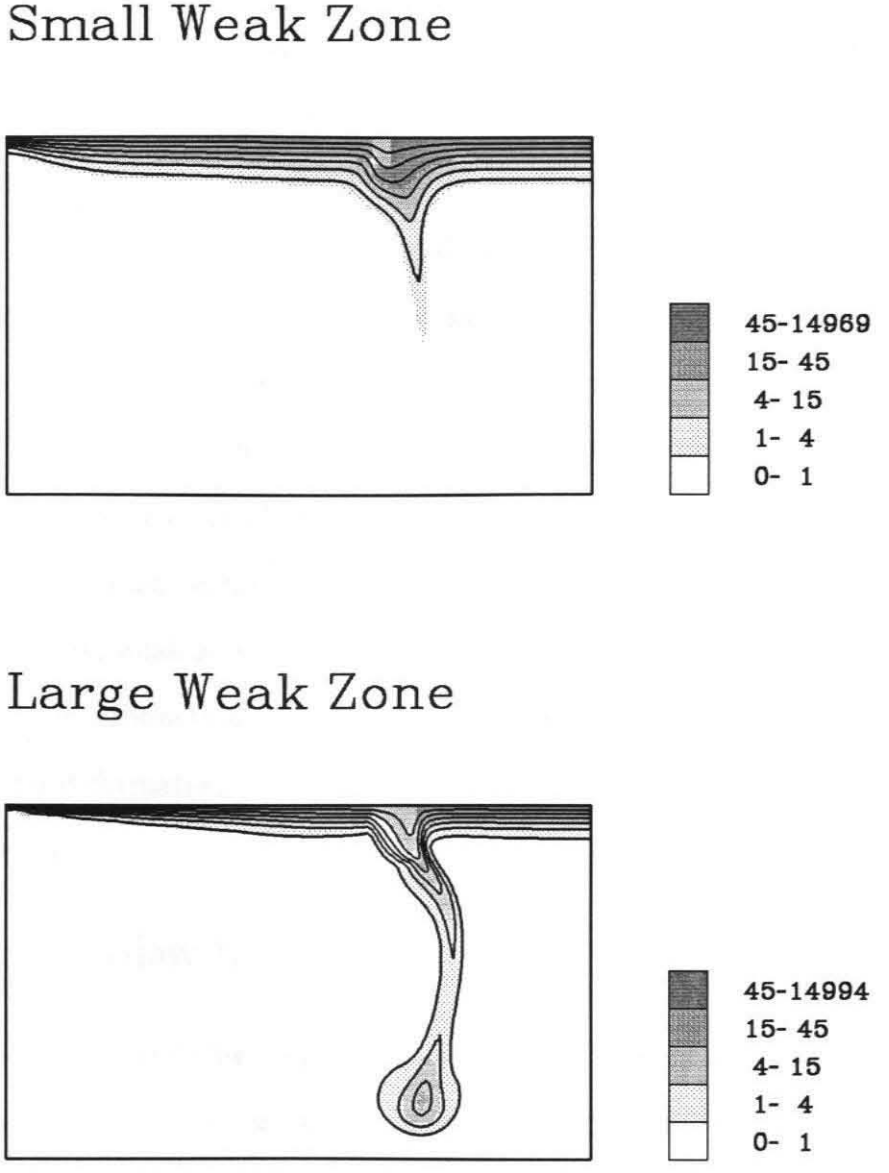

Figure 3.10: A comparison of small and large trench weak zones in Newtonian temperature-dependent calculations using 3.9b as an initial condition. Contours are the 0.14, 0.26, 0.40, 0.54, 0.72 and 0.86 ΔT isotherms and shading represents the viscosity. For both calculations $E^* = 52.0kJ/mole, T_o = 0.277$, Ra= 10^6 and the viscosity cutoff is 10^4. The surface velocities are not imposed.

weak zone viscosity is increased from 10^{-3} to 10^{-2} the plate freezes up.

Surprisingly, a significant factor is the location of the trench weak zone. Figures 3.11 and 3.12 show time-slices for two identical calculations with trench weak zones in slightly different locations relative to the initial slab. In Figure 3.11, the weak zone is at the left side of the initial slab, and in Figure 3.12, the weak zone is in the center of the initial slab. When the weak zone is directly in the middle (Figure 3.12) more of the boundary layer subducts than when the weak zone is on one side or the other (Figure 3.11). The plate velocity in the calculation shown in Figure 3.12 is twice the plate velocity of the calculation shown in Figure 3.11 (see Figure 3.13).

The weak zone calculations presented show that a number of unconstrained parameters (i.e., weak zone size, weak zone viscosity and initial location) can be used to fine tune subduction calculations. This should raise some scepticism since the shape and deformation of the slab can be so radically changed by the choice of these parameters.

3.5 Power-law Rheology

Cserepes (1982) and Christensen (1983) have shown that calculations with non-linear, stress-weakening, temperature-dependent rheology (non-Newtonian) can yield plate-like surface velocities. We also showed in 3.2 that imposing strong plates with non-Newtonian rheology eliminates the need for a weak zone at the trench. We investigate several non-Newtonian temperature-dependent calculations with the same geometry and initial conditions as the Newtonian calculations presented above.

Initial calculations with an activation energy equal to the activation energy of the

A.

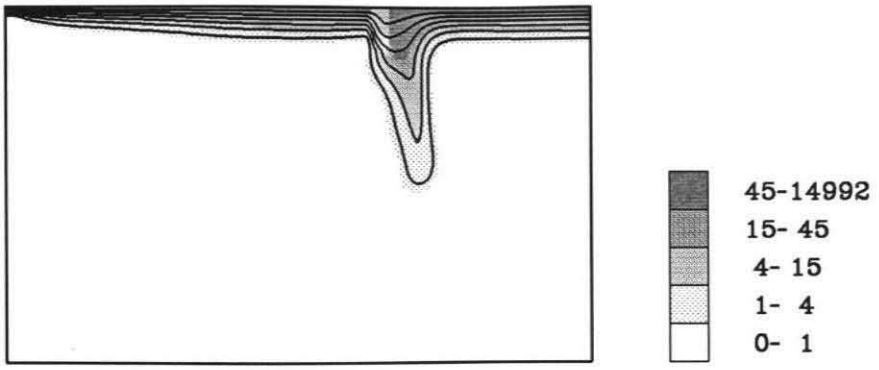

B.

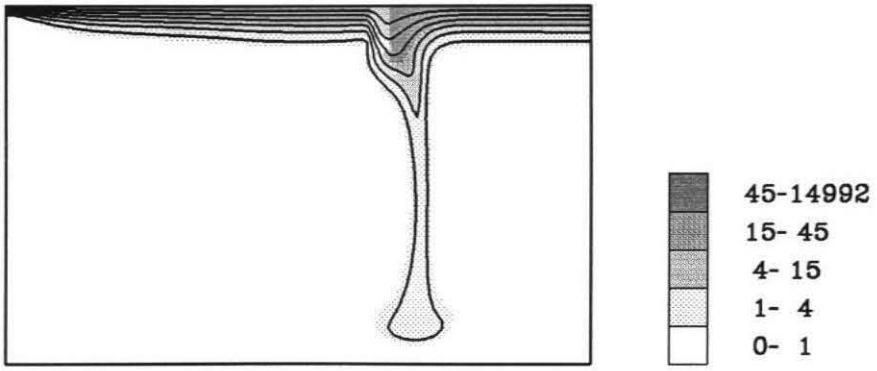

Figure 3.11: Temperature-dependent Newtonian slab calculation using Figure 3.9b as initial condition. Same parameters as 3.10 with a weak zone equal to the thermal boundary layer depth and slightly to the left of the initial slab. A. and B. are from the same calculation with B. being at a later time than A.

A.

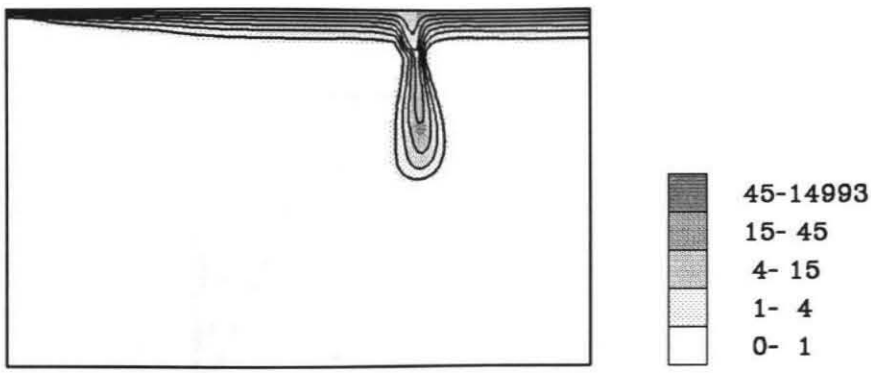

B.

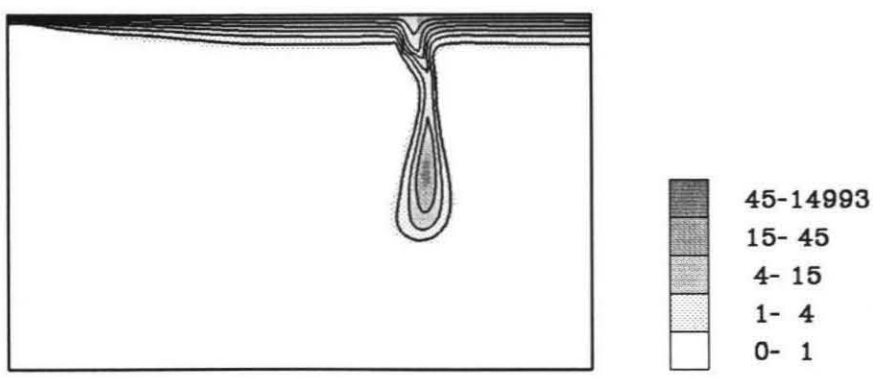

Figure 3.12: Temperature-dependent Newtonian slab calculation using Figure 3.9b as initial condition. Same parameters as 3.10 with a weak zone equal to the thermal boundary layer depth and centered under the initial slab. A. and B. are from the same calculation with B. being at a later time than A.

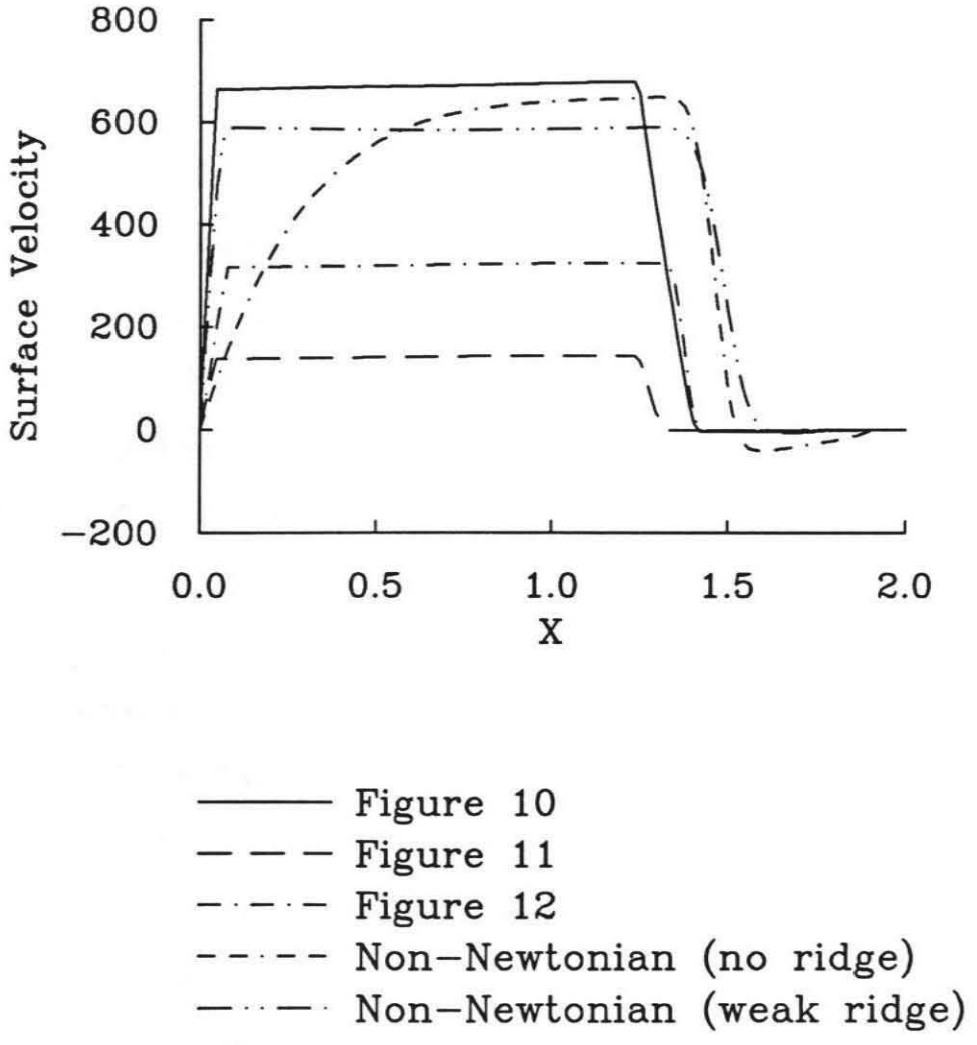

Figure 3.13: Surface velocities for the subduction calculations in 3.10, 3.11 and 3.12 as well as two non-Newtonian calculations

.

Newtonian calculations lead to a slab which drips and pinches off from the boundary layer. The velocity of the descending slab is up to 10 times the plate velocity, and the calculations are very time-dependent.

The strain-rate in these slabs is much too high for these calculations to be realistic models of subduction. Christensen (1983, 1984) showed that Newtonian calculations can simulate non-Newtonian calculations if the Rayleigh number of the non-Newtonian calculation is scaled by the effective viscosity and the activation energy of the Newtonian calculation is decreased by the stress exponent n. To account for this in our non-Newtonian calculations, we progressively increased the activation energy, starting from the value used in the Newtonian calculations. Even when the activation energy is increased five-fold to 275 kJ/mole (half the olivine rheology), the slabs drip away from the boundary. An activation energy equal to or slightly greater than the olivine activation energy was needed to keep the slab from "dripping." A higher activation energy than olivine may be appropriate. Garnet, for example, is harder than olivine (Karato, 1989; Meade and Jeanloz, 1990).

The non-Newtonian calculation shown in Figure 3.14 shows that without a weak zone at the trench, non-Newtonian calculations can produce slab-like, as well as plate-like, solutions. For this calculation the activation energy is 560 kJ/mole and the temperature-dependent cut-off is 10^4. The initial condition is once again Figure 3.9b. The formal Rayleigh number is 5×10^3, but when scaled by the effective viscosity (after Parmentier, Torrence, and Turcotte, 1976) is 10^6. Note that the weakest regions in the trench are at the hinge point of the slab (where bending is the greatest), and along the edge where the subducting plate and the overriding plate

meet (where the shear is greatest). A weak zone at the ridge is still required for uniform plate motion. Without it there is substantial internal deformation in the plate but the slab features are similar (see Figure 3.13 for plate velocities). There are no unrealistic regions of high strain-rate, like in the Newtonian calculations with a big weak zone.

A non-Newtonian rheology provides a self-consistent fluid-dynamical mechanism for subduction, once initiated. It should be noted that these calculations do not address the initiation of subduction, which may shed further light on the mechanism of deformation in trenches. However, it is not a unique solution, since other calculations (such as Newtonian calculations with imposed weak zones) are also capable of generating slab-like features.

3.6 Summary

An effective viscosity decrease in the regions of the ridge and trench is necessary for "plate-like" behavior in temperature-dependent convection calculations. When the viscosity in these regions is reduced to the viscosity of the interior of the flow, the plate and slab approach the maximum velocity of the fluid; raising the trench viscosity leads to large shear tractions at the base of the plate, while lowering the trench viscosity further has little effect on the solution. Using a non-Newtonian rheology, it is possible to simulate plate-like behavior without the use of imposed boundary conditions or weak zones at the trench, although the resulting plate and slab velocities are somewhat different from Newtonian flows with imposed weak zones.

For Newtonian calculations, the value of the weak zone viscosity can significantly

A.

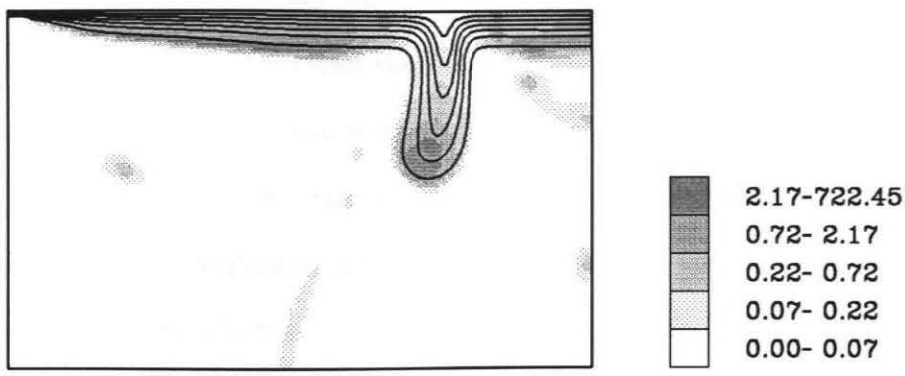

B.

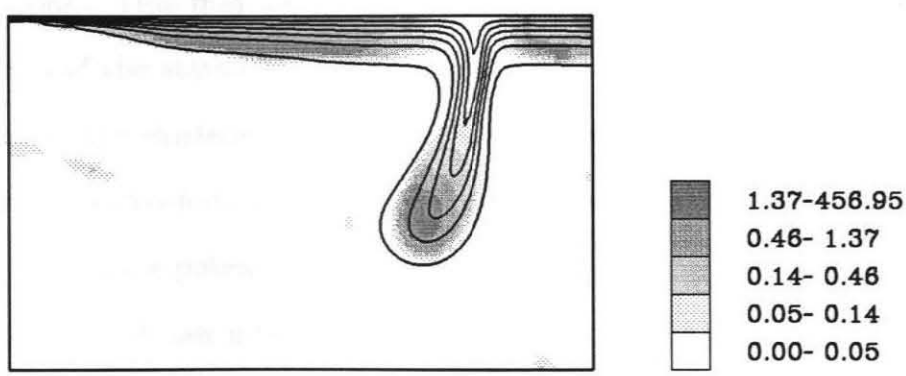

Figure 3.14: A non-Newtonian temperature-dependent calculation using 3.9b as an initial condition. Contours are the 0.14, 0.26, 0.40, 0.54, 0.72 and 0.86 ΔT isotherms and shading represents the effective viscosity. $E^* = 522.0\text{kJ/mole}, T_o = 0.277$, Ra= 10^3 (effective Rayleigh number is 10^6) and the viscosity cutoff is 10^4. The surface velocities are not imposed.

affect the plate velocity. For weak zone viscosities near the viscosity of the interior, varying the viscosity of the weak zone by a factor of ~10 changes the velocity of the plate by a factor of ~3. Only when the weak zone viscosity is much less than that of the interior, are the velocities insensitive to the actual weak zone viscosity used. This makes the choice of weak zone viscosity an important model parameter.

For our non-Newtonian calculations, where the viscosity of the weak zones is determined in a fluid-dynamically self-consistent way, the effective viscosity of the weak zones falls in the transition region for the Newtonian calculations. There, relatively small changes in weak zone viscosity lead to relatively large changes in plate and slab velocities. Plate and slab velocities are ~50% greater in Newtonian calculations with very weak plate boundaries than in the non-Newtonian calculations, and the slab often migrates underneath the stationary plate in the non-Newtonian calculations. This may be a result of the reflecting boundary conditions or the properties of the stationary plate. If plate boundary zones are intrinsically weak, e.g., due to the existence of through-going faults, the results of strictly fluid, non-Newtonian calculations, where the weakening of plate boundaries is due only to stress concentration, are potentially misleading.

A constitutive law much weaker than the dry olivine diffusional flow mechanism of Ashby and Verrall (1977, i.e., Newtonian, temperature- and pressure-dependent viscosity) is needed in the vicinity of the trench, regardless of the size or weakness of the weak zone. This would be possible if the effect of water on the activation energy is more important than it is currently thought or if another deformation mechanism is more important than diffusional flow (e.g., power-law flow, plasticity or brittle

failure).

Christensen (1983, 1984) shows that Newtonian rheologies can closely approximate non-Newtonian rheologies if the activation energy and volume in the Newtonian rheologies is decreased by the power-law exponent (and the average effective viscosity is used in the Rayleigh number). This could explain a decrease by a factor of 3 to 5 in the activation energy (assuming a power-law deformation mechanism). We find that a factor of 10 is more appropriate for scaling our calculations, and we need a weak zone in the Newtonian calculations as well. Christensen's conclusions were based on unit aspect ratio calculations with a more uniform change in viscosity with temperature. The simple scaling Christensen presents has also been shown to break down in time-dependent calculations (Christensen and Yuen, 1989).

Chapter 4

Subduction and the Geoid

The subduction of oceanic lithosphere is the most direct and compelling evidence for mantle convection. As we showed in Chapter 1, the depth to which the lithosphere subducts is also one of the most controversial issues in solid earth geophysics. Until recently, the most direct evidence of slabs has been the depth, dip, and shape of the Benioff zone (e.g., Isacks and Molnar, 1971; Richter, 1979; Giardini and Woodhouse, 1984; Vassiliou, 1984) and the travel-time residuals from deep earthquakes within the slab (Jordan, 1977; Creager and Jordan 1984, 1986; Fischer, Creager and Jordan, 1990). Recent three-dimensional seismic tomographic inversions (Zhou and Clayton, 1990) have attempted to resolve slabs in the western Pacific. While the agreement between the fast anomalies, interpreted as cold slabs, and the dip of Benioff zones is good in the mid-upper mantle, the results are somewhat ambiguous in regard to the fate of slabs near the 670. This could be due to: the resolution of the inversions, the noise in the ISC data in the 500 to 900 kilometer depth range (Gudmundsson, Davies and Clayton, 1990), or the inhomogeneous sampling due to the locations of

the sources and receivers, as well as any combination of these. As we will show, the maximum stresses and the thermal anomaly may not coincide near a deformed chemical boundary. Also, even a well resolved image is not always straight-forward to interpret, especially in a complicated situation where a highly deformed chemical boundary is present.

The fate of subducting slabs has been studied both numerically (Christensen and Yuen, 1984; Gurnis and Hager, 1988) and with tank experiments (Kincaid and Olson, 1987). These results were discussed in Chapter 1 as part of the overall review of convection and subduction; previous studies were concerned with the deformation of the slab and the ability of the slab to cross a viscous or a chemical boundary. No numerical study has attempted to investigate both density and viscosity discontinuities. We calculate both geoid and topography for temperature-dependent convection calculations with slab-like downwellings. We compare geoid and topography for slabs interacting with chemical and viscosity boundaries to determine what effects these boundaries have on the observed geoid.

The geoid is an equipotential surface of the Earth's gravity field. Geoid anomalies, differences between the observed geoid and a model elipsoidal geoid, are a result of lateral density variations within the Earth. Variations in density arise from temperature variations and topography on: the surface, the core mantle boundary, and any internal density contrasts (such as phase changes or compositional changes). Therefore, although the geoid alone does not uniquely determine the interior density structure, it provides a means of testing the calculations. This test is very important, since we are only now beginning to resolve fuzzy pictures of slabs, through

seismic tomography, and much of our knowledge about slabs comes from indirect observations.

In the mantle, the largest lateral variations in temperature are likely to be associated with subducted slabs. Therefore, subduction zones should have a major signature in the geoid. In fact, numerous studies show gravity or geoid highs in subduction regions (Kaula, 1972; Kogan, 1975; McAdoo, 1981; Jones, 1983; Rabimowicz *et al.*, 1984). Most of the power in the long wavelength, spherical harmonic degree l = 2-3, component of the geoid can be modeled by density anomalies inferred from seismic tomography (Hager and Richards, 1984; Hager *et al.*, 1985). Removing this signal from the geoid leaves a residual geoid high which is well correlated with subduction zones, up to spherical harmonic degree 9 (Hager, 1984). This strong signal in the geoid has been used to constrain mantle rheology (e.g., Hager, 1984; Ricard *et al.*, 1984; Richards and Hager, 1984; Hager and Richards; 1989). However, geoid anomalies over subduction zones also provide powerful constraints for testing dynamic and seismic models.

4.1 Slabs and the Deformation of a Chemical Boundary

The controlling factor in slab-density boundary interactions is the ratio of the density contrast across the boundary to the density contrast in the slab. Kincade and Olson (1987) define a factor

$$R = \frac{\rho_{slab} - \rho_{lower\ mantle}}{\rho_{slab} - \rho_{upper\ mantle}} = \frac{\alpha\Delta T/2 - \Delta\rho/\rho}{\alpha\Delta T/2} = \frac{\mathrm{Ra}/2 - \mathrm{Rb}}{\mathrm{Ra}/2} \tag{4.1}$$

which is the ratio of chemical buoyancy to thermal buoyancy, where α is the coefficient of thermal expansion, ΔT is the temperature contrast across the box, Ra is

the thermal Rayleigh number and Rb is the chemical "Rayleigh number"

$$Ra = \frac{\rho g \alpha \Delta T d^3}{\kappa \nu} \tag{4.2}$$

$$Rb = \frac{\Delta \rho g d^3}{\kappa \nu} \tag{4.3}$$

$\Delta\rho$ is the density contrast across the chemical boundary, g is the acceleration of gravity, d is the depth of the box, κ is the thermal diffusivity and ν is the viscosity. Note that in the scaling, we assume that the temperature difference across the slab is $\Delta T/2$, where ΔT is the temperature difference across the box (see Figure 4.1).

In the numerical calculations, Ra and Rb are input parameters. Translating to a density contrast $\Delta\rho$ for the chemical boundary requires accurate values for α and ΔT. Estimates of α for upper mantle minerals range from 2.0×10^{-5} to 5.0×10^{-5} (Duffy and Anderson, 1989). Also, α decreases by a factor of two over the pressure range in the upper mantle (Chopelas and Boehler, 1989), and α increases by a factor of two over the temperature range of the mantle (Suzuki, 1975). The slab may also not be the same composition as the surrounding mantle, and it has been proposed that due to the effects of phase changes on the appropriate slab mineralogies, the effective α for slabs may be as much as five times the value of α for the rest of the mantle (Anderson, 1987). We will present both R, and a percent density based on our scaling choices of $\alpha = 3.0 \times 10^{-5}$ and $\Delta T = 1200°\mathrm{C}$.

Figure 4.1 shows a temperature-dependent Newtonian slab calculation with a chemical boundary. The sides, top, and bottom of the box are free slip, and the fluid is internally heated and cooled from above. The boundary is tracked with a chain of markers (the implementation is described in Appendix C); the fluid below the marker chain (denoted by a black line) is more dense than the fluid above the

chain. A weak zone in the boundary layer is used to maintain subduction, and a small perturbation in the boundary layer, under the weak zone, is used as an initial condition. For Figure 4.1, $R = -1.0$, which corresponds to a 3.6% chemical density change if α is assumed to be 3×10^{-5} and $\Delta T = 1200°\mathrm{C}$.

In Figure 4.1, the slab deforms the boundary by several hundred kilometers directly beneath the slab; an amount which should be seismically detectable. In this calculation, the stresses in the slab are downdip extension in the mid-mantle region and downdip compression deep region (Figure 4.2), consistent with seismic observations (e.g., Richter, 1979; Vassiliou, 1984). Note that while the tip of the slab, which is a thermal feature (denoted by the contours), bends at the boundary, the maximum stresses (Figure 4.2) do not follow the thermal feature near the boundary. This shows that the seismic portion of the slab, defined by the locations of deep earthquakes, may behave differently from the thermal slab anomaly in the vicinity of a density discontinuity.

Some seismic observations of travel time residuals are best modeled by slab thickening at 670 kilometers (Giardini and Woodhouse, 1984; Vidale, 1987; Fischer and Jordan, 1990). Fischer and Jordan (1990) note that their observations of 50% to 200% thickening of the Tonga slab are consistent with Gurnis and Hager's (1988) calculations of slab subduction in a fluid with a viscous boundary. However, Creager and Jordan (1984, 1986) model deep slabs beneath Mariana and other Northwest Pacific arcs with no slab thickening. The slab in Figure 4.1 is consistent with the seismic observations of slab thickening; the deformation of the interface, about 150 kilometers, is nearly consistent with the 900 kilometer slab depth inferred by Fischer,

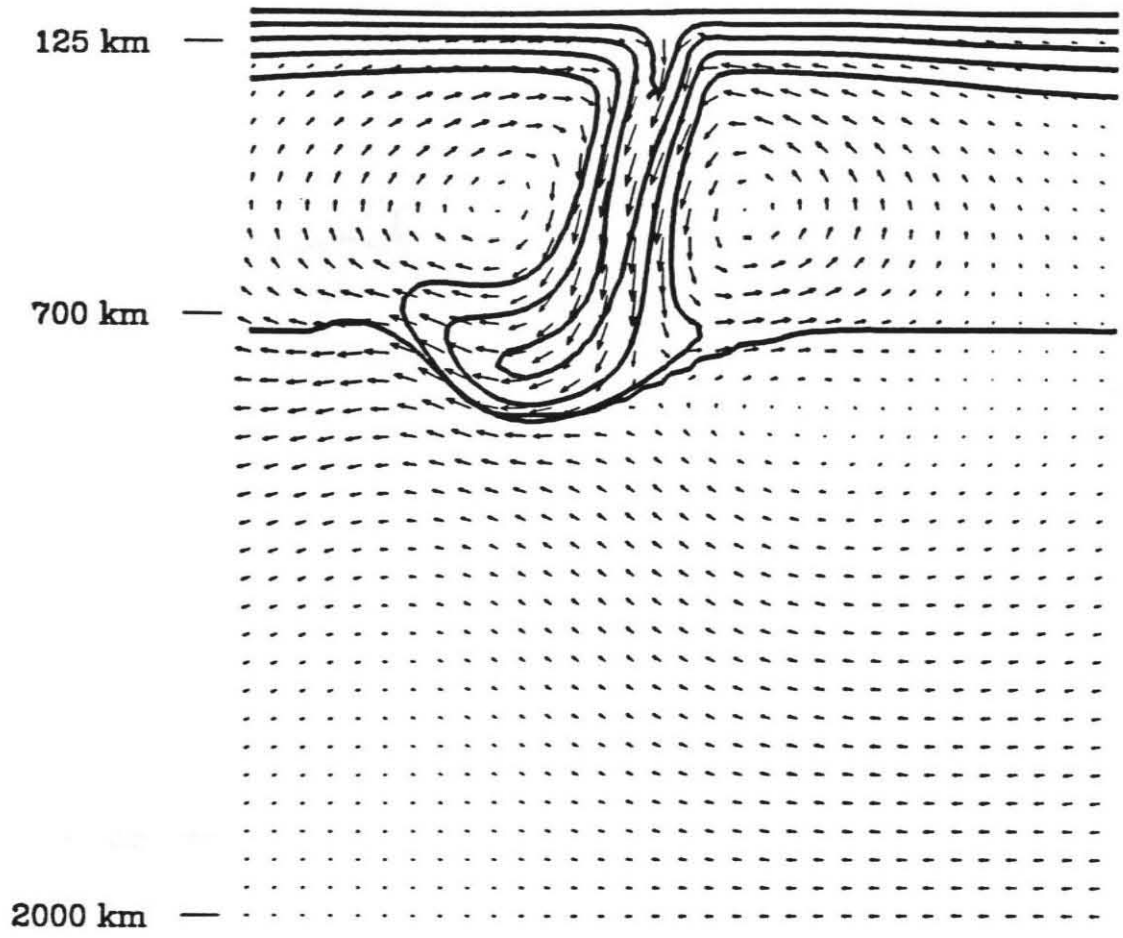

Figure 4.1: A temperature-dependent convection calculation representing a slab interacting with a chemical boundary (the lower layer is 3.6% denser than the upper layer; $R = -1.0$). The contours are evenly spaced isotherms with an interval of 0.20 dimensionless temperature units (about 250 °C). The heavy black line is the chemical boundary. Only part of the computational domain is shown.

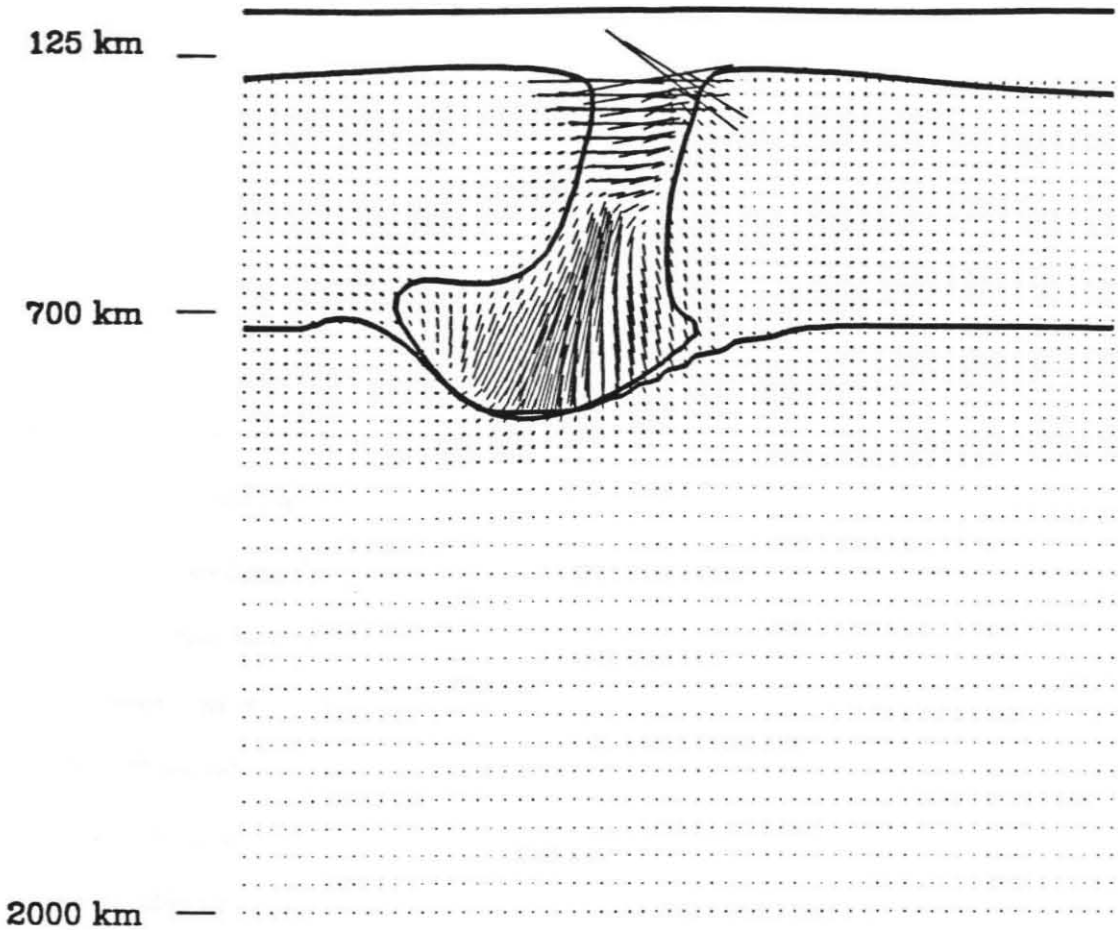

Figure 4.2: The axes of principal compressive stress for the calculation in Figure 4.1. The 0.8 isotherm (1000 °C) is shown to denote the slab. The magnitude of the stress is proportional to length of the line representing the axes.

Creager and Jordan (1990).

Table 4.1 shows the relationship between the deformation of the boundary and R for constant viscosity calculations. For small density discontinuities ($R > 0$), the slab continues subducting all the way to the core mantle boundary. For density discontinuities comparable to the density of the slab ($0 > R > -1$), the slab deforms the boundary, possibly by several hundred kilometers, but remains in the upper layer and the amount of boundary deformation is time-dependent. For density discontinuities greater than the slab ($R < -1$), the slab remains in the upper layer with little or no detectable deformation of the boundary. These results are consistent with other slab studies (Hager and Raefsky, 1981; Christensen and Yuen, 1984; Kincade and Olson, 1987). However, we find that a bigger density discontinuity is needed to resist slab penetration than either Kincade and Olson or Christensen and Yuen; this is most likely because our are slabs are stronger. However, because of the uncertainty in α for upper mantle mineralogies, dynamical studies cannot place a tight constraint on the density discontinuity across the "670."

In all these results, a temperature-dependent Newtonian rheology was used; the activation energy was considerably smaller than the activation energy of olivine. The rheology was chosen to give slab-like features with a Newtonian rheology with a weak zone parameterization, similar to the method discussed in Chapter 3. The use of even stronger, possibly more realistic, rheologies increases the amount of deformation for a given choice of Ra and Rb.

Model	$\frac{\Delta\rho_c}{\rho}$	Rb	R	Boundary Deformation
CH4.1	1.2%	1×10^6	0.33	large
CH4.2	2.4%	2×10^6	-0.33	limited
CH4.3	3.6%	3×10^6	-1.00	very limited
CH4.4	6.0%	5×10^6	-1.66	no

Table 4.1: Results from chemically layered temperature-dependent convection calculations. "Large" deformation means the slab continues to sink to the core mantle boundary and the boundary does not stop it, "limited" deformation means that a small but significant amount of deformation occurs (of order 300 km) and then the slab may return to the upper mantle and "no" deformation means the deformation is less than 50 kilometers (deformations smaller than this cannot be resolved from our calculations). The thermal Rayleigh number for all cases is 3×10^6.

4.2 Geoid and Topography for Subduction Calculations

The geoid anomaly over subduction zones is a powerful constraint on slab dynamics. Figure 4.3 shows geoid profiles across several trenches. Hager (1984), using slab densities based on the location of Benioff zones, showed that with a 30-fold viscosity increase in the lower mantle, the slab density could explain the long wavelength (degree 4-9) geoid anomaly around subduction zones. Hager also noted that a chemical boundary with a viscosity increase was consistent with the geoid but required that approximately 300 kilometers of subducted slab remained trapped at the base of the upper mantle beneath the subduction zone or that the density contrast associated with slabs is much larger than he estimated. The reasons for these conclusions can best be understood by examining the geoid kernels. Richards and Hager (1984) and Hager *et al.* (1985) presented the geoid kernels for a chemically stratified mantle, a viscously stratified mantle, and a chemically and viscously stratified mantle. The viscosity models which have kernels with a positive sign in the upper mantle are the kernels with a viscosity discontinuity at 670 kilometers (either with or without a density discontinuity). These models lead to a positive geoid with density anomalies from slabs confined primarily to the upper mantle. The applicability of Richards and Hager's results to the Earth depend on two critical assumptions. First, the kernels from Richards and Hager (1984) and Hager *et al.* (1985) are for a uniform viscosity fluid with no lateral viscosity variations; the effects of the rheology of the slab on the long wavelength geoid are unknown. Second, the chemically stratified kernels assume that the amount of boundary deformation can be modeled by calculating the deformation from the stresses on an undeformable boundary. Both of these assumptions

can now be tested.

4.2.1 Constant Viscosity Calculations

First, we examine a series of constant viscosity calculations with driven velocity boundary conditions. We follow the approach of Davies (1988) by driving the plates with a velocity consistent with the free convection velocity, but with uniform velocity across the surface to simulate plate behavior. Using these simple calculations eliminates the effect of the trench parameterization, which we will show has an effect on the short wavelength topography, and hence geoid. We note that topography provides a potential constraint on the viscosity of the weak zone, which, as we showed in Chapter 3, has an important affect on the solution and is otherwise unconstrained. The constant viscosity slabs allow us to compare our new method with the Richards and Hager (1984) results. In Appendix C, we outline the method we use for calculating the topography and geoid from our temperature and velocity fields. We can also address the effect of the deformation of a chemical boundary for constant viscosity slabs, and test the assumption made by Richards and Hager that an impenetrable boundary is a close approximation to the deformable density discontinuity with small deformation.

Figure 4.4 is the temperature field from a constant viscosity convection calculation in a 2 by 1 box with reflecting sidewalls. The box is heated from below, cooled from above, and uniform velocities are imposed on the top from $x = 0.1$ to $x = 0.9$ (plate 1) and a uniform zero velocity is imposed from $x = 1.0$ to $x = 2.0$ (plate 2). The velocities are tapered linearly from x=0.0 to x=0.1 and x = 0.9 to x=1.0 to smooth the large stress singularity which would result from a step discontinuity

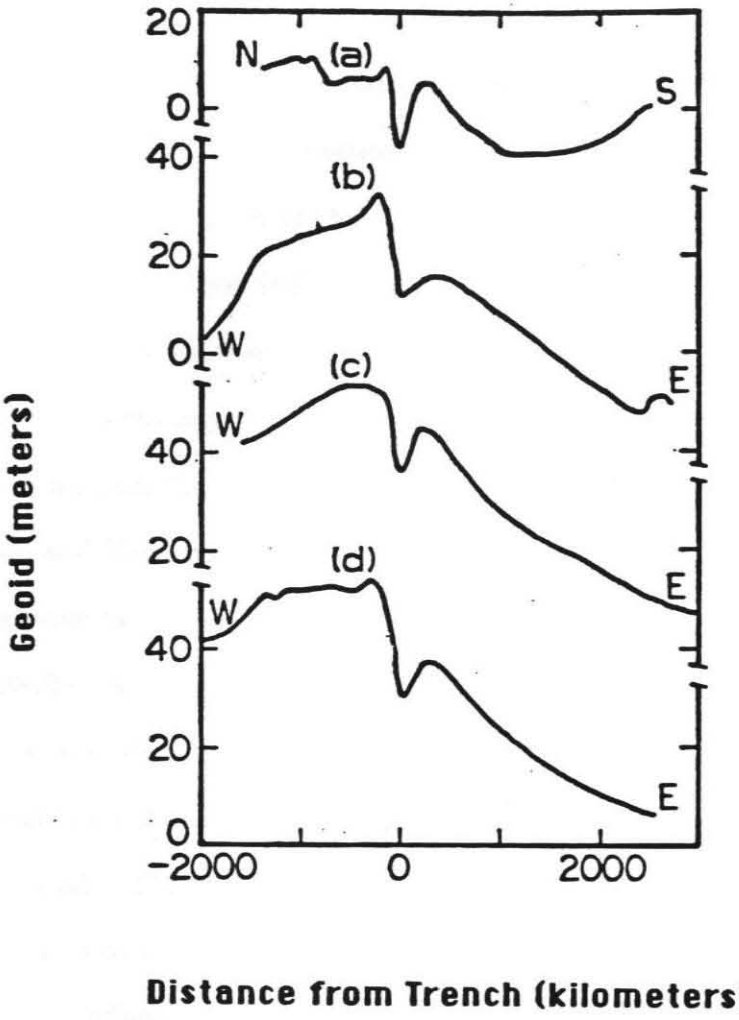

Figure 4.3: Geoid profiles across several trenches: (a) Aleutians, 175°; (b) Japan, 40°N; (c) Marianas, 20°N; Kermadec, 30°S. (after Davies, 1981).

in the velocity. This gives two plates of equal size, one on the left side of the box moving to the right, and the other on the right side of the box which is stationary. The Rayleigh number in the calculations is 10^6 and the chemical Rayleigh number is 5.0×10^5, ($R = 0.0$). A compositionally dense layer is initially at a uniform depth of $0.5d$, where d is the depth of the box.

The compositional layer is followed by tracking a chain of passive markers which defines the boundary between the two densities. Additional markers are added when the distance between any two markers becomes too large and markers are removed when they bunch up (for numerical tractability). A similar method was described by Christensen and Yuen (1984). There is less chemical diffusion with this method than in our implementation of a double-diffusive method described by Hansen and Yuen (1989a; 1989b). We compared several numerical methods for tracking a deformable boundary; a brief description of the methods can be found in Appendix C.

Our double-diffusive method becomes unstable for Lewis numbers greater than several hundred. (The Lewis number is the ratio of thermal to chemical diffusion). While it is not possible to quantify the Lewis number for our marker chain method, the amount of diffusion is significantly less than the double-diffusive method with a Lewis number of 200. For comparison to the Earth, if the density discontinuity at 670 kilometers is the result of an increase in iron content, and if molecular diffusion of iron is the dominant mechanism for chemical diffusion, then a Lewis number of at least 10^{10} is appropriate for the 670. Hansen and Yuen (1989b) provide a more detailed treatment of double-diffusive convection.

Gurnis and Hager (1988) showed that a temperature-dependent viscosity slab

with periodic boundary conditions leads to asymmertic subduction with a slab dipping shallower than 90°. The periodic boundary conditions allow the trench to move relative to the direction of flow. In the calculations which follow, periodic boundary conditions are not used for computational reasons, but we do not expect the steep dip of the slab to have a serious effect on our results.

The Frontispiece shows the same calculation as depicted in Figure 4.4. The top left image is the temperature field – red representing hot and blue representing cold material. The black line across the image marks the density discontinuity. The resulting density field is shown on the top right – red being less dense than average and blue being more dense than average. The composition field is generated by adding the thermal and compositional density, and then removing the horizontal average from each layer. The red region below the slab in the density field shows that as the slab descends into the region initially occupied by the denser fluid, a negative, not positive, density anomaly results because the slab has locally replaced denser material. This is a transient feature; as the slab continues to subduct, it flows laterally and settles along the boundary. Because of the uniform viscosity, the topography of the boundary is not maintained for long in these calculations. Geoid highs never result, regardless of the size of the density increase across the boundary or the amount of cold material subducted.

The image on the top right of the Frontispiece is processed similarly to a tomographic image (i.e., thermal and compositional density are lumped together, the horizontal average is removed from each layer, and differences relative to the average at that layer are plotted). However, we plot density perturbations, not velocity

perturbations, so this is not seismic tomographic image. To reduce a seismic tomographic image to a density image, like the ones on the Frontispiece, requires mapping the velocity anomalies to thermal and chemical anomalies. Since the upper mantle is not chemically homogeneous, this step is not unique. For example, comparing the density image on the right to the image on the left, it is clear that after removing the average with depth, separating the thermal and compositional density contributions is not straightforward. This demonstrates how difficult it can be to interpret density differences from seismic velocities in tomographic images. In seismic tomography, a one-dimensional model is removed (i.e., PREM), since the horizontal average is not known; it is not clear to what extent the differences between the one-dimensional model and the actual horizontal average enhance or hinder the interpretation of features in a tomographic image.

A slab with a factor of 100 increase in viscosity at $0.5d$ (see also Figure 4.8) is shown in the lower left of the Frontispiece and a density difference image is shown on the lower right. (The color scales are the same as the ones from the top images). The viscosity discontinuity is more straightforward to interpret: in this case all the slab anomaly contributes as a positive density anomaly.

Since there are several sources of density variations which contribute to the geoid, it is instructive to examine the contributions to the geoid individually. Figure 4.5 (top) shows the surface topography and the geoid for the temperature and composition fields shown in Figure 4.4. Figure 4.5 (bottom) shows the individual terms which contribute to the geoid: the surface topography contribution, the contribution from the temperature field, and the deformation of the chemical boundary. The core

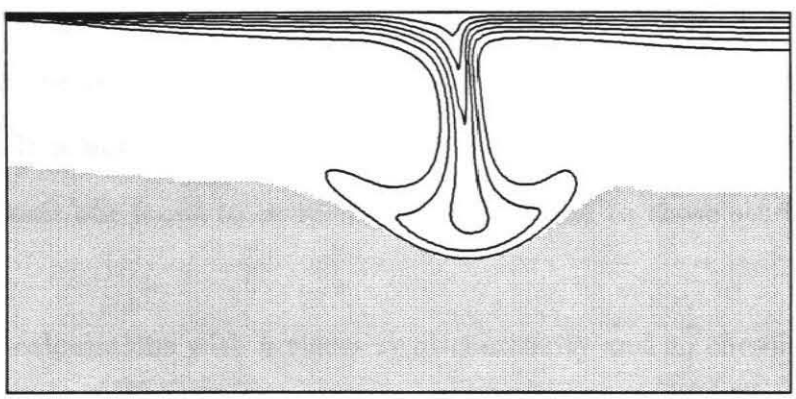

Figure 4.4: The temperature (line contours) and composition field (shaded region) for a constant viscosity slab with a 2% density increase ($R = 0.0$) initially at $0.5d$.

mantle boundary topography is small and only the longest wavelengths contribute due to the e^{-kd} factor (see Appendix C). From Figure 4.5 (bottom), it is clear that the positive thermal contribution to the geoid is overwhelmed by the topography at short wavelengths near the trench. This is true of all the models we examined, both viscously and chemically stratified.

In Figure 4.6, only the long wavelength components of the geoid are plotted, for comparison with Richards and Hager (1984). Richards and Hager (1984) use up to spherical harmonic degree 9, which has approximately a 4,000 kilometer wavelength. For the Cartesian slab calculations, using a box depth of 1,500 kilometers (twice the upper mantle) for our scaling length, the degree 2 wavelength is about 3,000 kilometers. In subsequent figures, the "long wavelength" component of the geoid calculations is the degree 1 and 2 components, for comparison with Richards and Hager. It is not clear how the trench parametrization affects the higher harmonics, so we limit our focus to wavelengths comparable to those studied by Richards and Hager.

For calculations with a viscosity discontinuity and no chemical boundary, the results are somewhat different. We assume that the viscosity discontinuity is a result of a strongly pressure-dependent phase change, and we do not allow the boundary of the viscosity discontinuity to deform. As the slab descends across the viscous boundary, it thickens due to the decreased slab velocity (Figure 4.7). This is consistent with the findings of Gurnis and Hager (1988) for temperature-dependent slabs. There is a noticeable difference in the geoid for the slab impinging on a viscosity discontinuity (Figure 4.8). While directly over the slab the geoid is low, due to the

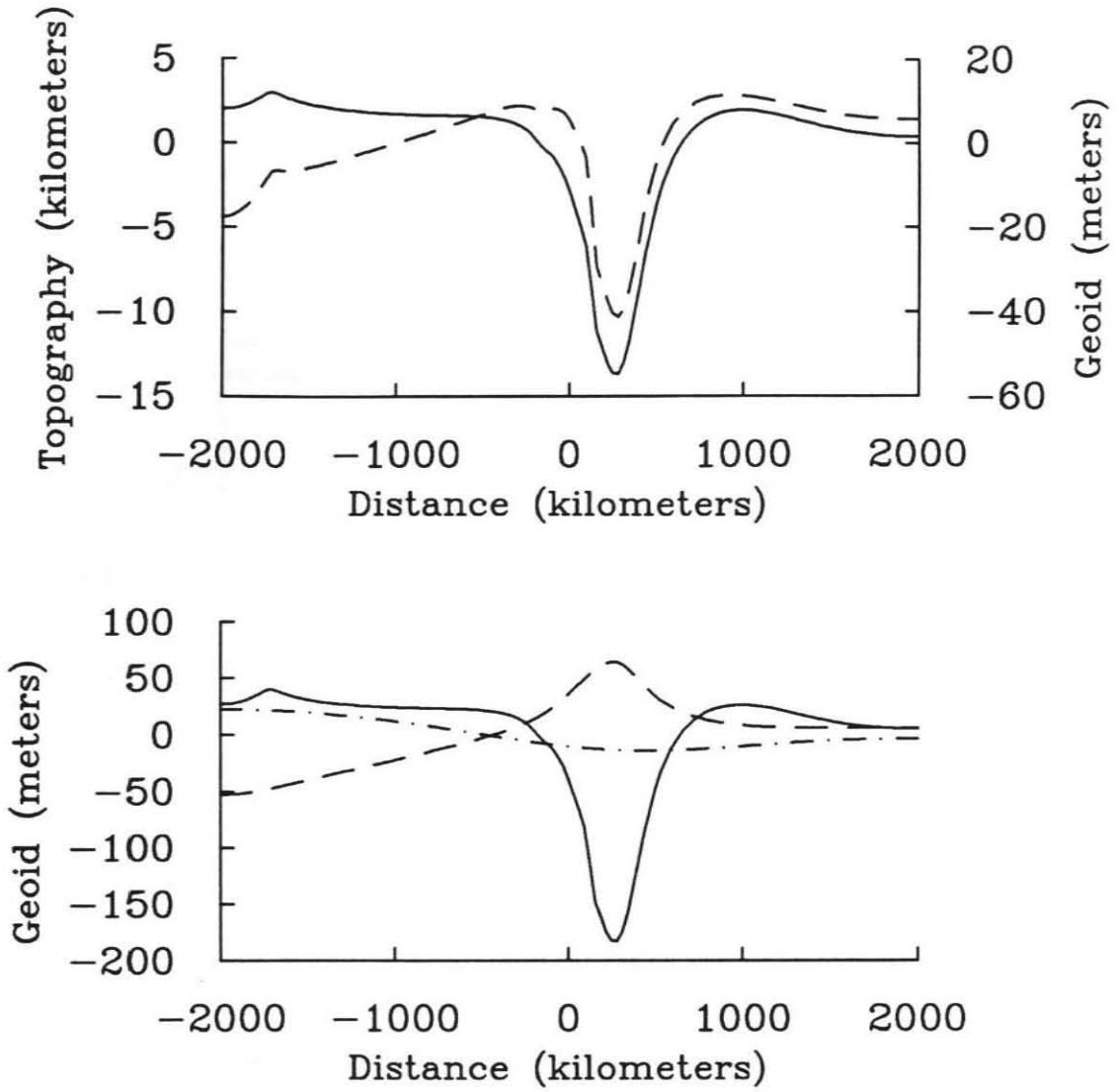

Figure 4.5: (top) The geoid (dashed line) and topography (solid line) for the calculation shown in Figure 4.4. (bottom) The individual components of the geoid: surface topography (solid line), thermal density anomaly (dashed line), and deformation of the chemical boundary (dot-dashed line).

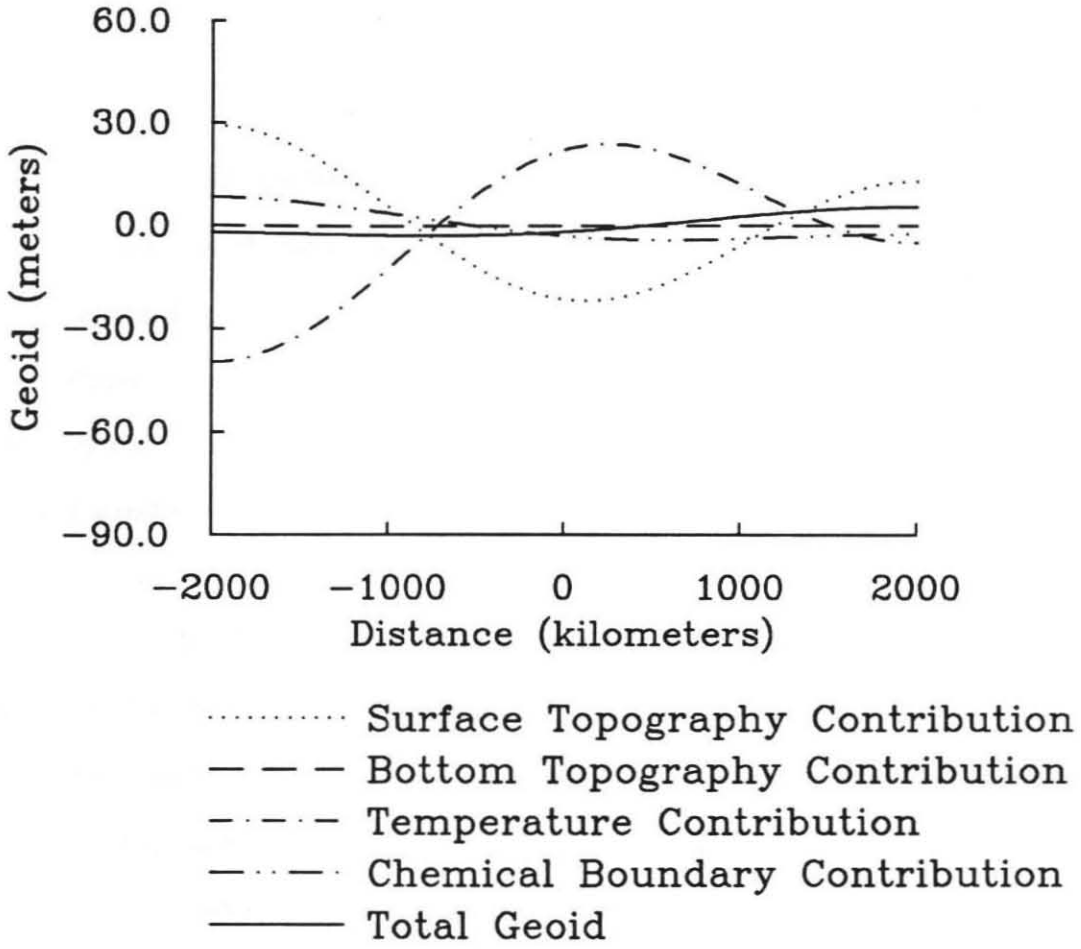

Figure 4.6: The long wavelength geoid and topography for the calculation shown Figure 4.4.

short wavelength component of the topography, the long wavelength geoid is slightly high over the subduction zone (Figure 4.9). This is not a pronounced high, as in the Earth's geoid, but the magnitude of the high can be adjusted by changing the density of the slab, through changing α for example. Also, the magnitude for the geoid will be affected by the depth of the discontinuity. For numerical tractability our discontinuity is at one half the depth of the box, while a depth of one quarter is more appropriate for the 670 kilometer discontinuity. The important feature is that the geoid is positive, unlike the geoid for a chemical boundary only (Figure 4.6).

An example of a 2% density discontinuity and a factor of 100 increase in viscosity is shown in Figure 4.10. The density discontinuity is allowed to deform, but the viscosity discontinuity is not. In this case, the long wavelength geoid is once again positive, but the effect of deforming the boundary acts to decrease the geoid high (Figures 4.11, 4.12). This result agrees with Hager *et al.* (1985), and it is easy to see how the effect of increasing the boundary deformation decreases the geoid (note that the chemical boundary contribution is negative over the trench). For the cases where there is a large deformation of the boundary, i.e., R is positive, the increased amount of thermal slab anomaly cannot offset the chemical contribution to the geoid. For these cases the layered mantle kernels from Richards and Hager (1984) no longer apply, and geoid lows can result even with a viscosity increase if the amount of boundary deformation is large.

To further examine the effect of the density discontinuity on the geoid, we present several calculations with various density discontinuities across the boundary in Figure 4.13. (The temperature and composition fields for these calculations can be

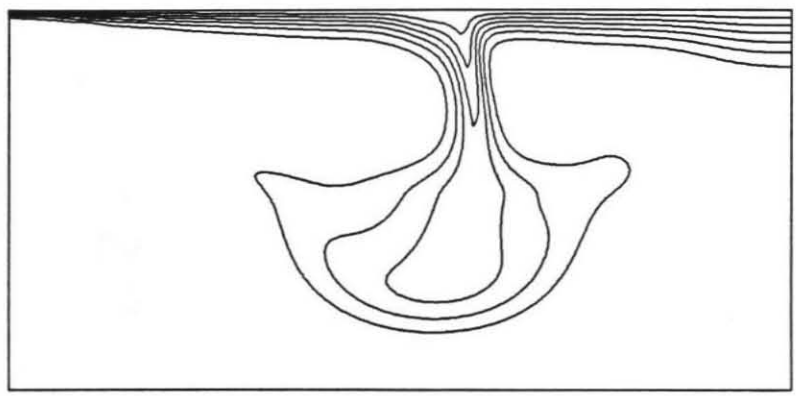

Figure 4.7: The temperature (line contours) for a constant viscosity slab with a factor of 100 increase in viscosity at $0.5d$.

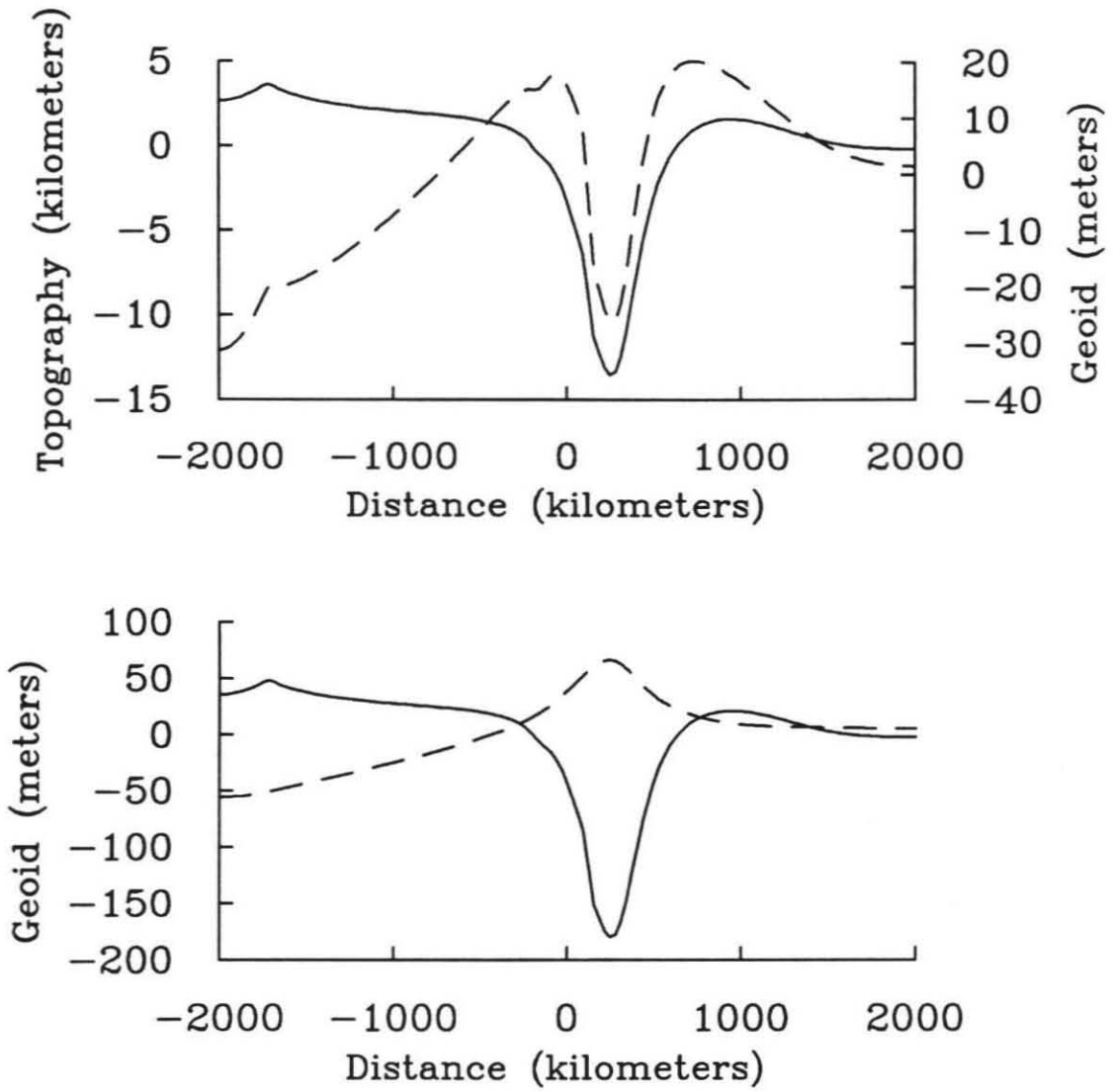

Figure 4.8: (top) The geoid (dashed line) and topography (solid line) for Figure 4.7. (bottom) The individual components of the geoid: surface topography (solid line) and thermal density anomaly.

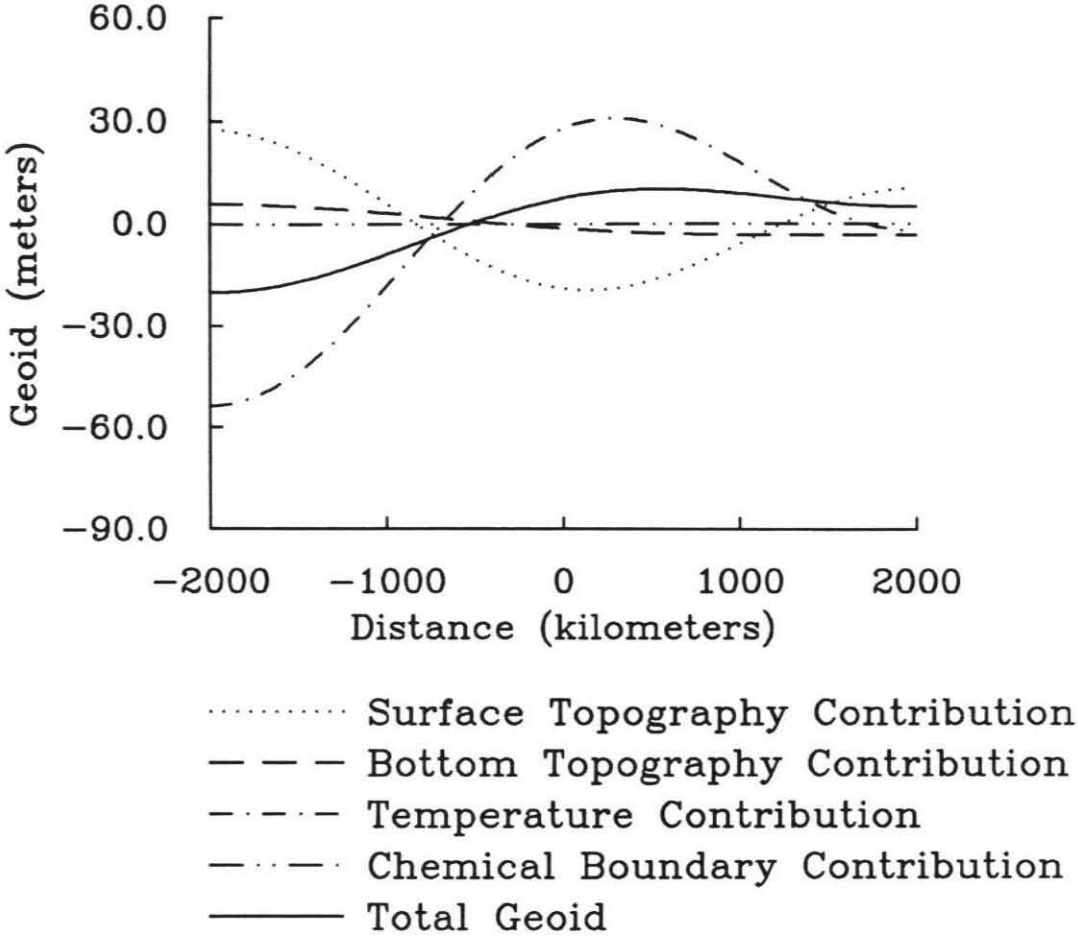

Figure 4.9: The long wavelength geoid and topography for the calculation shown Figure 4.7.

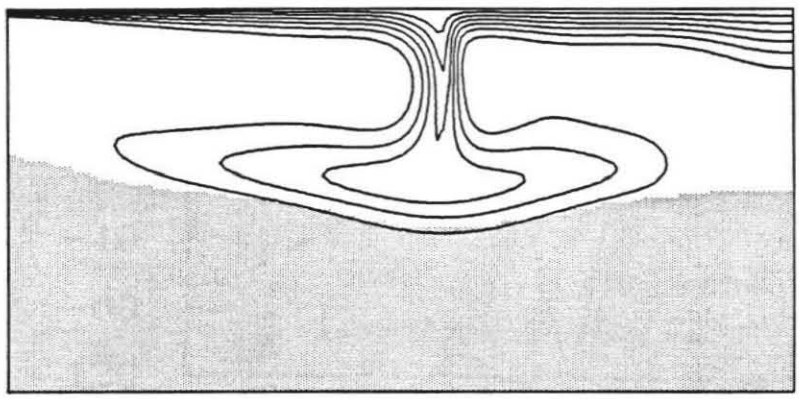

Figure 4.10: The temperature (line contours) and composition (shaded region) for a constant viscosity slab with a factor of 100 increase in viscosity and a 2% density discontinuity initially at $0.5d$.

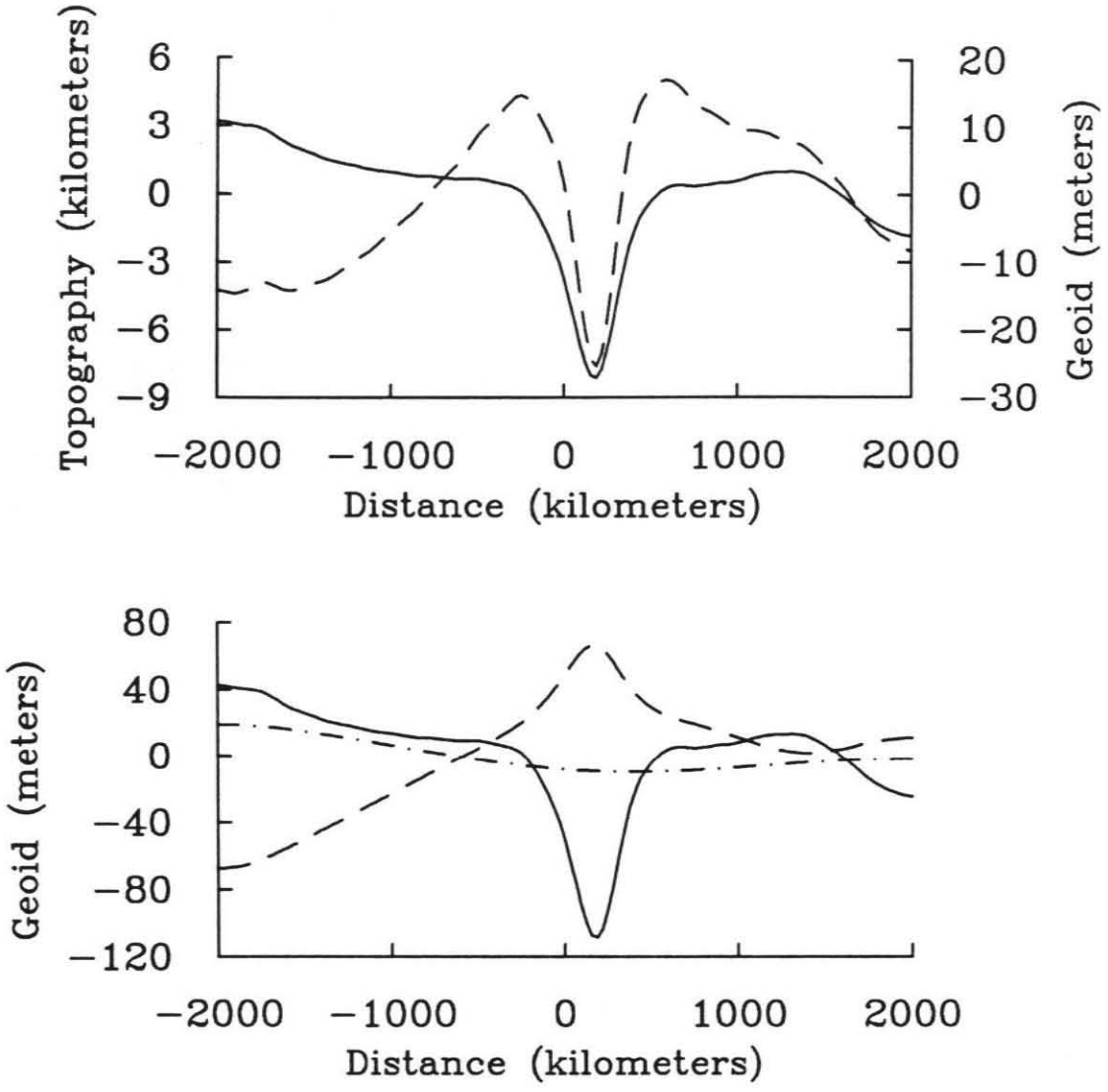

Figure 4.11: (top) The geoid (dashed line) and topography (solid line) for Figure 4.10. (bottom) The individual components of the geoid: surface topography (solid line), thermal density anomaly (dashed line), and deformation of the chemical boundary (dot-dashed line).

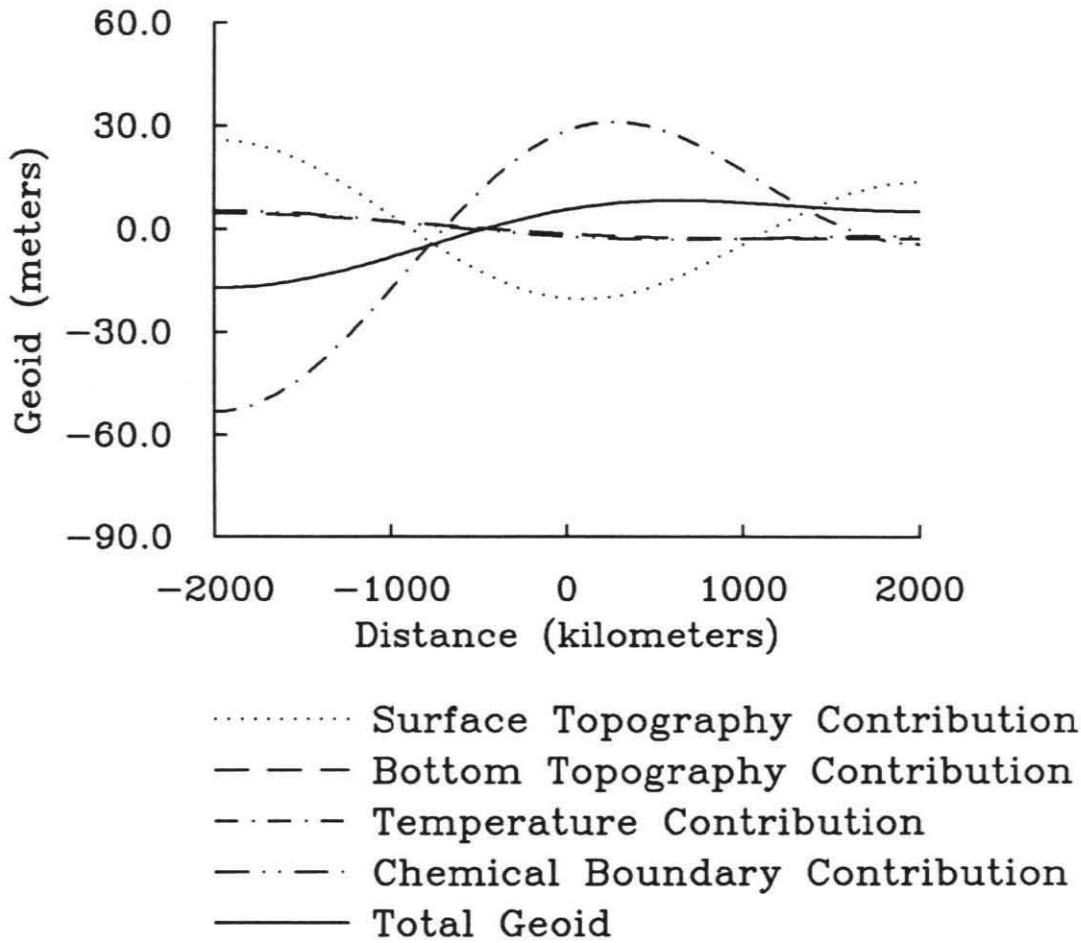

Figure 4.12: The long wavelength geoid and topography for the calculation shown Figure 4.10.

found in appendix E.) The Rayleigh number and boundary conditions for these calculations are the same as the calculations discussed above. As these calculations are time-dependent, and since we only show one snap-shot for each, we have picked a representative time step. The time step picked for each of the calculations is as close as possible to the maximum deflection of the boundary. The calculations with the low density contrast (i.e., 1%, $R = 0.72$ and 2%, $R = 0.5$) are distinguishable from the rest. These are the calculations with the maximum boundary deformation. For the other calculations, the slab deforms the boundary, but the density discontinuity and the amount of deformation of the boundary compensate each other, resulting in a nearly equal chemical boundary contribution to the geoid for these cases.

We also present the resulting geoid for calculations with: a density discontinuity, a viscosity discontinuity, a fixed boundary ($V_z = 0$), and no boundary in Figure 4.14. To make the comparison as close as possible, we use the same temperature field for each calculation and calculate the resulting geoid and topography. The fixed boundary represents the Richards and Hager chemically stratified models. They argue that a boundary with little or no deformation can be closely approximated by an impenetrable boundary. From Figure 4.14, the agreement for the 8% ($R = -3$) chemical boundary and the fixed boundary indicates that the fixed boundary is a good approximation when the amount of boundary deformation is small. However, when the slab sinks into the lower mantle, as in the 1% ($R = 0.75$) case, the agreement breaks down.

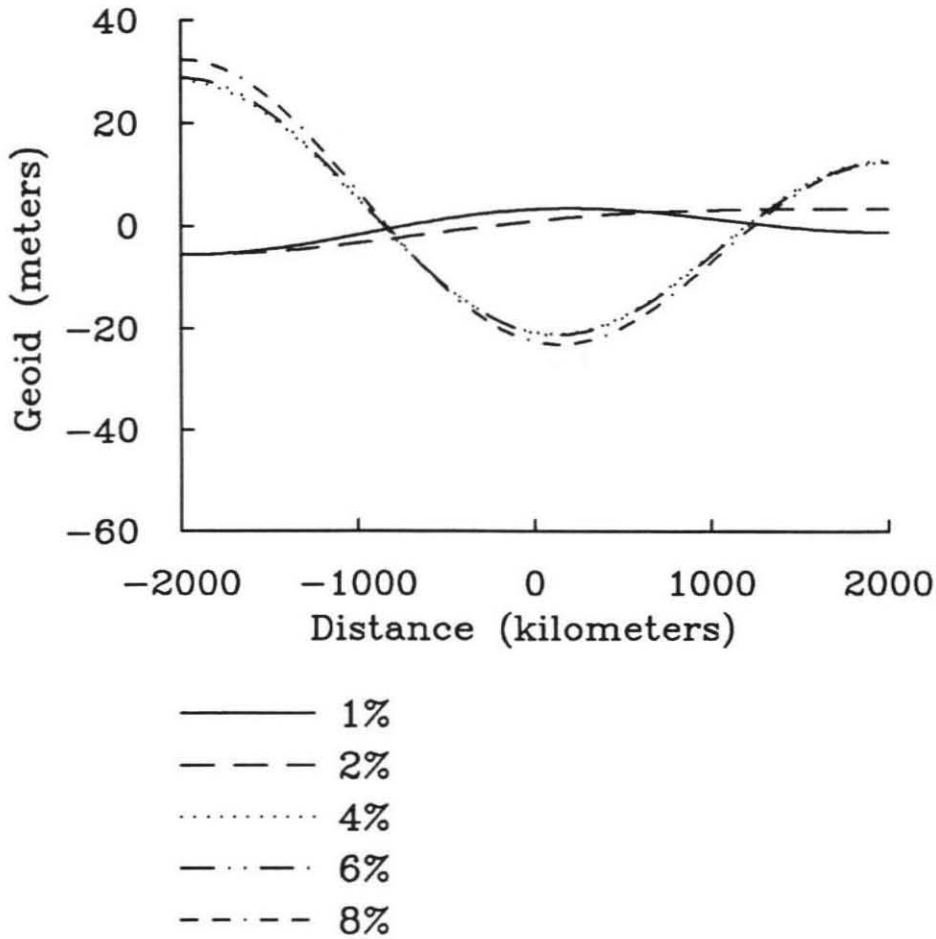

Figure 4.13: The long wavelength geoid for various density discontinuities.

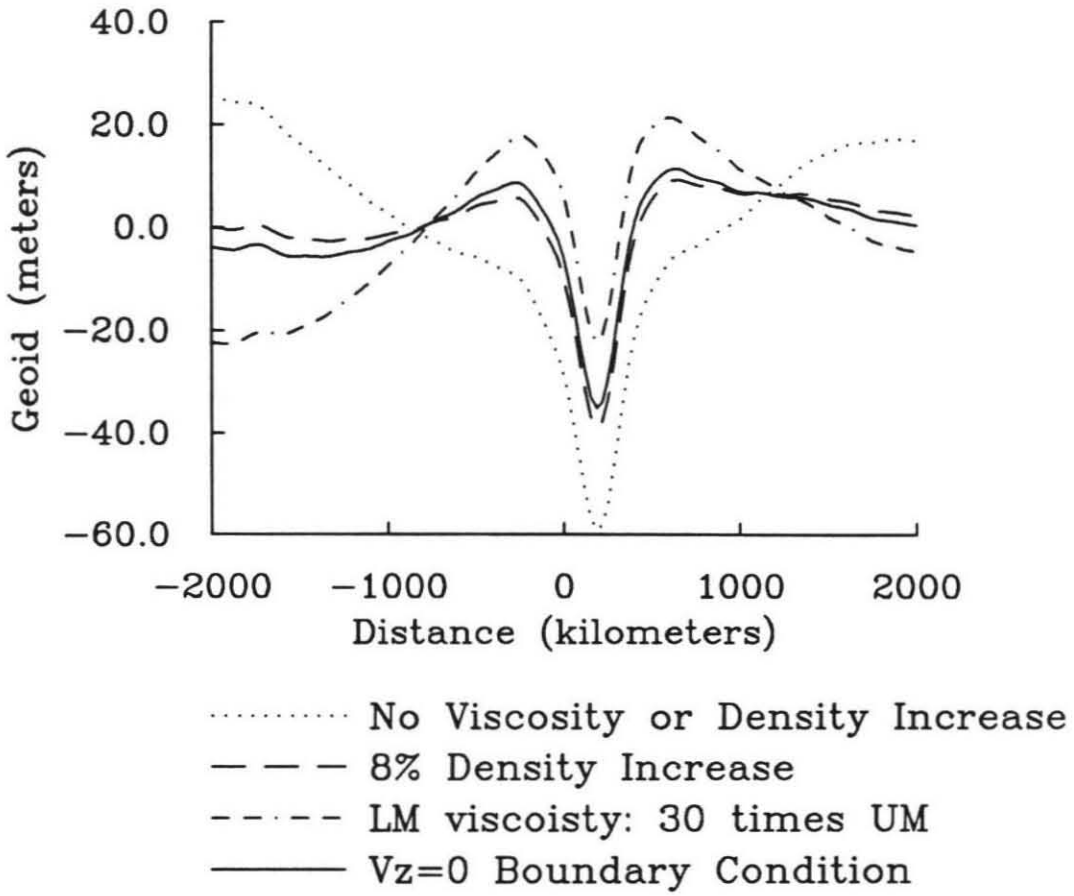

Figure 4.14: The geoid for a viscosity, density, imposed boundary, and no boundary.

4.2.2 Temperature-Dependent Calculations

One of the strengths of the method developed is the ability to calculate the geoid and topography over subduction zones with laterally varying viscosity. Willemann and Anderson (1987) examined the effect of a strong slab on the geoid, concluding that even for a strong slab a viscosity increase of about a factor of 10 at the 670 still results in a geoid high. The calculations by Willemann and Anderson used imposed tractions on both the plate and the slab. The slab was confined to the side of the computational mesh, much like the geometry used in Chapter 3. Imposing tractions on the slab means that the calculations are not dynamically consistent, since the slab is being driven by an unknown external force. This raises doubts about the applicability of these calculations to subduction zones. Also, the effects of density discontinuities were not explored.

Figure 4.15 shows both the temperature and composition fields for a temperature-dependent slab calculation. Unlike the constant viscosity calculations in the previous section, no velocities are imposed, but a weak zone method, similar to the method outlined in Chapter 3, is used. The Rayleigh number is 3×10^6 and the chemical Rayleigh number is 2×10^6 ($R = -0.33$). A dimensionless activation energy of 9.0 was used, and the viscosity cut-off was 6.6 (see Chapter 3 for details). We found that the choice of these parameters had more of an influence on the shape of the slab than it did on the long wavelength geoid.

The contributions to the geoid from the surface topography, the core mantle boundary topography, the temperature contributions, and the density discontinuity are shown in Figure 4.16. From the top figure, it is clear that the trench is about

6 times as deep as trenches observed on the Earth (e.g., Kogan, 1975). However, this is a short wavelength phenomenon, related to the parameterization of the weak zone. In the long wavelength geoid (Figure 4.17), the local effects of the trench do not effect the long wavelength geoid. Also, the effect of the density boundary, due to the lateral density variation, is small. Note that the density could also affect the topography by supporting the slab, and this effect cannot be directly separated from the topography.

In order to minimize the variations from calculation to calculation due to the time-dependence of the problem, we use the temperature field from Figure 4.15 as the "slab" for all the remaining calculations; we only run each calculation for one time-step to calculate the stresses and topography. This means that the slabs may not be dynamically consistent with the viscosity and density structure. However, the thermal contribution to the geoid will be the same from calculation to calculation. We can then address the dynamical consistency by running a longer calculation with the same viscosity and density structure and allow the slab to develop to ensure that the effects we observe are not artifacts of the slab geometry.

Figure 4.18 shows the geoid contributions for a constant viscosity calculation with no density discontinuity, using the temperature field from Figure 4.15. While there are significant differences in the short wavelength geoid, there is a striking similarity between the temperature-dependent slab geoid and the constant viscosity slab geoid at long wavelengths. The similarity between the long wavelength topography contribution in this case and the previous one demonstrates that there is no significant long wavelength component to the topography due to support of the slab by the

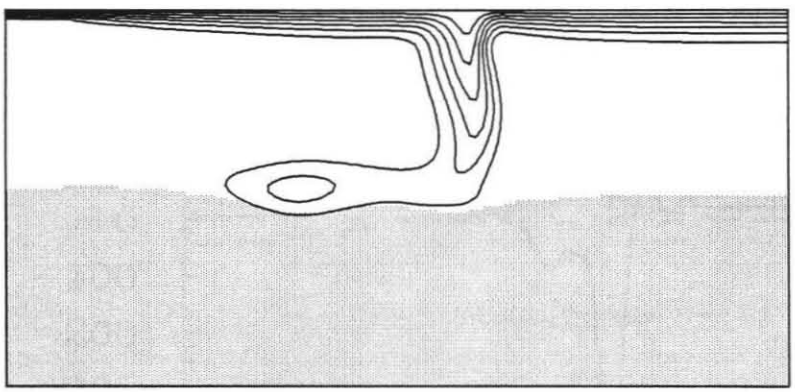

Figure 4.15: The temperature (line contours) and composition fields (shaded region) for a temperature-dependent viscosity slab with a 2% density increase ($R = -0.33$) at $0.5d$.

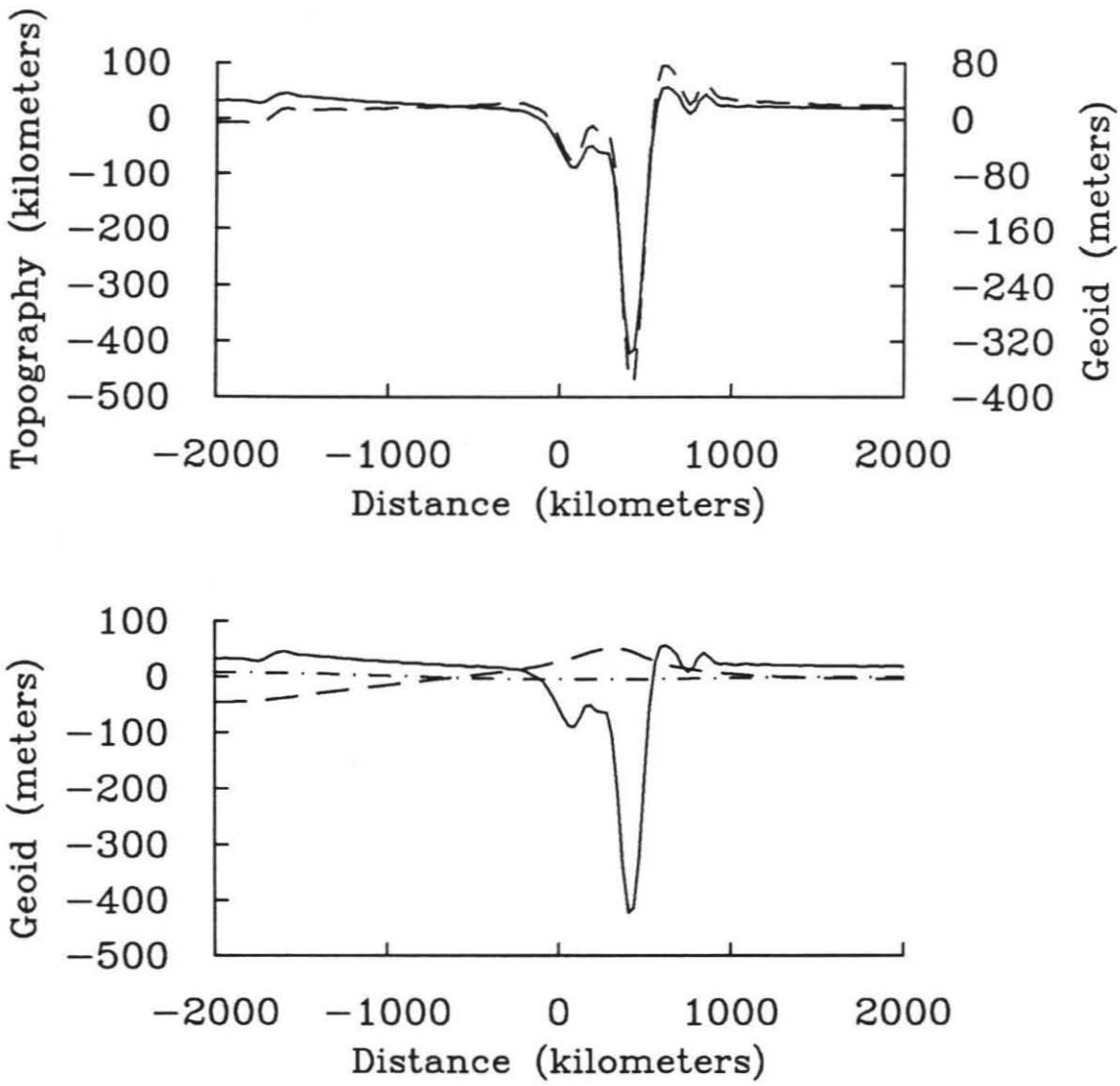

Figure 4.16: (top) The geoid and topography for the temperature field in Figure 4.15. (bottom) The individual components of the geoid: surface topography (solid line), thermal density anomaly (dashed line), and deformation of the chemical boundary (dot-dashed line).

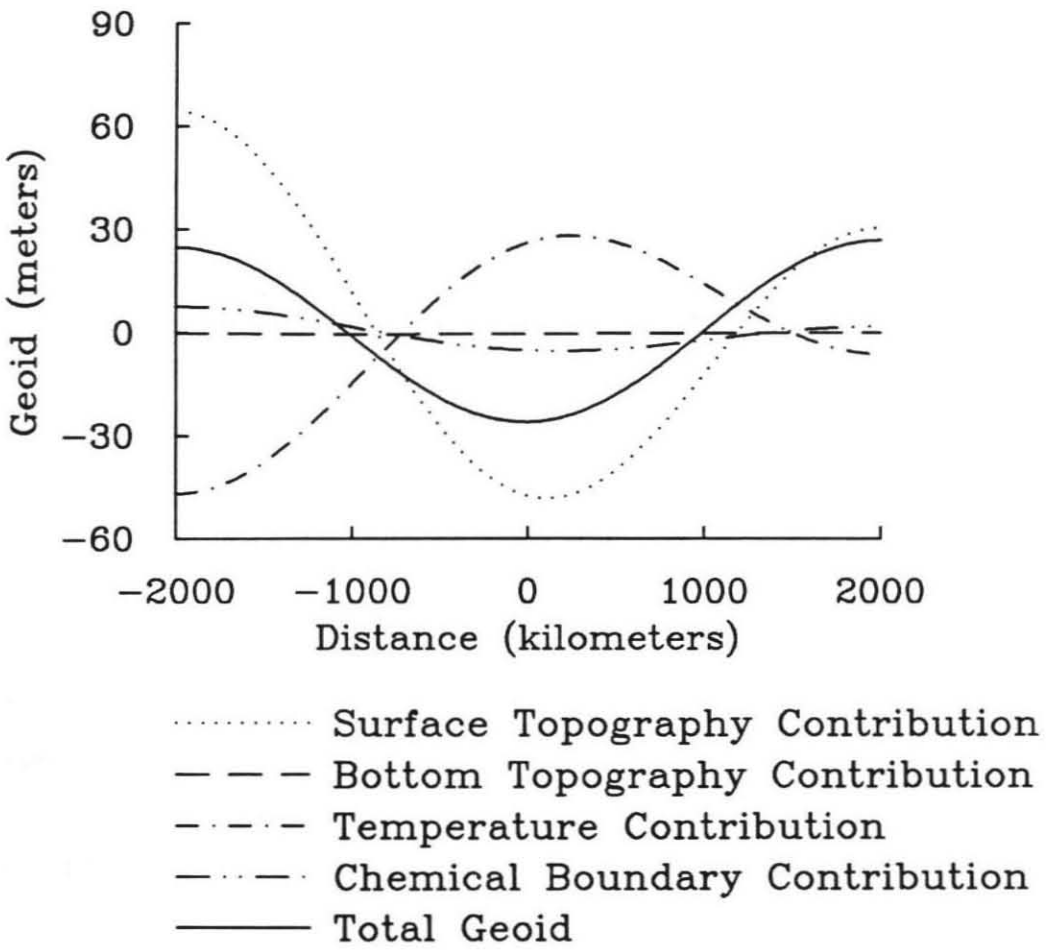

Figure 4.17: The long wavelength geoid and topography for the calculation shown Figure 4.15.

density boundary.

Once again, the viscosity discontinuity is quite different. Figure 4.19 shows the long wavelength geoid contributions from a calculation with a factor of 100 increase in viscosity at a depth of $0.5d$. The geoid is significantly higher in the region of the subduction zone, and while it is not clear from the figure, the geoid has changed sign. The geoid could be scaled by increasing the value of α.

The long wavelength geoid similarity is also observed for other types of viscosity parameterizations as well. Figure 4.20 is the long wavelength geoid from a non-Newtonian temperature-dependent slab; the non-Newtonian slabs have the same long wavelength geoid features. However, for the non-Newtonian calculation, a slab did not develop when the calculation was begun with a less mature slab (such as the slab in Figure 3.9b). Even with the strongly temperature-dependent viscosity, the slab re-organized into a flow with cells which were smaller than the imposed plate. Christensen and Yuen (1989) noted a similar preference for small aspect ratio cells in time-dependent non-Newtonian flows.

4.3 Summary

In order to understand the dynamical effects of the 670 kilometer discontinuity, more investigations are needed to understand the broad range of interesting, time-dependent, and complex phenomenon that we have observed with slabs and deformable boundaries. The relationship between maximum stress, direction of principal stress, and the direction of the flow becomes complicated near a density discontinuity. The plane of the maximum stresses and direction of maximum stresses

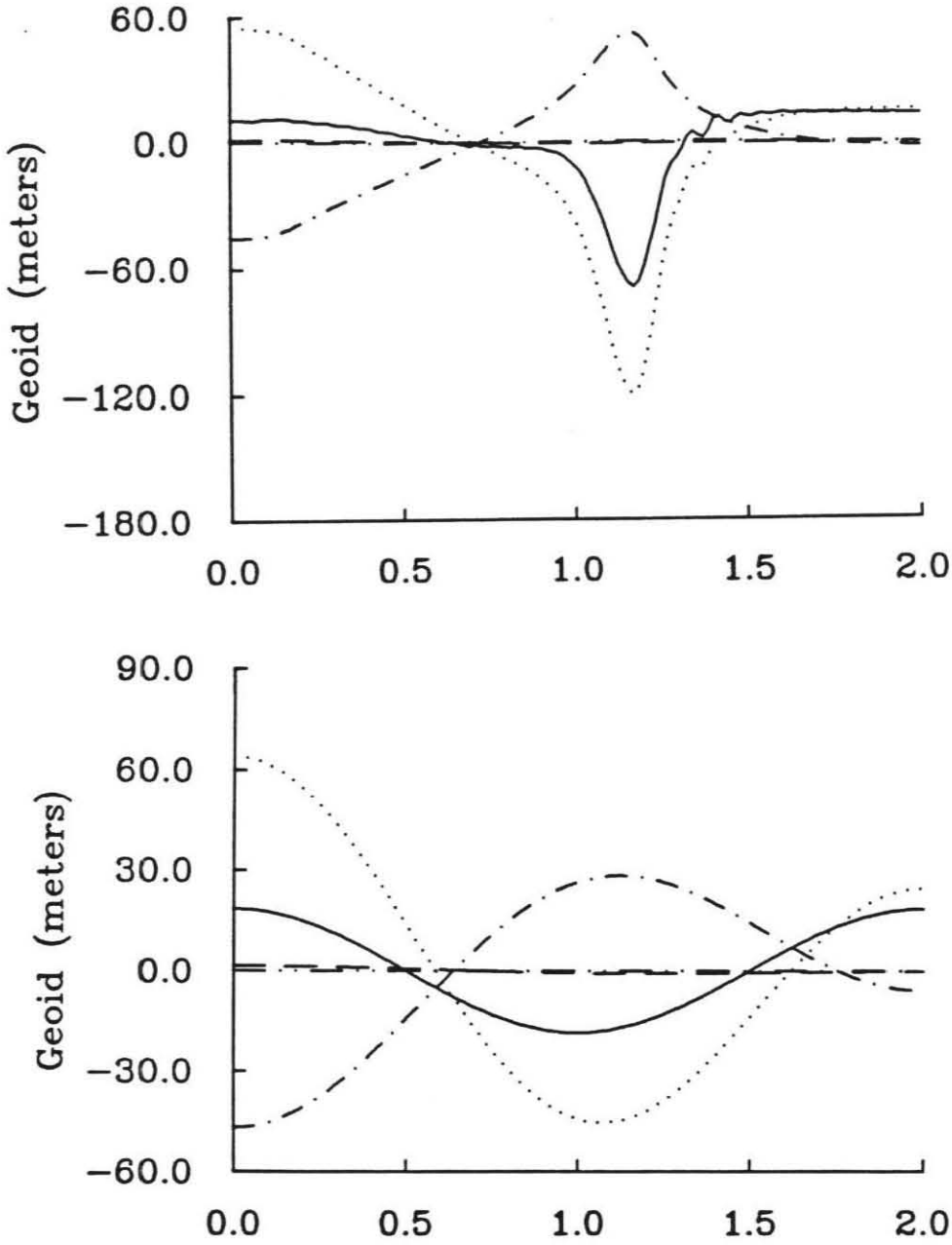

Figure 4.18: The full geoid (top) and long wavelength geoid (bottom) for a constant viscosity calculation using the temperature field from Figure 4.15.

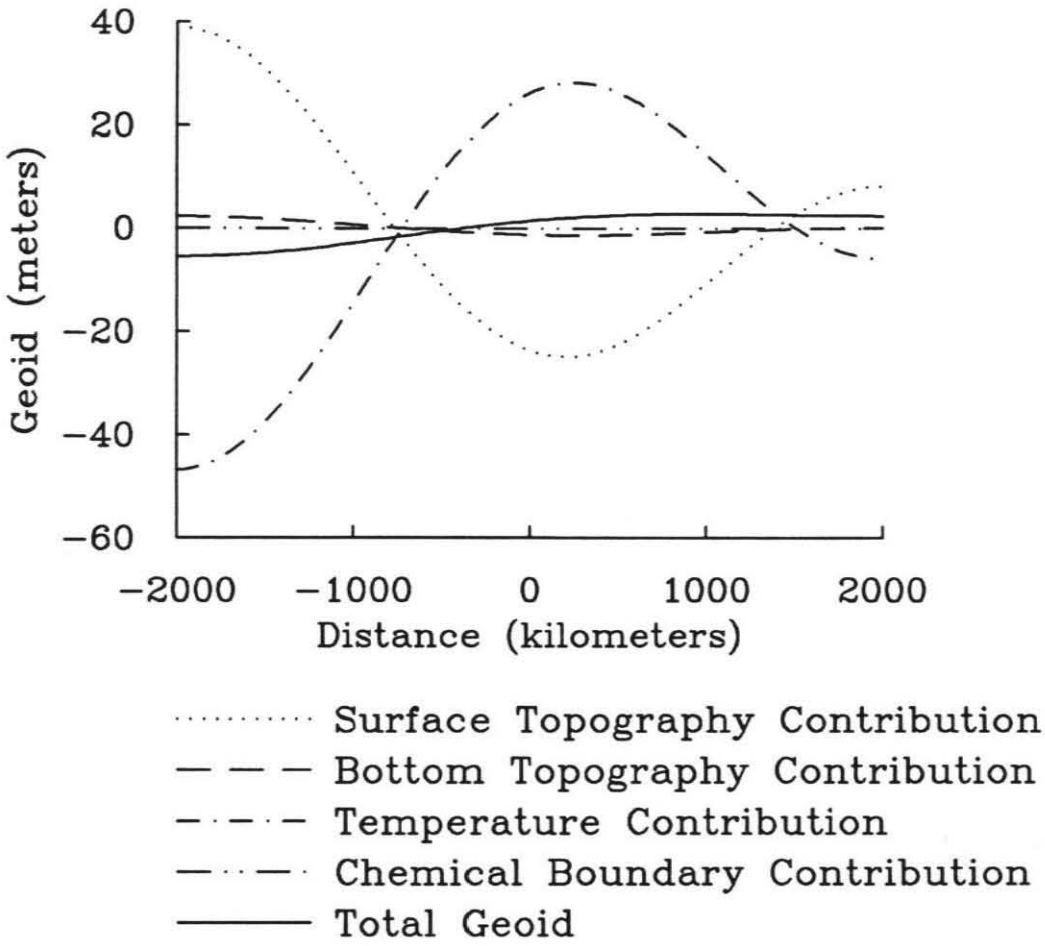

Figure 4.19: The long wavelength geoid and topography for a constant viscosity calculation with a 100-fold viscosity discontinuity at a depth of $0.5d$ using the temperature field from Figure 4.15.

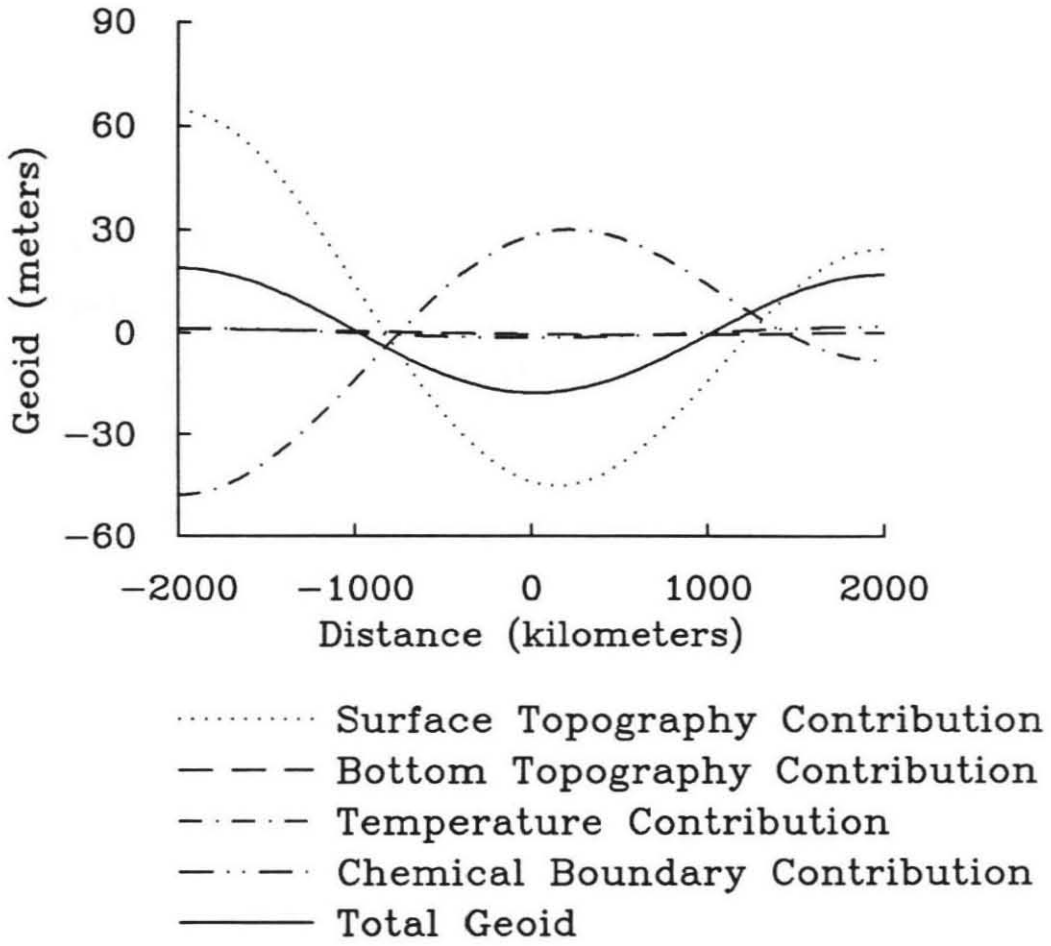

Figure 4.20: The long wavelength geoid and topography for a temperature-dependent non-Newtonian calculation.

are related to, but do not need to coincide with, the thermal anomaly. Also, the interpretation of seismic tomography images can become complicated when a density discontinuity is present.

The long wavelength geoid over subduction zones is insensitive to the parameterization of the slab. For constant viscosity, temperature-dependent viscosity, and non-Newtonian temperature-dependent viscosity slabs, the long wavelength geoid anomaly is almost identical given the same thermal slab. In particular, the long wavelength results from the temperature-dependent slab are not significantly different from the results for the same thermal slab with a constant viscosity. This confirms the assumption of Richards and Hager, that the effects of lateral viscosity variations on the long wavelength geoid is small.

We have examined the long wavelength geoid from a number of viscosity and density contrasts. In general, a density contrast alone is insufficient to generate long wavelength geoid highs, unless it is a small density contrast. A moderate or large density contrast along with a viscosity contrast cannot be ruled out; a viscosity contrast of a factor of at least 30 is needed for long wavelength geoid highs. However, other viscosity models have also been proposed. The relationship between viscosity, temperature, and pressure predicts a low-viscosity zone beneath the lithosphere (Parmentier, 1978; Fleitout and Yuen, 1984), where the viscosity decreases rapidly, due to the large temperature gradient with depth, and then increases, due to the increase in pressure with depth. Robinson, Parsons, and Driscoll (1988) use a low viscosity zone to model the geoid anomalies at fracture zones. Another, more speculative model advocated both by mineral physics (Karato, 1989; Meade and Jeanloz, 1990),

post-glacial rebound (Spada, Sabadini and Yuen, 1990), and Monte Carlo inversions (Ricard, Vigny, and Froidevaux, 1989) has a viscosity increase at 400 kilometers, then decreasing again at 670 kilometers. These models need to be examined in more detail.

The results from a dynamically deformable density discontinuity are nearly indistinguishable from the impenetrable approximation used by Richards and Hager, and the presence of a deformable density discontinuity does not change the conclusions of Richards and Hager (1984), Hager *et al.* (1985), and Hager and Richards (1989) when the deformation of the boundary is small. However, large boundary deformation can cause the long wavelength geoid over a subduction zone to become positive, although the results are time-dependent.

If is well known that mantle mineral assemblages undergo phase changes at pressures equivalent to 400 and 670 kilometers (e.g., Birch, 1952; Anserson, 1967; Anderson, 1970). The effects of phase changes, both the increase or decrease in density and the latent heat, could play a major role in the dynamics of slabs. Anderson (1987) points out that a major effect could be to increase the effective slab coefficient of thermal expansion, which would increase R. However, a more detailed study of the effects of phase changes in conjunction with compositional changes should be undertaken.

Understanding the relationship between the trench parameterization and the shorter, but still long, wavelength geoid and topography could lead to a better understanding of the deformation of oceanic plates at subduction zones. The trench topography may provide a much needed constraint for the weak zone parameteri-

zation, or a better understanding of the physics of the deformation at subduction zones.

Bibliography

Allègre, C. J., Chemical geodynamics, *Tectonophysics*, **81**, 109-132, 1982.

Allègre, C. J., and D. L. Turcotte, Geodynamic mixing in the mesosphere boundary layer and the origin of ocean islands, *Geophys. Res. Lett.*, **12**, 207-210, 1985.

Allègre, C. J., and D. L. Turcotte, Implications of a two-component marble-cake mantle, *Nature*, **323**, 123-127, 1986.

Anderson, D. L., Phase changes in the upper mantle, *Science*, **157**, 1165-1170, 1967.

Anderson, D. L., Petrology of the mantle, *Mineral. Soc. Amer. Spec. Pap.*, **3**, 85-93, 1970.

Anderson, D. L., The 650 km mantle discontinuity, *Geophys. Res. Lett.*, **3**, 347-349, 1976.

Anderson, D. L., Composition of the mantle and core, *Ann. Rev. Earth Planet. Sci.*, **5**, 179-202, 1977.

Anderson, D. L., Transition region of the Earth's upper mantle, *Nature*, **320**, 321-326, 1986.

Anderson, D. L., Thermally induced phase changes, lateral heterogeneity of the mantle, continental roots and deep slab anomalies, *J. Geophys. Res.*, **92**, 13,968-13,980, 1987.

Anderson, D. L., Chemical boundaries in the mantle, in: *Glacial isostacy, sea-level and mantle rheology*, ed R. Sabadini and K. Lambeck, Kluwer Academic Publishers, Dordrecht, in press.

Anderson, O. L., A. Choplas, and R. Boehler, Thermal expansivity versus pressure at constant temperature: a re-examination, *Geophys. Res. Lett.*, **17**, 685-688, 1990.

Ashby, M. F., and R. A. Verrall, Micromechanisms of flow and fracture, and their relevance to the rheology of the upper mantle, *Phil. Trans. R. Soc. Lond. A*, **288**, 59-95, 1977.

Ashcraft, C. C., R. G. Grimes, B. W. Peyton, and H. D. Simon, Progress in sparse matrix methods for large linear systems on vector supercomputers, *Int. J. Supercomput. Appl.*, **1**, 10-30, 1988.

Barkley, B. J., The origin of complexity in some P seismograms from deep earthquakes, *Geophys. J. R. Astr. Soc.*, **49**, 773-777, 1977.

Bercovici, D., G. A. Glatzmaier, and G. A. Schubert, Influence of heating mode on three-dimensional mantle convection, *Geophys. Res. Lett.*, **16**, 617-620, 1989a.

Bercovici, D., G. A. Glatzmaier, G. A. Schubert, and A. Zebib, 3-dimensional thermal-convection in a spherical shell, *J. Fluid Mech.*, **206**, 75-104, 1989b.

Bevis, M., The curvature of Wadati-Benioff zones and the torsional rigidity of subducting plates, *Nature*, **323**, 52-53, 1986.

Bevis, M., Seismic slip and down-dip strain rates in Wadati-Benioff zones, *Science*, **240**, 1317-1319, 1988.

Birch, F., Elasticity and constitution of the earth's interior, *J. Geophys. Res.*, **57**, 227-286, 1952.

Birch, F., Density and composition of the upper mantle: first approximation as an olivine layer, in: *The Earth's crust and upper mantle*, Geophys. Monogr. Ser., ed P. J. Hart, **13**, 18-36, 1969.

Blankenbach, B., F. Busse, U. Christensen, L. Cserepes, D. Gunkel, U. Hansen, H. Harder, G. Jarvis, M. Koch, G. Marquart, D. Moore, P. Olson, H. Schmeling, and T. Schnaubelt, A benchmark comparison for mantle convection codes, *Geophys. J. Int.*, **98**, 23-38, 1989.

Bock, G., and J. Ha, Short period S-P conversions in the mantle at a depth near 700 km, *Geophys. J. R. Astr. Soc.*, **77**, 593-615, 1984.

Brooks, A., A Petrov-Galerkin finite-element formulation for convection dominated flows, *Ph.d. Thesis, California Institute of Technology, Pasadena, CA*, 1981.

Brooks, A. N., and T. J. R. Hughes, Streamline upwind/Petrov-Galerkin formulations for convection dominated flows with particular emphasis on the incompressible Navier-Stokes equations, *Comp. Meth. in Appl. Mech. and Eng.*, **32**, 199-259, 1982.

Cathles, L. M. III, Viscosity of the Earth's Mantle, Princeton Univ. Press, Princeton, N. J., 1975.

Chandrasekhar, S. *Hydrodynamic and Hydromagnetic Stability*, Oxford University Press, Oxford, 1961.

Choplas, A., and R. Boehler, Thermal expansion measurements at very high pressure, systematics, and a case for a chemically homogeneous mantle, *Geophys. Res. Lett.*, **16**, 1347-1350, 1989.

Chopra, P. N., and M. S. Paterson, The experimental deformation of dunite, *Tectonophyics*, **78**, 453-473, 1981.

Christensen, U. R., Convection in a variable-viscosity fluid: Newtonian versus power-law rheology, *Earth Planet. Sci. Lett.*, **64**, 153-162, 1983.

Christensen, U. R., Heat transport by variable viscosity convection and implications for the Earth's thermal evolution, *Phys. Earth Planet Int.*, **35**, 264-282, 1984.

Christensen, U. R., Convection with pressure- and temperature- dependent non-Newtonian rheology, *Geophys. J. R. Astr. Soc.*, **77**, 343-384, 1984.

Christensen, U. R., Time-dependent convection in elongated Rayleigh-Benard cells, *Geophys. Res. Lett.*, **14**, 220-223, 1987.

Christensen, U. R., and D. A. Yuen, The interaction of a subducting lithospheric slab with a chemical or phase boundary, *J. Geophys. Res.*, **89**, 4389-4402, 1984.

Christensen, U. R., and D. A. Yuen, Time-dependent convection with non-Newtonian viscosity, *J. Geophys. Res.*, **94**, 814-820, 1989.

Cray Research, Inc., CFT optimization guide, *Cray Research, Inc.*, Mendota Heights, MN, document SG-0115 1/88, 120 pp., 1987.

Creager, K. C., and T. H. Jordan, Slab penetration into the lower mantle, *J. Geophys. Res.*, **89**, 3031-3049, 1984.

Creager, K. C., and T. H. Jordan, Slab penetration into the lower mantle beneath the Mariana and other island arcs of the northwest Pacific, *J. Geophys. Res.*, **91**, 3573-3589, 1986.

Cserepes, L., Numerical studies of non-Newtonian mantle convection, *Phys. Earth Planet Int.*, **30**, 49-61, 1982.

Daly, S. F., and A. Raefsky, On the penetration of a hot diapir through a strongly temperature-dependent viscosity medium, *Geophys. J. R. Astr. Soc.*, **83**, 657-681, 1985.

Davies, D., and D. P. McKenzie, Seismic travel time residuals and plates, *Geophys. J. R. Astr. Soc.*, **18**, 51-63, 1969.

Davies, G. F., Mechanics of subducted lithosphere, *J. Geophys. Res.*, **85**, 6304-6318, 1980.

Davies, G. F., Regional compensation of subducted lithosphere: effects on geoid, gravity and topography from a preliminary model, *Earth Planet. Sci. Lett.*, **54**, 431-441, 1981.

Davies, G. F., Subduction zone stresses: constraints from mechanics and from topographic and geoid anomalies, *Tectonophysics*, **99**, 85-98, 1983.

Davies, G. F., Geophysical and isotopic constraints on mantle convection: an interim synthesis, *J. Geophys. Res.*, **89**, 6017-6040, 1984.

Davies, G. F., Mantle convection under simulated plates: effects of heating modes, ridge and trench migration, and implications for the coure-mantle boundary, bathymetry, the geoid and Benioff zones, *Geophys. J. R. Astr. Soc.*, **84**, 153-183, 1986.

Davies, G. F., Role of the lithosphere in mantle convection, *J. Geophys. Res.*, **93**, 10451-10466, 1988a.

Davies, G. F., Ocean bathymetry and mantle convection 1. large-scale flow and hot spots, *J. Geophys. Res.*, **93**, 10467- 10480, 1988b.

Davies, G. F., Ocean bathymetry and mantle convection 2. small-scale flow, *J. Geophys. Res.*, **93**, 10481-10488, 1988c.

Davies, G. F., Mantle convection model with a dynamic plate: topography, heat-flow and gravity anomalies, *Geophys. J.*, **98**, 461-464, 1989.

Dongarra, J. J., Performance of various computers using standard linear equations software in a fortran environment, *Argonne National Laboratory Technical Memorandum*, **23**, 1987.

Dongarra, J. J., and S. C. Eisenstat, Squeezing the most out of an algorithm in Cray fortran, *ACM Trans. Math. Software*, **10**, 219-230, 1984.

Duffy, T. S., and D. L. Anderson, Seismic velocities in mantle minerals and the mineralogy of the upper mantle, *J. Geophys. Res.*, **94**, 1895-1912, 1989.

Elsasser, W. M., Sea floor spreading and thermal convection, *J. Geophys. Res.*, **76**, 1101-1111, 1971.

Fischer, K. M., K. C. Creager, and T. H. Jordan, Mapping the Tonga slab, *J. Geophys. Res.*, **in press**, 1990.

Fischer, K. M., and T. H. Jordan, Seismic strain rate and deep slab deformation in Tonga, *J. Geophys. Res.*, **in press**, 1990.

Fleitout, L., and D. A. Yuen, Secondary convection and the growth of the oceanic lithosphere, *Phys. Earth Planet Int.*, **36**, 181-212, 1984.

Gable C., R. J. O'Connell, and B. J. Travis, Convection in three dimensions with surface plates: Generation of toroidal flow, *J. Geophys. Res.*, **submitted**, 1990.

Gable C., R. J. O'Connell, and B. J. Travis, Plate motions in models of 3-D convection with layered viscosity: Implications for mantle flow, *EOS trans. AGU*, **69**, 44, 1414, 1988.

Garfunkel, Z., C. A. Anderson, and G. A. Schubert, Mantle circulation and the lateral migration of subducted slabs, *J. Geophys. Res.*, **91**, 7205-7223, 1986.

Giardini, D., and J. H. Woodhouse, Deep seismicity and modes of deformation in Tonga subduction zone, *Nature*, **307**, 505-509, 1984.

Grand, S., Tomographic inversion for shear velocity beneath North America, *J. Geophys. Res.*, **92**, 14,065-14,090, 1987.

Gudmundsson, O., J. H. Davies, and R. W. Clayton, Stochastic analysis of global traveltime data: Mantle heterogeneity and random error in the ISC data, *Geophys. J. Int.*, **102**, 25-43, 1990.

Gurnis, M., and B. H. Hager, Controls on the structure of subducted slabs and the viscosity of the lower mantle, *Nature*, **335**, 317-321, 1988.

Gutenburg, B., and C. F. Richter, Magnitude and energy of earthquakes, *Nature*, **176**, 795-796, 1955.

Hager, B. H., Global isostatic geoid anomalies for plates and boundary layer models of the lithosphere *Earth Planet. Sci. Lett.*, **63**, 97-109, 1983.

Hager, B. H., Subducted slabs and the geoid: Constraints on mantle rheology and flow, *J. Geophys. Res.*, **89**, 6003-6015, 1984.

Hager, B. H., R. W. Clayton, M. A. Richards, R. P. Comer, and A. M. Dziewonski, Lower mantle heterogeneity, dynamic topography and the geoid, *Nature*, **313**, 541-545, 1985.

Hager, B. H., and R. J. O'Connell, A simple global model of plate dynamics and mantle convection, *J. Geophys. Res.*, **86**, 4843-4867, 1981.

Hager, B. H., and A. Raefsky, Deformation of seismic discontinuities and the scale of mantle convection, *EOS trans. AGU*, **62**, 1074, 1981.

Hager, B. H., and M. A. Richards, Long-wavelength variations in Earth's geoid: physical models and dynamical implications, *Phil. Trans. R. Soc. Lond. A*, **328**, 309-327, 1989.

Hansen, U., and D. A. Yuen, Dynamical influences from thermal-chemical instabilities at the core-mantle boundary, *Geophys. Res. Lett.*, **16**, 629-632, 1989a.

Hansen, U., and D. A. Yuen, Subcritical double-diffusive convection at infinite Prandtl number, *Geophys. Astrophys. Fluid Dynamics*, **47**, 199-224, 1989b.

Hoffman, N. R. A., and D. P. McKenzie, The destruction of geochemical heterogeneities by differential fluid motions during mantle convection, *Geophys. J. Roy. Astr. Soc.*, **82**, 162-206, 1985.

Ho-Liu, P., B. H. Hager, and A. Raefsky, An improved method of Nusselt number calculation, *Geophys. J. Roy. Astr. Soc.*, **88**, 205-215, 1987.

Houseman, G., The dependence of convection planform on mode of heating, *Nature*, **332**, 346-349, 1988.

Hughes, T.J.R., The finite element method, *Prentice-Hall, Inc.*, Englewood Cliffs, New Jersey, 1987.

Hughes, T. J. R., and A. N. Brooks, A multi-dimensional upwind scheme with no crosswind diffusion, In: *Finite element methods for convection dominated flows*, ASME, New York, **34**,19-35 1982.

Hughes, T. J. R., L. P. Franca, G. M. Hulbert, Z. Johan, and F. Shakib, The Galerkin/least-squares method for advective-diffusive equations, In: *Recent developments in computational fluid dynamics*, T. E. Tezduyar (Editor), ASME, New York, **95**,75-99, 1987.

Hughes, T. J. R., W. K. Liu, and A. N. Brooks, Finite element analysis of incompressible viscous flows by the penalty function formulation, *J. Comput. Phys.*, **30**, 19-35, 1979.

Isacks, B. L., J. Oliver, and L. R. Sykes, Seismology and the new global tectonics, *J. Geophys. Res.*, **73**, 5855-5899, 1968.

Isacks, B. L., and P. Molnar, Distribution of stresses in the descending lithosphere from a global survey of focal mechanism solution of mantle earthquakes, *Rev. Geophys. Space Phys.*, **9**, 103-174, 1971.

Jeanloz, R., and A. B. Thompson, Phase transitions and mantle discontinuities, *Rev. Geophys. Space Phys.*, **21**, 51-74, 1983.

Jeffreys, H., The times of *P, S*, and *SKS*, *Mon. Not. R. Astron. Soc., Geophys. Suppl*, **4**, 498-533, 1939.

Jones, G. M., Isostatic geoid anomalies over trenches and island arcs *Tectonophysics*, **99**, 119-137, 1983.

Jordan, T. H., Lithospheric slab penetration into the lower mantle beneath the Sea of Okhotsh, *J. Geophys.*, **43**, 473-496, 1977.

Karato, S., Plasticity-crystal structure systematics in dense oxides and its implications for the creep strength of the Earth's deep interior, *Phys. Earth Planet Int.*, **55**, 234-240, 1989.

Kaula, W. M., Global gravity and tectonics, In: *The nature of the solid Earth*, E. C. Robertson (Editor), 386-405, McGraw-Hill, New York, 1972.

Kellogg, L. H., and C. S. Stewart, Mixing and the distribution of heterogeneities in a chaotically convecting mantle, *J. Geophys. Res.*, **95**, 421-432, 1990.

Kincaid, C., and P. L. Olson, An experimental study of subduction and slab migration, *J. Geophys. Res.*, **92**, 13,832-13,840, 1987.

King, S. D., R. F. Lucas, and A. Raefsky, Using a multifrontal sparse solver in a high performance finite element code, *Int. J. Supercomput. Appl.*, **submitted**, 1990.

King, S. D., A. Raefsky, and B. H. Hager, ConMan: Vectorizing a finite element code for incompressible two-dimensional convection in the earth's mantle, *Phys. Earth Planet Int.*, **59**, 196-208, 1990.

Knittle, E., R. Jeanloz, and G. L. Smith, Thermal expansion of silicate perovskite and stratification of the Earth's mantle, *Nature*, **319**, 214-216, 1986.

Kogan, M. G., Gravity field of the Kuiril-Kamchatka Arc and its relation to the thermal regime of the lithosphere, *J. Geophys. Res.*, **80**, 1381-1390, 1975.

Kopitzke, U., Finite element convection models: Comparison of shallow and deep mantle convection and temperatures in the mantle, *J. Geophys.*, **46**, 97-121, 1979.

Lees, A. C., M. T. S. Bukowinski, and R. Jeanloz, Reflection properties of phase transitions and compositional change models of the 670-km discontinuity, *J. Geophys. Res.*, **88**, 8145-8159, 1983.

Levesque, J. M., and J. W. Williamson, A guidebook to fortran on supercomputers, *Academic Press*, San Diego, 1989.

Lucas, R. F., Solving planer systems of equations on distributed memory multiprocessors, *Ph.D. Thesis, Stanford University*, Palo Alto, CA, 1988.

Machetel P., and D. A. Yuen, Chaotic axisymmetrical spherical convection and large-scale mantle circulation, *Earth Planet. Sci. Lett.*, **86**, 93-104, 1987.

Malkus, D. S., and T. J. R. Hughes, Mixed finite element methods reduced and selective integration techniques: a unification of concepts, *Comp. Meth. in Appl. Mech. and Eng.*, **15**, 63-81 1978.

McAdoo, D. C., Geoid anomalies in the vicinity of subduction zones, *J. Geophys. Res.*, **86**, 6073-6090, 1981.

McKenzie, D. P., J. M. Roberts, and N. O. Weiss, Convection in the earth's mantle: towards a numerical simulation, *J. Fluid Mech.*, **62**, 465-538, 1974.

McKenzie, D. P., The importance of high temperature creep, In: *The history of the Earth's crust, Proc. NASA Conf.*, pp. 28, Princeton University Press, 1968.

McKenzie, D. P., The viscosity of the Earth, *Geophys. J. Roy. Astr. Soc.*, **14**, 279-305, 1967.

Meade, C., and R. Jeanloz, The strength of mantle silicates at high pressures and room temperature: implications for the viscosity profile of the mantle, *Nature*, **submitted**, 1990.

Melosh, H. J., Dynamic support of the outer rise, *Geophys. Res. Lett.*, **5**, 321-324, 1978.

Melosh, H. J., and A. Raefsky, The dynamical origin of subduction zone topography, *Geophys. J. Roy. Astr. Soc.*, **60**, 333-354, 1980.

Nataf, H. C., and F. M. Richter, Convection experiments in fluid with highly temperature-dependent viscosity and the thermal evolution of the planets, *Phys. Earth Planet Int.*, **29**, 320-329, 1982.

Nataf, H. C., S. Moreno, and Ph. Cardin, What is responsible for thermal coupling in layered convection?, *J. Phys. France*, **49**, 1707-1714, 1988.

Olson, P. L., and D. A. Yuen, Thermochemical plumes and mantle phase transitions, *J. Geophys. Res.*, **87**, 3993-4002, 1982.

Parmentier, E. M., A study of thermal convection in non-Newtonian fluids, *J. Fluid Mech.*, **84**, 1-11, 1978.

Parmentier, E. M., D. L. Turcotte, and K. E. Torrance, Studies of finite amplitude non-Newtonian thermal convection with application to convection in the Earth's mantle, *J. Geophys. Res.*, **81**, 1839-1846, 1976.

Parsons, B. E., and G. L. Sclater, An analysis of the variation of ocean floor bathymetry and heat flow with age, *J. Geophys. Res.*, **82**, 803-827, 1977.

Perkris, C. L., Thermal convection in the interior of the Earth, *Mon. Not. R. Astron. Soc., Geophys. Suppl.*, **3**, 343-367, 1935.

Peyret, R., and T. D. Taylor, Computational methods for fluid flow, *Springer-Verlag*, New York, 1983.

Rabinowicz, M., B. Lago, and M. Souriau, Large-scale gravity profiles across subducted plates, *Geophys. J. Roy. Astr. Soc.*, **73**, 325-349, 1983.

Reynard, B., and G. Price, Thermal expansion of mantle minerals at high pressures - a theoretical study, *Geophys. Res. Lett.*, **17**, 689-692, 1990.

Ricard, Y., L. Fleiotout, and C. Froidevaux, Geoid heights and lithospheric stresses for a dynamic Earth, *Ann. Geophys.*, **2**, 267-286, 1984.

Ricard, Y., C. Vigny, and C. Froidevaux, Mantle heterogeneities, geoid, and plate motion, a monte carlo inversion, *J. Geophys. Res.*, **94**, 13,739-13,754, 1989.

Richards, M. A., and C. W. Wicks Jr., S-P conversions from the transition zone beneath Tonga and the nature of the 670 km discontinuity, *Geophys. J. Int.*, **101**, 1-35, 1990.

Richter, F. M., Focal mechanisms and seismic energy release of deep and intermediate earthquakes in the Tonga-Kermadec region and their bearing on the depth extent of mantle flow. *J. Geophys. Res.*, **84**, 6783-6795, 1979.

Richter, F. M., Dynamical models for sea floor spreading, *Rev. Geophys. Space Phys.*, **11**, 223-278, 1973.

Richter, F. M., and C. E. Johnson, Stability of a chemically layered mantle, *J. Geophys. Res.*, **79**, 1635-1639, 1974.

Richter, F. M., H. C. Nataf, and S. Daly, Heat transfer and horizontally averaged temperature of convection with large viscosity variations, *J. Fluid Mech.*, **129**, 173-192, 1983.

Richter, F. M., and D. P. McKenzie, Simple plate models of mantle convection, *Jour. Geophys.*, **44**, 441-471, 1978.

Richter, F. M., and D. P. McKenzie, On some consequences and possible causes of layered mantle convection, *J. Geophys. Res.*, **86**, 6133-6142, 1981.

Ringwood, A. E., and T. Irifune, Nature of the 670-km seismic discontinuity: implications for mantle dynamics and differentiation, *Nature*, **331**, 131-136, 1988.

Ringwood, A. E., Phase transitions and the constitution of the mantle, *Phys. Earth Planet Int.*, **3**, 109-155, 1970.

Robinson, E., B. Parsons, and M. Driscoll, The effect of a shallow low-viscosity zone on the mantle flow, the geoid anomalies and the geoid and depth-age relationships at fracture zones, *Geophys. J.*, **93**, 25-43, 1988.

Schmeling, S., and W. R. Jacoby, On modeling the lithosphere in mantle convection with non-linear rheology, *J. Geophys*, **50**, 89-100, 1981.

Schubert, G., D. A. Yuen, and D. L. Turcotte, Role of phase transitions in a dynamic mantle, *Geophys. J. Roy. Astr. Soc.*, **42**, 705-735, 1975.

Silver, P.G., R. W. Carlson, and P. Olson, Deep slabs, geochemical heterogeneity, and the large-scale structure of mantle convection: Investigation of an enduring paradox, *Ann. Rev. Earth Planet. Sci.*, **16**, 477-541, 1988.

Spada, G., R. Sabadini, and D. A. Yuen, The dynamical influences of a hard transition zone on postglacial uplifts and rotational signatures, *Phys. Earth Planet Int.*, **in press**, 1990.

Suzuki, I., Thermal expansion of periclase and olivine, and their anharmonic properties, *J. Phys. Earth*, **23**, 145-159, 1975.

Sykes, L. R., Seismicity and deep structure of island acrs, *J. Geophys. Res.*, **71**, 2981-3006, 1966.

Temam, R., Navier-Stokes equations: theory and numerical analysis, North-Holland, Amsterdam, 1977.

Travis, B. J., C. Anderson, J. Baumgardner, C. Gable, B. H. Hager, P. Olson, R. J. O'Connell, A. Raefsky, and G. Schubert, A benchmark comparison of numerical methods for infinite Prandtl number convection in two-dimensional Cartesian geometry, *Geophys. Astrophys. Fluid Dynamics*, **submitted**, 1990.

Turcotte, D. L., and E. R. Oxburgh, Finite amplitude convective cells and continental drift, *J. Fluid Mech.*, **28**, 29-42, 1967.

Turcotte, D. L., and G. Schubert, Structure of the olivine-spinel phase boundary in the descending lithosphere, *J. Geophys. Res.*, **76**, 7980-7987, 1971.

Vassiliou, M. S., Stresses in subduction slabs as revealed by earthquakes analyzed by moment-tensor inversion, *Earth Planet. Sci. Lett.*, **69**, 195-202, 1984.

Vassiliou, M. S., and B. H. Hager, Subduction zone earthquakes and stress in slabs, *PAGEOPH*, **128**, 547-624, 1988.

Vassiliou, M. S., B. H. Hager, and A. Raefsky, The distribution of earthquakes with depth and stress in subduction slabs, *J. Geodynamics*, **1**, 11-28, 1984.

Vidale, J. E., Waveform effects of a high velocity, subducted slab, *Geophys. Res. Lett.*, **14**, 542-545, 1987.

Wasserburg, G. J., and D. J. DePaolo, Models of Earth structure inferred from neodymuim and strontium isotopic abundances. *Proc. Natl. Acad. Sci. USA*, **76**, 3594-3598, 1979.

Weertman, J., The creep strength of the Earth's mantle, *Rev. Geophys. Space Phys.*, **8**, 145-168, 1970.

Wilemann, R. J. and C. A. Anderson, Modeling geoid anomalies due to subduction of inextensible lithosphere, *Geophys. Res. Lett.*, **14**, 820-823, 1987.

Yuen, D. A., R. Sabadini, and E. V. Boschi, Viscosity of the lower mantle as inferred from rotational data, *J. Geophys. Res.*, **87**, 10745-10762, 1982.

Zhang, J., B. H. Hager, and A. Raefsky, A critical assessment of viscous models of trench topography and corner flow, *Geophys. J. Roy. Astr. Soc.*, **83**, 451-475, 1985.

Zhou, H., Mapping of *P*-wave slab anomalies beneath the Tonga, Kermadec and New Hebrides arcs, *Phys. Earth Planet Int.*, **61**, 199-229, 1990.

Zhou, H., and D. L. Anderson, Search for deep slabs in the Northwest Pacific mantle, *Proc. Natl. Acad. Sci. USA*, **86**, 8602-8606, 1989.

Zhou, H., D. L. Anderson, and R. W. Clayton, Modeling of residual spheres for subduction zone earthquakes, 1, apparent slab penetration signatures in the NW pacific caused by deep diffuse mantle anomalies, *J. Geophys. Res.*, **95**, 6799-6828, 1990.

Zhou, H., and R. W. Clayton, *P* and *S* wave travel time inversions for subducting slab under island arcs of the northwest pacific, *J. Geophys. Res.*, **95**, 6829-6852, 1990.

Appendix A

ConMan on Various Computers

Timing results for various computers are presented from ConMan for a constant viscosity (CVBM) and temperature-dependent viscosity (TDBM) problem. Both benchmarks are 32 by 32 element problems and all computers use only FORTRAN routines; no special assemble language kernels are used. However, for vector machines, compiler directives are used to force vectorization of ambiguous loops. For all machines the maximum level of optimization, which gives the correct result, is used by the compiler. Where available, both vector (V) and scalar (S) times are given; all times are normalized to the scalar Cray X-MP time. For machines with multiple CPUs, times reflect single processor speeds only.

CVBM is a constant viscosity problem, so the matrix is only factored once, and CVBM is run for 5000 time steps. TDBM is a temperature-dependent viscosity problem, so the matrix is factored each time step, and TDBM is run for 1000 time steps. For both problems, a banded matrix solver is used. There are a total of 2046 equations in the global stiffness matrix and the average half-bandwidth is 65.

This means that 4.3 million operations are required to factor the matrix and 133,000 operations are required for the forward reduction and backsubstitution.

Computer	CVBM	TDBM
Cray Y-MP V	31.18	26.07
Cray X-MP V	18.73	15.29
Cray 2 V	15.92	10.62
Convex C210 V	4.27	3.10
Alliant FX40 V	1.70	1.07
Convex C120 V	1.40	1.42
IBM 6000-320	1.25	—
Ardent Titan V	1.23	1.54
Cray X-MP S	1.00	1.00
Sun 4-330	0.42	0.79
Sun SparcStation 1	0.37	0.61
Sun 4-260 fpu2	0.34	0.59
Convex C120 S	0.31	0.42
Sun 4-260	0.28	0.48
Ardent Titan S	0.27	0.28

Table A.1: Execution speeds normalized to the Cray X-MP scalar execution speed for a constant viscosity problem (CVBM) and a temperature-dependent problem (TDBM) using ConMan. For real time comparisons, CVBM on a Cray X-MP scalar takes 2869.3 seconds and TDBM takes 6094.7 seconds.

Appendix B

Non-Newtonian Implementation and Verification

We use the two-dimensional Cartesian finite element convection code ConMan, described in Chapter 2 as the starting point for our non-Newtonian code. ConMan uses the penalty method to enforce incompressibility and Streamline-Upwind Petrov-Galerkin weighting functions for the advective term of the energy equation. The time stepping is done with a predictor-corrector algorithm which is second order accurate in space and time so that the time evolution of the flow can be followed reliably. For Newtonian convection ConMan has been benchmarked against detailed results presented for other Cartesian codes (Travis *et al.*, 1990).

For the non-Newtonian calculations, the relationship between stress and strain rate is given by

$$\dot{\epsilon} = A\left(\frac{\sigma}{\sigma_o}\right)^n \tag{B.1}$$

where $\dot{\epsilon}$ is the second invariant of the strain-rate tensor, σ is the second invariant

of the stress tensor, σ_o is the reference stress, n is the power law exponent and A expresses the temperature, pressure and compositional dependence of the viscosity. A has units of $\frac{\text{stress}}{\text{viscosity}}$ in this formulation and is given by

$$A = \frac{\sigma_o}{\eta_o e^{(E^*+V^*P)/kT}} \tag{B.2}$$

where η_o is the reference viscosity, E^* is the activation energy, V^* is the activation volume, P is the pressure, T is the temperature and k is the Boltzmann constant. The effective viscosity is defined by

$$\eta_{\text{eff}} = \frac{\sigma}{2\dot{\epsilon}} \tag{B.3}$$

Using (1) and (3) two forms of the effective viscosity can be defined

$$\eta_{\text{eff}}^{(\text{strain})} = \frac{\sigma_o}{2A^{\frac{1}{n}}\dot{\epsilon}^{(1-\frac{1}{n})}} \tag{B.4}$$

$$\eta_{\text{eff}}^{(\text{stress})} = \frac{\sigma_o^n}{2A\sigma^{(n-1)}} \tag{B.5}$$

where $\eta_{\text{eff}}^{(\text{stress})}$ is the stress form of the effective viscosity and $\eta_{\text{eff}}^{(\text{strain})}$ is the strain-rate form of the effective viscosity. Either form of the effective viscosity leads to a non-linear equation for the velocity, since the effective viscosity now depends on the stress or the strain-rate. The Stokes equation is solved iteratively using the stress or strain-rate from the previous iteration to obtain the new effective viscosity.

We tested both the stress and the strain-rate formulation of the effective viscosity along with a formulation where a geometric mean of the two formulations is used as in

$$\eta_{\text{eff}}^* = \left[\eta_{\text{eff}}^{(\text{stress})}\right]^x \left[\eta_{\text{eff}}^{(\text{strain})}\right]^{(1-x)} \tag{B.6}$$

where x is the weighting factor. For a simple shear problem where a uniform velocity is imposed at the surface, the sides are free slip and the bottom is pinned, the analytic solution is calculated as follows:

$$\dot{\epsilon} = V_s/2 \tag{B.7}$$

where $\dot{\epsilon}$ is the strain-rate and V_s is the imposed surface velocity. For a non-Newtonian rheology,

$$\dot{\epsilon} = \eta_o \sigma^n \tag{B.8}$$

and choosing $\eta_o = 1$

$$\sigma = (V_s/2)^{1/n} \tag{B.9}$$

The numerical results from ConMan for simple shear with $V_s = 100.0$ and $n = 3$ on a 32 by 32 grid are shown in Table B.1 for various ratios of stress and strain-rate weighting. The value at each node in the grid is the same as the value presented in the table to round off precision.

We next considered Poiseuille flow, where the velocities along the top and bottom were pinned in both the x (horizontal) and z (vertical) directions and a shear stress boundary condition of the form

$$\frac{\partial \sigma_{xz}}{\partial z} = C, \tag{B.10}$$

where C is a constant, was imposed along the left ($x = 0$) and right ($x = 1$) hand sides of the box. The maximum velocity and the number of iterations are shown in Table B.2 for various ratios of stress and strain-rate weighting.

For steady, non-Newtonian, simple shear and Poiseuille flow problems the iterative method converges to the analytic solution with only a few iterations. The full

Weighting	Final Stress	Number of Iterations
100% Strain	3.68398	1
90% Strain	3.68401	7
60% Strain	3.68402	35
55% Strain	—	>35

Table B.1: A non-Newtonian simple shear test on a 32 by 32 element grid with an imposed surface velocity, $V_s = 100$ and stress exponent, $n = 3$. The stress is uniform throughout the domain and the analytic solution is 3.68403.

Weighting	Final Maximum Velocity	Number of Iterations
100% Strain	31.1904	15
40% Strain	31.1893	7
0% Strain	31.0956	1

Table B.2: A non-Newtonian Poiseuille flow test on a 32 by 32 element grid with a stress exponent, $n = 3$. The maximum velocity occurs at z=0.5.

stress form of the viscosity, although optimal for Poiseuille flow, is unstable for buoyancy driven problems. The strain-rate form is stable but converges slowly as seen in Table B.2, except for imposed velocity problems (Table B.1).

To assess the optimal weighting for buoyancy driven problems we began with a steady, non-Newtonian, non-temperature-dependent convection calculation from Parmentier, Torrance and Turcotte (1976). We then started a calculation with the final temperature field, set the effective viscosity to one, and began iterating to recover the effective viscosity and temperature field. Each iteration, we measured the change in global kinetic energy and the maximum change in effective viscosity to assess when the solution had converged. The results for three representative ratios of stress to strain-rate weighting are shown in Figures B.1, B.2 and B.3. Clearly the 25% stress weighted formulation (B.2) converges the fastest.

For time-dependent problems, since the time stepping is explicit, it is limited by the Courant condition, which means the fluid can move no more than 1/2 element each time step. Thus, the distribution of effective viscosity evolves slowly. Because of this, the previous time steps viscosity field is a good starting condition for the first iteration of the next time step. As a result, after the first time step, which may take as many as 20 iterations to converge (see Figure B.2), each time step converges in only 2 or 3 iterations. We tested this by following an initial transient for one overturn using 1, 2, 5, and 10 iterations per time step. There was no significant difference between the 2, 5, and 10 iteration per time step calculations; however, the 1 iteration per time step calculation deviated slightly from the rest.

The non-Newtonian method was further tested by comparing steady-state calcu-

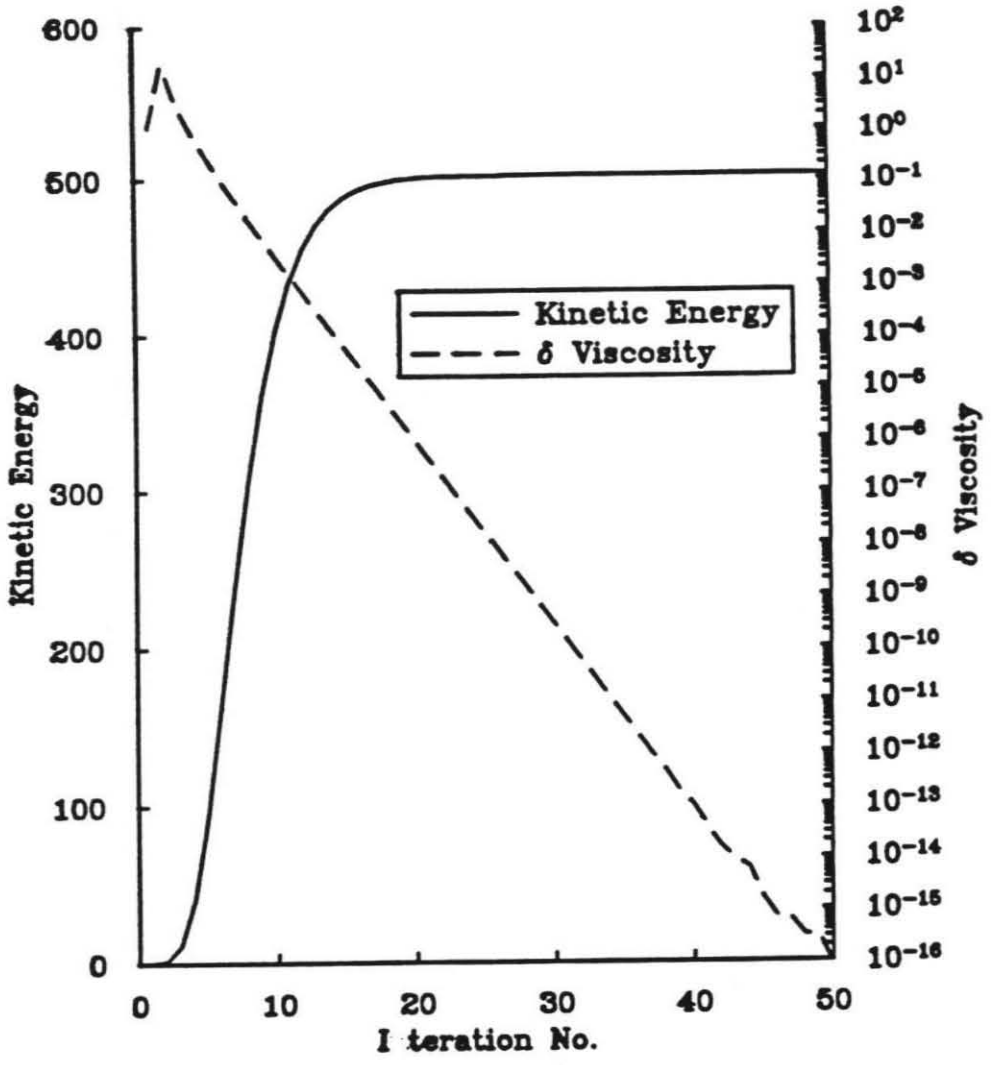

Figure B.1: Kinetic energy and maximum effective viscosity change as a function of iteration for a fully strain weighted (0% stress) non-Newtonian convection calculation on a 32 by 32 element grid. The initial condition was a steady temperature field from a non-Newtonian calculation and the effective viscosity reset to one.

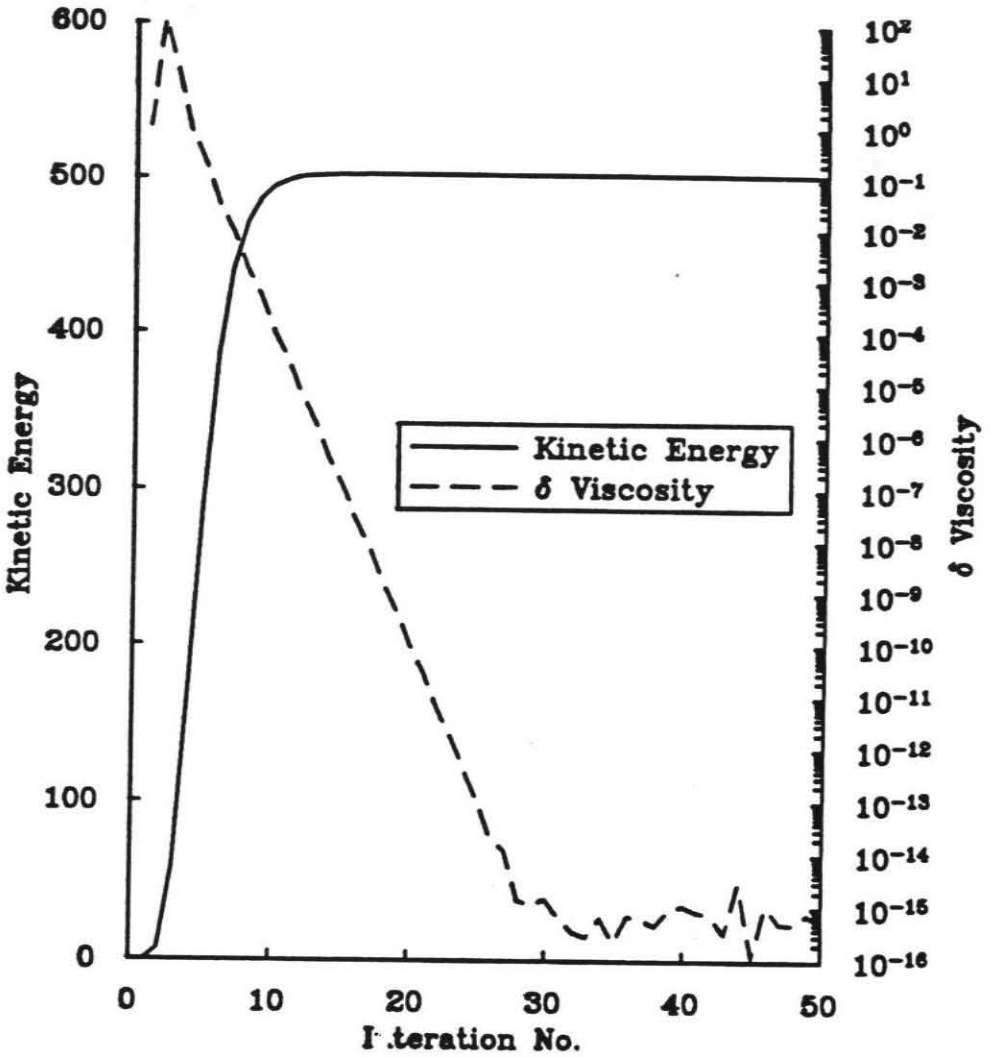

Figure B.2: Kinetic energy and maximum effective viscosity change as a function of iteration for a 25% stress weighted non-Newtonian convection calculation on a 32 by 32 element grid. The initial condition was a steady temperature field from a non-Newtonian calculation and the effective viscosity reset to one.

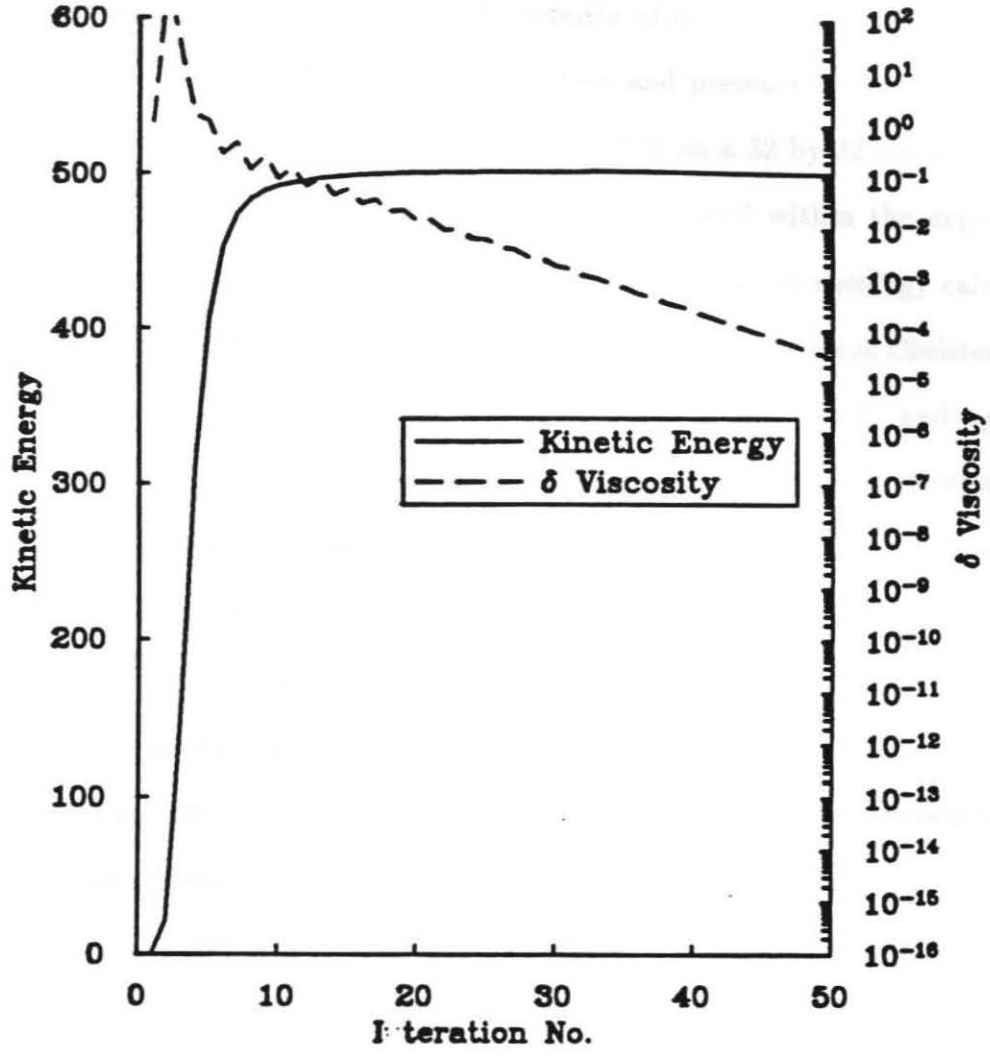

Figure B.3: Kinetic energy and maximum effective viscosity change as a function of iteration for a 45% stress weighted non-Newtonian convection calculation on a 32 by 32 element grid. The initial condition was a steady temperature field from a non-Newtonian calculation and the effective viscosity reset to one.

lations with no temperature- or pressure-dependence of rheology (Parmentier, Torrance and Turcotte, 1976) and strongly temperature and pressure-dependent rheology (Christensen, 1983). Our results agree to within 1% on a 32 by 32 element grid for the non-temperature or pressure-dependent rheology, well within the expected grid error. For the strongly temperature- and pressure-dependent rheology calculations, the solution on a 32 by 32 element grid is time-dependent whereas Christensen reports a steady solution. The solution on the 64 by 64 grid is steady and agrees with Christensen's. This behavior is surprising since apparently steady Newtonian flows are often found to be time-dependent when the grid resolution is increased, because excess diffusion stabilizes the under-resolved flows. The reverse case, apparently time-dependent flows which become steady with increased resolution, has not been previously reported in non-Newtonian calculations, to our knowledge, although Machetel and Yuen (1987) find a similar behavior for spherical-shell convection using a finite-difference scheme.

Appendix C

Calculation of Geoid, Topography and Deformed Boundaries

There are at least three sources of density anomalies which contribute to the geoid. They are the density anomalies which result from the temperature distribution (which enter the equations through the coefficient of thermal expansion), the density anomalies which arise from the deformation of the top and the bottom surface, and the density anomalies which arise from the deformation of any interior surfaces (such as changes in chemical composition or phase changes). The changes arising from deformation of an interior boundary are conceptually similar to topography of the top and bottom. In numerical calculations, the top and the bottom of the box do not actually deform, but can be approximated by a Taylor expansion of the stress to a hypothetical free surface. This is a good approximation since the topography at the surface and core mantle boundary are small compared to the depth of the mantle. However, the internal boundary may have hundreds of kilometers of topog-

raphy. Pekeris (1935) demonstrated that for the Earth, the surface and core mantle boundary topography cannot be neglected in the calculation of the geoid. Thus, to calculate the geoid correctly the topography must be calculated.

C.1 Topography

Topography can be calculated directly from stress. If the surface were allowed to deform the topography would take a shape such that there was no net tractions acting on the surface. Since in numerical calculations the surface cannot deform, and since the amount of surface topography is small compared to the depth of the box, the topography can be calculated from the following Taylor expansion approximation:

$$\tau_{zz}(h) = 0 = \tau_{zz}(0) + \delta h \Delta \rho g \tag{C.1}$$

where δh is height a free surface would take relative to the reference height (z=0), which is the top of the box, $\Delta\rho$ is the density contrast across the surface, and g is the force of gravity.

Stresses can be calculated from density fields using a propagator matrix technique (e.g., Cathes, 1975) or stresses can be calculated directly from the velocity field in the finite element formulation. The propagator method can only solve for stresses when the viscosity is constant throughout or constant within horizontal layers. Therefore, temperature-dependent models cannot be considered. The stresses from the finite element method are calculated at the element interiors and must be "smoothed" to the nodes and the boundaries. Interior node smoothing is well understood; Hughes (1987) discusses smoothing in some detail as do Ho-Liu, Raefsky and Hager (1987), although they discuss smoothing in the context of the Nusselt number. The stress

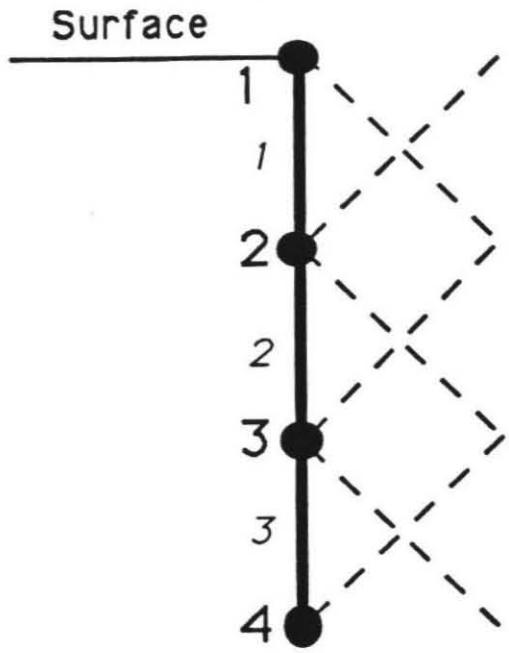

Figure C.1: One-dimensional analytic problem to test stress smoothing at the surface. The node numbers are shown in bold typeface and the element numbers are shown in slanted typeface. The dashed lines show the one-dimensional, linear shape-functions.

at an interior node is simply the area weighted average of the stresses from the four surrounding elements (see, e.g., Hughes, 1987 pp. 227-231).

However, smoothing stresses at the surface is not quite so direct. Consider the following one-dimensional example from Figure C.1. A single point buoyancy force is applied at one node, with the assumption that all nodes considered are close to the boundary. In this case, the magnitude of the stress at the surface (and in the interior near the point force) is equal to the point force. It is easy to calculate the values of the stress within the elements and at the surface, as a result of the finite element smoothing, for this simple one-dimensional problem. These are shown in Table C.1.

node	n_1 analytic	e_1 FEM	e_2 FEM	n_1 smoothed	n_2 smoothed	n_1 fixed
1	1/2	1/6	0	1/6	1/12	1/4
2	1	5/6	1/6	5/6	1/2	7/6
3	1	1	5/6	1	11/12	13/12
4	1	1	1	1	1	1

Table C.1: Results for the analytic test of the finite element smoothing. Figure C.1 depicts the finite element discretization for this problem. A point buoyancy force of 1 unit is applied at the node in column 1, and the stresses within the element and at the nodes are shown: n_1 analytic is the analytic answer for the stress at the surface (node 1), e_1 FEM is the value of the stress within element 1, e_2 FEM is the value of the stress within element 2, n_1 smoothed is the value of the stress at node 1 (after smoothing), n_2 smoothed is the value of the stress at node 2 (after smoothing) and n_1 fixed is the value of the stress at node 1 after the boundary correction is applied.

For a point buoyancy of 1, (in units of ρg) the stress should be identically 1 (in units of ρg), as long as the point buoyancy is near the surface. Once away from the boundary (i.e., node 4) this is true, but near the boundary the stress smoothing breaks down. Typically, a fix is applied to correct for the presence of the boundary. The fix is a linear projection of the stress in element 2 and element 1 projected to an imaginary element above the boundary. The top node is then smoothed using this imaginary element and the real element below it. The results of this fix are shown in the column labeled n_1 fixed. While it can be shown in general that this fix is a least-squares best approximation for general smoothing (Hughes, 1987), for the topography from density driven flow, we can do better. Examining Table C.1, it is clear that after the fix, the stress due to the buoyancy in the second row is overestimated by a factor of 1/6, and the stress in the third row is overestimated by a factor of 1/12. (The stress due to the buoyancy at the surface (row 1) is underestimated by 3/4 but the surface is usually a constant boundary condition.)

We compare our topography results with those of Christensen (Blankenbach *et al.*, 1989) in Figure C.2. We plot the topography at x=0 from a unit aspect ratio isoviscous convection calculation at a Rayleigh number of 10^5 for various size grids. We present: Christensen's results, the results with the propagator method (including the first 5 harmonics), the smoothing plus standard fix, and the smoothing plus new fix. Christensen uses higher order cubic-spline elements, which are more accurate and more computationally expensive than our linear elements. (One might think that stresses are only first-order accurate within linear elements; however, it is easy to show that at the integration points the stresses are second-order accurate). The new

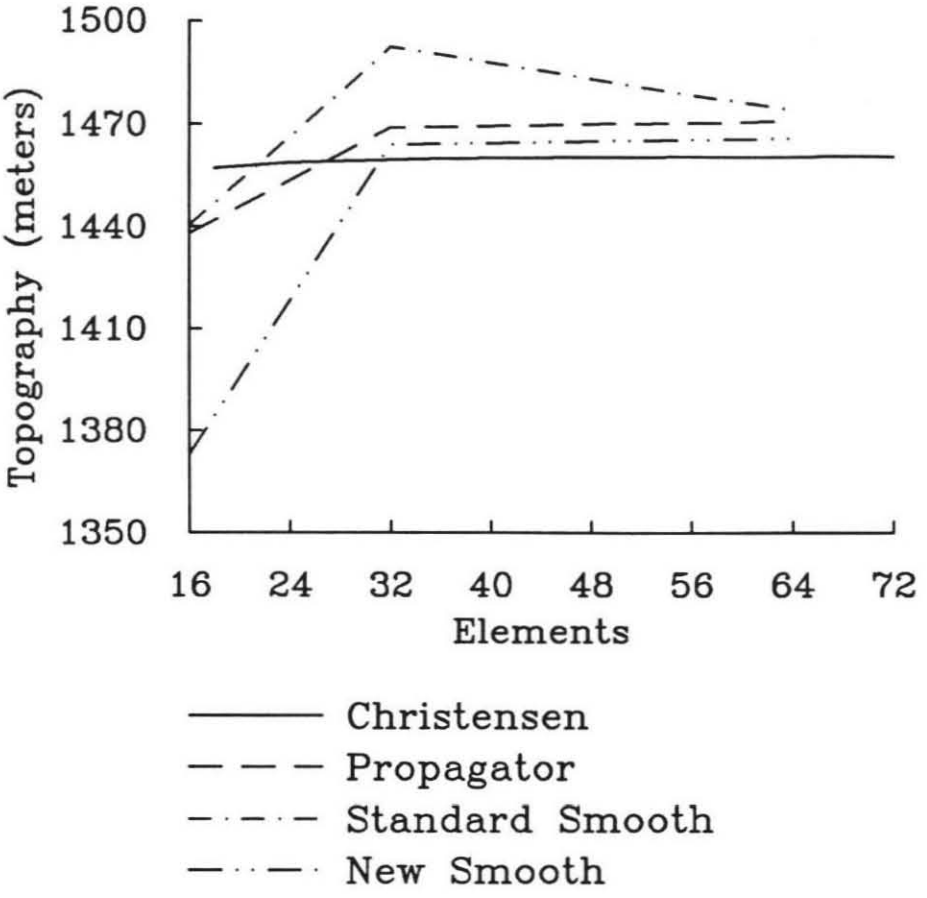

Figure C.2: A comparison of topography calculations at x=0 for isoviscous convection in a unit aspect ratio box with a Rayleigh number of 10^5 for various size grids. Christensen's results are from Blankenbach *et al.* (1989) while the propagator method is from Hager and O'Connell (1981) and the standard smooth and new smooth are from ConMan. For the propagator and the two smoothing methods the same temperature and velocity fields are used so differences reflect differences in the topography calculation only.

fix is slightly better than the old fix for all but the underresolved 16 by 16 element grid. However, the new fix does not make a significant difference because the top three rows are within the thermal boundary layer and the horizontal temperature, hence density, differences in the thermal boundary layer are small. Although for subduction problems, the horizontal density difference near the surface could become significant.

C.2 Geoid

It is most convenient to separate the horizontal and vertical dependencies of a given density field when considering the resulting geoid anomalies of that field. If the horizontal dependence is expressed in terms of harmonic functions, then for a flat earth, the contribution to the geoid ($N_k(x)$) from a density contrast $\Delta\rho_k(z)$, of wavelength k, can be written:

$$N_k(x) = \frac{2\pi G}{kg} e^{ikx} \int_0^h \Delta\rho_k e^{-kz} dz \tag{C.2}$$

where G is the gravitational constant, h is the depth over which the density contrast extends (in the z direction) and x is the horizontal position vector. Hager (1983) showed that the geoid from this flat earth model does not differ greatly from that calculated from a spherical model for all but the longest wavelengths.

In the calculations presented in Chapter 4, there are three sources for $\Delta\rho$: the topography on the top and bottom of the box (discussed in the previous section), the density due to temperature anomalies, and the deformation of any internal compositional boundaries. Thus, for each wavelength k, $\Delta\rho$ can be written as:

$$\Delta\rho = \frac{\tau_{zz}|_{z=0}}{g} + \frac{\tau_{zz}|_{z=h}}{g} \times e^{-kh} + \rho\alpha \int_0^h \Delta T(z) e^{-kz} dz - \int_0^h \Delta C(z) e^{-kz} dz \tag{C.3}$$

where the dependence of τ_{zz}, $\Delta T(z)$ and $\Delta C(z)$ on wavelength k was dropped for notational convenience. Several methods of calculating the chemical buoyancy were implemented and tested, but to calculate the geoid we always projected the element density to the nodes using a "smoothing" technique and calculated the chemical buoyancy contribution to the geoid in the same manner as the temperature contribution.

C.3 Chemical Composition Methods

In the work presented in Chapter 4, the compositional field was calculated by advecting a "chain" of markers and following fluid which is initially above or below the chain. (Once the fluids begin to intermix or overturn "above" or "below" become somewhat meaningless.) The tracking algorithm is able to keep track of the fluid even in complicated cases where the fluids overturn; however, it does not allow fluid to "pinch-off" (i.e., the chain must always be connected). Each element was given a buoyancy contribution of 1, when the fluid was below the chain, and 0, when it was above the chain. (In practice, since the integration is done numerically, the Gauss points were weighted with a 1 or a 0 depending on where the chain crossed the element.) A similar method was discussed by Christensen and Yuen (1984). This method was compared with a double-diffusive method (Hansen and Yuen, 1989; Kellogg, 1990), where a chemical concentration field is solved with an advection-diffusion equation; and a particle method, where thousands of small tracer particles are randomly disbursed in the flow and a density for the element is assigned based on the number of particles.

The equations governing double-diffusive convection are the equation for conservation of mass in an incompressible fluid:

$$\nabla \cdot \boldsymbol{u} = 0 \tag{C.4}$$

conservation of momentum:

$$\nabla^2 \boldsymbol{u} = \nabla p + \mathrm{Ra}\, T\hat{\boldsymbol{k}} - \mathrm{Rb}\, C\hat{\boldsymbol{k}} \tag{C.5}$$

and the advection-diffusion equations for temperature, T, and concentration, C, of a tracer field indicating composition:

$$\frac{\partial T}{\partial t} = \nabla^2 T - \boldsymbol{u} \cdot \nabla T \tag{C.6}$$

$$\frac{\partial C}{\partial t} = \frac{1}{\mathrm{Le}} \nabla^2 C - \boldsymbol{u} \cdot \nabla C \tag{C.7}$$

where $\boldsymbol{u}$ is the velocity, p is the pressure, and T is the non-dimensional temperature. The dimensionless compositional field, C, indicates the presence of dense material; where $C = 1$ the material is densest; where $C = 0$ it is least dense.

The problem is governed by three dimensionless parameters. The effect of thermal buoyancy is controlled by the Rayleigh number, $Ra = \alpha \rho \Delta T d^3 / \mu\kappa$, where α is the coefficient of thermal expansion, ρ is the density, ΔT is the temperature drop across the box, d is the thickness of the box, μ is the viscosity, and κ is the thermal diffusivity. The chemical density contrast is controlled by the chemical Rayleigh number, $Rb = \Delta\rho_c d^3 / \mu\kappa$, where $\Delta\rho_c$ is the density contrast due to the compositional variation. The Lewis number, $Le = D/\kappa$, is the ratio of the chemical to the thermal diffusivities. For a chemical discontinuity in the mantle (e.g., an enriched iron lower mantle) the Lewis number should be quite high (i.e., 10^{10} for diffusion of iron) but due

to numerical limitations Lewis numbers of 100 are used. For some problems, we found that the diffusion caused a strong counter-flow to develop which stopped subduction and caused the plate to reverse direction. This counter-flow was not observed with the other methods and we attribute it to the excessive chemical diffusion and not to any relevant physics of the problem.

For the particle method, particles are placed at random locations in the initial domain of the denser fluid. These tracers are given a small buoyancy such that on average each element integrates to the total desired density. Then these particles are advected with the flow, and every time step their buoyancy is added along with the thermal buoyancy to drive the flow. For example, if there are 100 elements in the lower fluid and 2,000 particles are used, for a density contrast of 1% between the upper and lower fluid each particle is given a density of $0.2 \times \rho_o$, where ρ_o is the Boussinesque density. We found that for simple problems where small density differences from element to element average out, for example the Rayleigh-Taylor decay of a sinusoidal instability, often 10 particles per element matched the other methods satisfactorily. However, when small density perturbations become important, such as in calculating the geoid, often 100 to 1,000 particles per element were necessary. The cost of this method grows linearly with the number of particles; when greater than 100 particles per element are needed, the time spent advecting the particles dominates the calculation. From this we concluded that the marker chain method was the most efficient method for our purposes.

Appendix D

ConMan: Example Subroutine

```
      subroutine f_vRes(shl   , det   , tl    , lcblk  ,
     &                  t     , vrhs  , mat   , ra     ,
     &                  tq    , lmv   , lmt   )
c
      include 'common.h'
c
        dimension  shl(4,5)      , det(numel,5), tl(lvec,4)    ,
     &             lcblk(2,nEG)  , t(numnp)    , vrhs(nEGdf)   ,
     &             mat(numel)    , ra(numat)   , tq(lvec,5)    ,
     &             lmv(numel,8)  , lmt(numel,4)
c
      common /temp1 / el_rhs(lvec,8),blkra(lvec)
c
c-----------------------------------------------------------------
c
c     This routinue calculates the Right Hand Side velocity Residual
c
cInput:
c    lvec:          max length of element groups (64 for Cray)
c    numnp:         total number of nodes
c    numel:         total number of elements
c    nEGdf:         number of degrees of freedom for velocity
c                     equation (2*numnp)
c    shl(4,5):      shape functions (for mapping element)
c    det(numel,5):  determinant of element (for transformation)
```

```
c     lcblk(2,nEG):  element group info
c     t(numnp):      array of nodal temperatures
c     mat(numel):    material number of element
c     ra(numat):     rayleigh number of material groups
c     lmv(numel,8):  array linking element and local node number
c                      to global equation number for velocity
c     lmt(numel,8):  array linking element and local node number
c                      to global equation number for temperature
c
cTemporary:
c     tl(lvec,4):    temporary space for temperature array
c     tq(lvec,4):    temporary array for temperatures at
c                      integration points
c     el_rhs(lvec,8):temporary space for element contribution
c
cOutput:
c     vrhs(nEGdf): right hand side of velocity equation
c
c-----------------------------------------------------------------------
c
      include 'common.h'
c
c.... loop over the element blocks
c
      do 1000 iblk = 1 , nelblk
c
c.... set up the parameters
c
c     iel: starting element number of the group
c     nenl: number of element nodes ( 4 for bilinear elements )
c     nvec: number of elements in iblk th group
c
      iel    = lcblk(1,iblk)
      nenl   = lcblk(2,iblk)
      nvec   = lcblk(1,iblk+1) - iel
c
c..... localize (gather) the temperature for the whole element group
c
      do 150 iv = 1 , nvec
        ivel = iv + iel - 1
        tl(iv,1) = t(  lmt(ivel,1) )
```

```
        tl(iv,2) = t(  lmt(ivel,2) )
        tl(iv,3) = t(  lmt(ivel,3) )
        tl(iv,4) = t(  lmt(ivel,4) )
150   continue
c
c....form the temperature at integration points
c     the temperature at each integration point (tq(iv,1-4)) is
c     formed by adding contributions from all four nodes:
c     (tl(iv,1-4))
c
      do 200 iv = 1,nvec
         tq(iv,1) = shl(1,1) * tl(iv,1) + shl(2,1) * tl(iv,2)
     &            + shl(3,1) * tl(iv,3) + shl(4,1) * tl(iv,4)
         tq(iv,2) = shl(1,2) * tl(iv,1) + shl(2,2) * tl(iv,2)
     &            + shl(3,2) * tl(iv,3) + shl(4,2) * tl(iv,4)
         tq(iv,3) = shl(1,3) * tl(iv,1) + shl(2,3) * tl(iv,2)
     &            + shl(3,3) * tl(iv,3) + shl(4,3) * tl(iv,4)
         tq(iv,4) = shl(1,4) * tl(iv,1) + shl(2,4) * tl(iv,2)
     &            + shl(3,4) * tl(iv,3) + shl(4,4) * tl(iv,4)
200   continue
c
c...load the value of the rayleigh number into temp array blkra
c   for each element
c
c$dir no_recurrence
      do 300 iv = 1 ,  nvec
        ivel = iv + iel - 1
        blkra(iv) = ra(mat(ivel))
300   continue
c
c...calculate the contribution to each local element right hand side
c   due to the buoyancy (i.e. t*Ra )
c
      do 400 iv = 1 , nvec
      ivel = iv + iel - 1
        el_rhs(iv,1)=zero
        el_rhs(iv,3)=zero
        el_rhs(iv,5)=zero
        el_rhs(iv,7)=zero
        el_rhs(iv,2)=blkra(iv) * (tq(iv,1) * det(ivel,1) * shl(1,1)
     &                          +  tq(iv,2) * det(ivel,2) * shl(1,2)
```

```
     &                          +  tq(iv,3) * det(ivel,3) * shl(1,3)
     &                          +  tq(iv,4) * det(ivel,4) * shl(1,4))
c
        el_rhs(iv,4)=blkra(iv) * (tq(iv,1) * det(ivel,1) * shl(2,1)
     &                          +  tq(iv,2) * det(ivel,2) * shl(2,2)
     &                          +  tq(iv,3) * det(ivel,3) * shl(2,3)
     &                          +  tq(iv,4) * det(ivel,4) * shl(2,4))
c
        el_rhs(iv,6)=blkra(iv) * (tq(iv,1) * det(ivel,1) * shl(3,1)
     &                          +  tq(iv,2) * det(ivel,2) * shl(3,2)
     &                          +  tq(iv,3) * det(ivel,3) * shl(3,3)
     &                          +  tq(iv,4) * det(ivel,4) * shl(3,4))
c
        el_rhs(iv,8)=blkra(iv) * (tq(iv,1) * det(ivel,1) * shl(4,1)
     &                          +  tq(iv,2) * det(ivel,2) * shl(4,2)
     &                          +  tq(iv,3) * det(ivel,3) * shl(4,3)
     &                          +  tq(iv,4) * det(ivel,4) * shl(4,4))
400   continue

c
c..... assemble (scatter) the local element right hand sides into the
c      global right hand side
c
c$dir no_recurrence
      do 500 iv = 1 ,  nvec
         ivel = iv + iel - 1
         vrhs(lmv(ivel,1)) = vrhs(lmv(ivel,1)) + el_rhs(iv,1)
         vrhs(lmv(ivel,2)) = vrhs(lmv(ivel,2)) + el_rhs(iv,2)
         vrhs(lmv(ivel,3)) = vrhs(lmv(ivel,3)) + el_rhs(iv,3)
         vrhs(lmv(ivel,4)) = vrhs(lmv(ivel,4)) + el_rhs(iv,4)
         vrhs(lmv(ivel,5)) = vrhs(lmv(ivel,5)) + el_rhs(iv,5)
         vrhs(lmv(ivel,6)) = vrhs(lmv(ivel,6)) + el_rhs(iv,6)
         vrhs(lmv(ivel,7)) = vrhs(lmv(ivel,7)) + el_rhs(iv,7)
         vrhs(lmv(ivel,8)) = vrhs(lmv(ivel,8)) + el_rhs(iv,8)
500   continue
c
c.... end loop over element blocks
c
1000  continue
c
c....  return
```

```
c
      return
      end
```

Appendix E

Additional Calculations

This Appendix contains the temperature and composition plots for the calculations in the geoid plots shown in Figures 4.13 and 4.14.

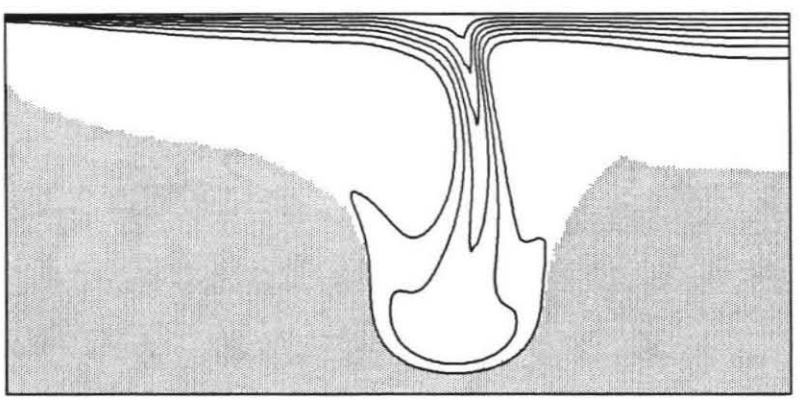

Figure E.1: Temperature (line contours) and composition (shading) for a constant viscosity slab calculation. The shaded material is 1% more dense than the white region.

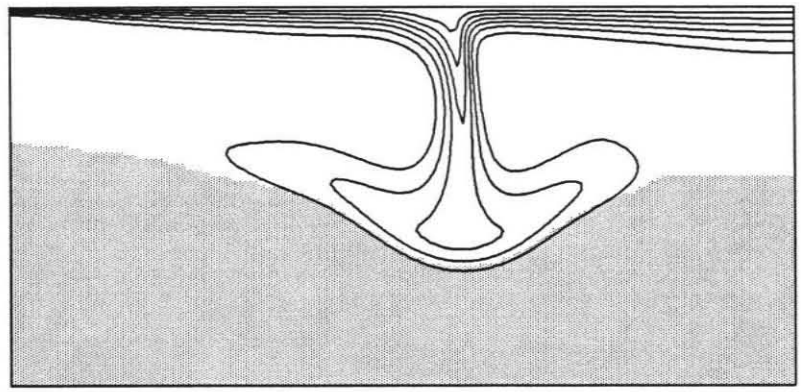

Figure E.2: Temperature (line contours) and composition (shading) for a constant viscosity slab calculation. The shaded material is 2% more dense than the white region.

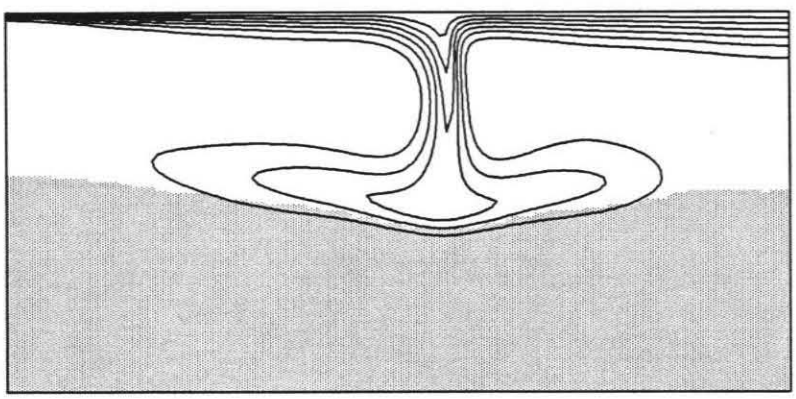

Figure E.3: Temperature (line contours) and composition (shading) for a constant viscosity slab calculation. The shaded material is 4% more dense than the white region.

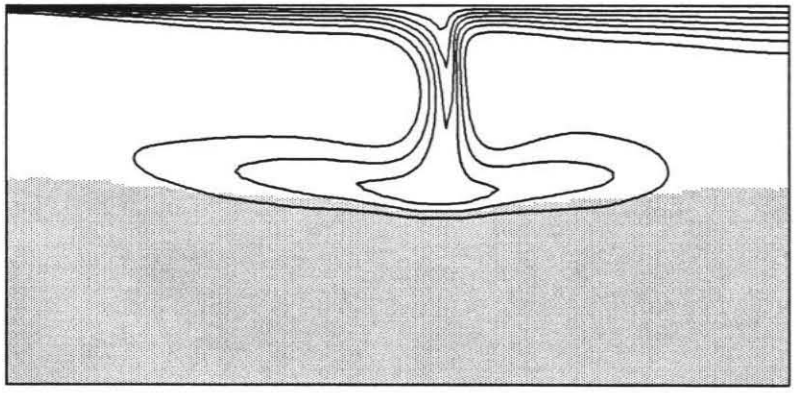

Figure E.4: Temperature (line contours) and composition (shading) for a constant viscosity slab calculation. The shaded material is 6% more dense than the white region.

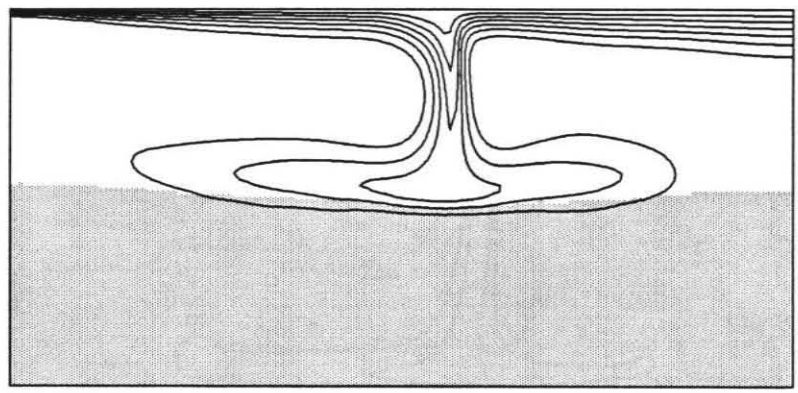

Figure E.5: Temperature (line contours) and composition (shading) for a constant viscosity slab calculation. The shaded material is 8% more dense than the white region.

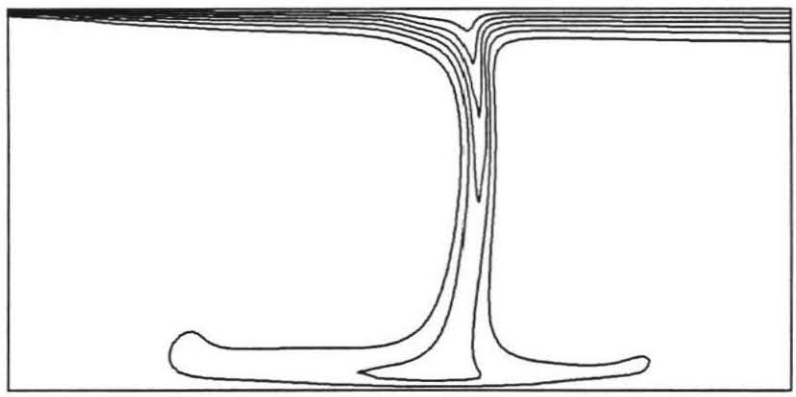

Figure E.6: Temperature (line contours) for a constant viscosity slab calculation with no density contrast.

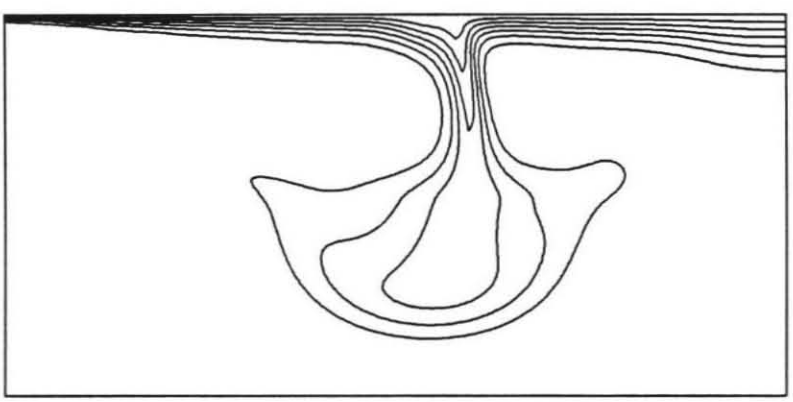

Figure E.7: Temperature (line contours) for a constant viscosity slab calculation with no density contrast and a 30 fold increase in viscosity at a depth of $0.5d$.

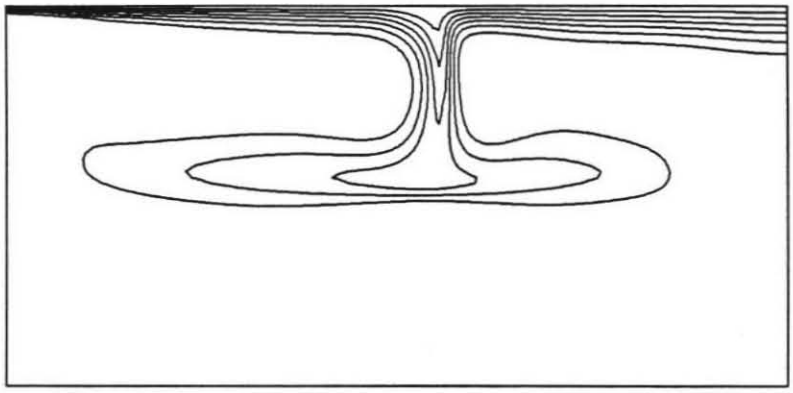

Figure E.8: Temperature (line contours) for a constant viscosity slab calculation with a no vertial velocity boundary condition at a depth of $0.5d$.

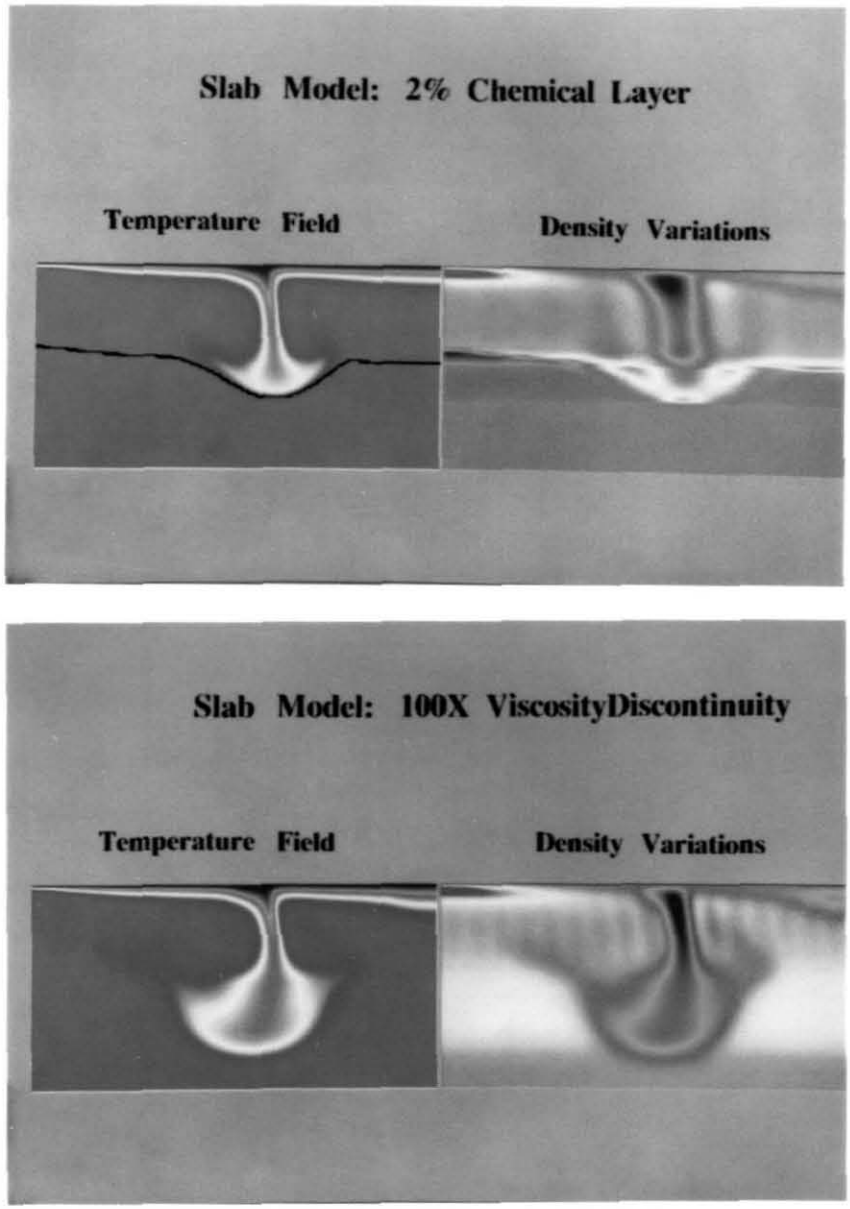

Frontispiece: Temperature and density field for a constant viscosity slab with a density (top) and viscosity (bottom) discontinuity (from Chapter 4).